



«Analyse de la fatigue, homogénéisation et optimisation de structures architecturées en titane obtenues par fabrication additive »

“Analysis of the fatigue, homogenization and optimization of the architectural structures in titanium obtained by additive manufacturing”

Bo-Ning YU

Directeur de thèse:	M. Yu-Ming LI
CoDirecteur de thèse:	M. Boussad ABBES
Président de jury:	M. Zhi-Qiang FENG

Abstract

With the continuous advancement and increasing demands in the field of medicine, electron beam melting (EBM) technology has shown extensive potential in the fabrication of biomedical implants. Among them, the rhombic dodecahedron lattice structure is a common design used for medical bone implants. This structure exhibits excellent mechanical properties and adaptability, making it suitable for replacing or repairing human skeletal tissues. In the design of lattice structures, the structure's elastic modulus and its fatigue performance are crucial factors to ensure the long-term stability of implants within the human body. Specifically, elastic modulus is particularly important as it effectively avoids stress shielding phenomena and enhances the load transfer capacity of the material. Additionally, the fatigue performance of implants during repetitive stress motion inside the human body is also of utmost significance.

This study analyzed the elastic deformation behavior and high-cycle compression fatigue behavior of the mapped lattice structure of a rhombic dodecahedron used in medical bone implants fabricated with electron beam melting method. Analytical and finite element models were developed to estimate the compressive elastic modulus and Poisson's ratios of mapped cellular rhombic dodecahedron structures with and without border constraints. The mapping function $x \rightarrow \alpha x$ was used to map strut coordinates, causing changes to strut section and position while maintaining porosity. We investigated compressive elastic modulus, Poisson's ratios, high-cycle compression-compression fatigue response, and the effect of cryogenic treatment on Ti6Al4V samples.

The mechanical properties of the Ti6Al4V rhombic dodecahedron lattice structure showed significant improvement as the mapping ratio α decreased. The equivalent elastic modulus of the cell is related to the number of periodic arrays of single cells under the condition of no boundary constraints. The modulus value increases monotonically with the number of cells and the diameter of struts, but the range of increase approaches a limit as the number of cells tends to infinity.

The influence of cryogenic treatment on the mechanical properties of the specimens and the fatigue fracture mechanism of the struts were analyzed through microstructure characterization. Cryogenic treatment enhanced elastic modulus, compressive strength, and fatigue performance, but increased accumulated strain along the compression direction after fatigue failure. The microstructure of Ti6Al4V alloy revealed the presence of α -Ti clusters and a strong texture, which in-

fluenced mechanical properties. Cryogenic treatment caused lattice distortion, grain refinement, and increased grain boundaries, which resulted in improving plasticity and fatigue performance while reducing creep resistance.

The analysis of mapped cellular rhombic dodecahedron structures introduced the mapping ratio α and developed analytical and finite element models to estimate elastic modulus and Poisson's ratios. The models considered changes in strut section and position. The analytical model showed promising predictions of elastic modulus and accurately predicted the effective elastic modulus of a homogeneous block. Fatigue life prediction involved determining maximum local stress, applying mean stress correction, and establishing the relationship between fatigue life of the homogeneous block and the life of the first fatigue-fractured strut. A nonlinear relationship was established between fatigue life and mapping ratio α , in which the smallest mapping ratio showed the best performance. The model provided accurate predictions and offered an alternative approach to predicting fatigue life based on testing results, saving costs.

Overall, this research successfully analyzed the mechanical properties, microstructure, and performance of Ti6Al4V base material and mapped cellular rhombic dodecahedron structures, providing valuable insights for understanding and predicting their behavior.

Key words: Lattice structure, Equivalent elastic modulus, High-cycle Fatigue, Analytical model, Ti6Al4V.

Résumé

Avec les avancées continues dans le domaine de la médecine, la technologie de fusion par faisceau d'électrons (EBM) a montré un potentiel étendu dans la fabrication d'implants biomédicaux. Parmi eux, la structure en losange dodécaédrique est une conception couramment utilisée pour les implants osseux médicaux. Cette structure présente d'excellentes propriétés mécaniques et une grande adaptabilité, ce qui la rend appropriée pour remplacer ou réparer les tissus squelettiques humains. Dans la conception de structures en treillis, la compréhension du module d'élasticité du matériau et de sa performance en fatigue est cruciale pour assurer la stabilité à long terme des implants dans le corps humain. L'étude du module d'élasticité est particulièrement importante car elle permet d'éviter efficacement les phénomènes de protection contre les contraintes et d'améliorer la capacité de transfert de charge du matériau. De plus, la performance en fatigue des implants lors des mouvements de contrainte répétitive à l'intérieur du corps humain revêt également une grande importance.

Cette étude analyse le comportement de déformation élastique et le comportement de fatigue en compression à cycles élevés de la structure en treillis cartographiée d'un dodécaèdre rhombique utilisé dans les implants osseux médicaux fabriqués par fusion par faisceau d'électrons. La recherche a développé des modèles analytiques et à éléments finis pour estimer le module d'élasticité en compression et les coefficients de Poisson des structures rhombiques dodécaédriques cellulaires cartographiées, avec ou sans contraintes de bord. La fonction de cartographie $x \rightarrow \alpha x$ a été utilisée pour cartographier les coordonnées des barres de soutien, entraînant des modifications de la section et de la position des barres tout en maintenant la porosité. L'étude a examiné le module d'élasticité en compression, les coefficients de Poisson, la réponse à la fatigue en compression-compression à cycles élevés et l'effet du traitement cryogénique sur les échantillons de Ti6Al4V.

Les propriétés mécaniques de la structure en treillis rhombique dodécaédrique de Ti6Al4V ont montré une amélioration significative lorsque le rapport de cartographie α diminuait. Le module d'élasticité équivalent de la cellule est lié au nombre d'ensembles périodiques de cellules simples dans des conditions sans contraintes de bord. La valeur du module augmente de manière monotone avec le nombre de cellules et le diamètre des barres, mais la plage d'augmentation approche une limite lorsque le nombre de cellules tend vers l'infini.

L'influence du traitement cryogénique sur les propriétés mécaniques des échantillons et le mécanisme de rupture par fatigue des barres de soutien a été analysée grâce à une caractérisation de la microstructure. Le traitement cryogénique a amélioré le module d'élasticité, la résistance à la compression et les performances en fatigue, mais a également augmenté la déformation accumulée le long de la direction de compression après une défaillance en fatigue. La microstructure du matériau Ti6Al4V a révélé la présence de grappes d' α -Ti et une forte texture, qui ont influencé les propriétés mécaniques. Le traitement cryogénique a provoqué une distorsion du réseau cristallin, un affinage des grains et une augmentation des joints de grains, améliorant la plasticité et les performances en fatigue tout en réduisant la résistance au fluage.

L'analyse des structures cartographiées en treillis rhombique dodécaédrique a introduit le rapport de cartographie α et développé des modèles analytiques et à éléments finis pour estimer le module d'élasticité et les coefficients de Poisson. Les modèles ont pris en compte les modifications de la section et de la position des barres de soutien. Le modèle analytique a montré des prédictions prometteuses du module d'élasticité et a reflété avec précision le module d'élasticité effectif d'un corps homogène. La prédiction de la durée de vie en fatigue impliquait la détermination de la contrainte locale maximale, l'application d'une correction de contrainte moyenne et l'établissement de la relation entre la durée de vie en fatigue du bloc homogène et la durée de vie de la première barre de soutien fracturée par fatigue. Une relation non linéaire a été observée entre la durée de vie en fatigue et le rapport de cartographie α , le plus petit rapport de cartographie montrant les meilleures performances. Le modèle a fourni des prédictions précises et offrait une approche alternative pour prédire la durée de vie en fatigue basée sur les résultats des tests, ce qui permettait de réaliser des économies.

Dans l'ensemble, cette recherche a analysé avec succès les propriétés mécaniques, la microstructure et les performances du matériau de base Ti6Al4V et des structures cartographiées en treillis rhombique dodécaédrique, fournissant des connaissances précieuses pour comprendre et prédire leur comportement.

Mots clés: Structure en treillis, Module d'élasticité équivalent, Fatigue à haute fréquence, Modèle analytique, Ti6Al4V.

Catalogue

Abstract	I
Résumé	III
Chapter 1 Introduction	1
1.1 Research background	1
1.2 Additive Manufacturing of Titanium Alloy Lattice Structures	3
1.2.1 Characteristics of additive manufacturing.....	3
1.2.2 Titanium alloy	4
1.2.3 Lattice structure.....	8
1.3 The fatigue performance of additive manufacturing lattice structures.....	14
1.3.1 Fatigue Mechanisms of Lattice Structures at the Microscale	15
1.3.2 Influencing factors for the fatigue performance of lattice structures	16
1.3.3 Failure of lattice structures under cyclic loading	21
1.4 Research significance and subject.....	25
1.4.1 Research significance	25
1.4.2 Research objectives	26
Chapter 2 Methodology.....	29
2.1 Design of the mapped rhombic dodecahedron in Ti6Al4V.....	29
2.2 Fabrication via EBM	29
2.3 Cryogenic treatment	30
2.4 Microstructural characterization	30
2.5 Mechanical properties	30
2.6 Numerical modelling.....	31
2.6.1 Finite element theory of beam element	31
2.6.2 Fatigue model.....	33
Chapter 3 Material properties and microstructure characterization	35
3.1. Samples and surface roughness.....	36
3.2 Mechanical properties	37
3.2.1 Mechanical properties of base metal	37
3.2.2 Mechanical properties of Rhombic dodecahedron.....	41

3.3 Characterization of microstructure evolution.....	46
3.3.1 Metallographic observation.....	46
3.3.2 EBSD analysis.....	48
3.3.3 TEM analysis.....	51
3.4 Fracture morphology analysis	53
3.4.1 Failure analysis of joint	53
3.4.2 Failure analysis of struts.....	54
3.4.3 Effect of cryogenic treatment on fatigue fracture	55
3.5 Summary	57
Chapter 4 Geometric modeling	59
4.1 Homogenization of rhombic dodecahedron	59
4.2 Geometry of the unit cell.....	61
4.3 Mathematic description of the beam's section	63
4.4 Summary	70
Chapter 5 The analytical calculation of the equivalent elastic modulus	71
5.1 Application conditions of the structure under compression	71
5.1.1 Application without border constraint in the plane XO_gY	72
5.1.2 Application with border constraint in the plane XO_gY	72
5.1.3 Lower and upper bounds of effective elastic modulus by using analytical method.....	73
5.2 Analytical model for lower bound of effective elastic modulus	74
5.3 Analytical model for upper bound of effective elastic modulus	83
5.4 Modeling for structure with border constraint	87
5.5 Finite element modeling by using beam theory	90
5.5.1 Stiffness matrix of a beam in the local coordinate system.....	90
5.5.2 Stiffness matrix of a beam in the global coordinate system.....	91
5.6 Results and discussion.....	95
5.7 Summary	104
Chapter 6 Prediction of high-cycle fatigue	107
6.1 Simulation of first fatigue fracture on the single strut in multi-cells	108
6.2 Analytical calculation of local maximum stress.....	111

6.3 Fatigue life of multi-cells under preset load limit.....	114
6.4 Summary:	121
Chapter 7 Conclusion.....	123
Chapitre 7 Conclusion.....	127
References	131
Publications	143
Acknowledgments.....	145

Chapter 1 Introduction

1.1 Research background

As a rapidly evolving advanced manufacturing technology, Additive Manufacturing (AM) has gained significant attention from various industries in recent years due to its ability to achieve a strong correlation between microstructure and mechanical properties. These industries encompass automotive¹, construction², biomedical³⁻⁶, unmanned aerial vehicles⁷, and aerospace⁸, among others. Among these techniques, Electron Beam Melting (EBM) technology has gained popularity due to its fast manufacturing efficiency and energy utilization⁹.

With the continuous and rapid growth of industrial demands, product diversification and increasing complexity in design have become inevitable trends. In comparison to traditional manufacturing processes, AM technology enables the design of complex geometric models and the rapid and accurate production of components, including lattice structures, at relatively low process costs¹⁰. A lattice structure is a minimum three-dimensional framework porous structure composed of struts or layers arranged in a spatial three-coordinate array and has emerged as a promising structural configuration¹⁰. Porous structures offer the ability to control the directional response of different mechanical properties and shapes within a controllable range through preliminary design, providing varying structural stiffness, impact resistance, and energy absorption capabilities¹¹⁻¹⁴. Compared to the traditional octahedral beam lattice structures, three-dimensional periodic arrangements of porous structures exhibit higher mechanical performance¹⁵. The commonly used cell types in industrial applications include cubes, rhombic dodecahedron, and other lattice structures¹⁶.

Lattice structures are considered as one of the optimal candidate materials for implant replacement due to their permeability and stiffness compatibility with cortical bone. Previous studies have shown that the elastic modulus of human cortical bone is approximately 30 GPa¹⁷, while that of trabecular bone is approximately 1.5 GPa¹⁸. Among various lattice structures, rhombic dodecahedron is commonly used in biomedical implants. As substitutes for human skeletal structures, they exhibit similar porosity and density to natural human bones. The development of biomaterials for human implants must consider the biocompatibility with human tissues as well as excellent mechanical properties such as bending, compression, torsion, and fa-

tigue resistance¹⁹. The low elastic modulus of rhombic dodecahedron avoids stress shielding effects, making them safer alternatives to human skeletal structures²⁰.

AM technology enables the customization of biomedical implants using various metals and alloys, including steel, magnesium, and titanium²¹. Among them, titanium alloys, especially Ti6Al4V, are suitable implant materials for replacing human skeletal structures due to their excellent mechanical properties, corrosion resistance, and biocompatibility. The incorporation of porosity and the reduction of elastic modulus in Ti6Al4V functional lattice structures implanted in organism can accelerate tissue generation and integration. Compared to conventional casting or forging products, Ti6Al4V lattice structures fabricated using Electron Beam Melting (EBM) exhibit comparable or even superior mechanical properties²²⁻²⁴, and their characterization complements the alloy's properties^{25,26}.

However, AM technology leads to significant cooling gradients during the solidification process, resulting in compositional and morphological variations in the microstructure of Ti6Al4V²⁷. The material exhibits numerous metastable microstructures and non-equilibrium compositions, which may vary with each deposited layer of the build. The metal powder solidifies starting from the substrate direction, and the thermal conductivity along the build direction is typically higher than in other directions. The high thermal gradients result in residual stresses during the rapid solidification process of the metal. After the fabrication of the component, internal stresses in the metal can self-regulate or cause local secondary bending, leading to material anisotropy and the formation of texture^{28,29}. Residual stresses³⁰ and anisotropy³¹ significantly influence the fatigue performance under cyclic loading. Appropriate post-processing methods can optimize stress distribution and prevent cracking of the component.

According to statistics, repetitive low-intensity loads caused by daily activities can result in fatigue damage to trabecular bone, which is a potential cause of fractures in hard tissues such as joints and the spine. The study of the fatigue behavior of implants under low-stress high-cycle loading is essential³². Point lattice structures with different gradients can achieve longer fatigue service life, and the improvement of gradient substructures in lattice structures makes them highly attractive for high-cycle applications.

The main objective of this study is to analyze the elastic deformation behavior of Ti6Al4V mapped rhombic dodecahedron lattice structures prepared by EBM. By conducting stress analysis, the mechanical adaptability of this type of lattice structure in the human body under biome-

chanical conditions will be assessed. Furthermore, the study aims to predict the service life of the lattice structure under static loading and daily activity stress levels. The findings of this research not only provide guidance for the design of lattice structures in the field of biomedical applications but also serve as a reference and complement for the practical application of emerging and popular lattice structures in additive manufacturing.

1.2 Additive Manufacturing of Titanium Alloy Lattice Structures

1.2.1 Characteristics of additive manufacturing

Additive Manufacturing technology (AM), compared to traditional manufacturing methods, offers a seamless process from design to final production without the need for additional processing steps, thereby meeting the requirements of sustainable development³³⁻³⁸. Additionally, AM provides greater customization freedom for the design of high-performance and complex structural components³⁹⁻⁴¹.



Fig 1.1 The design process for complex bio-inspired unit cells³⁹

The commonly used Additive Manufacturing (AM) technologies for fabricating complex structures using metal powders are primarily Laser Powder Bed Fusion (LPBF) and Electron Beam Melting (EBM)⁴²⁻⁴⁷. LPBF offers high manufacturing efficiency and is often used for producing large structural components. EBM can achieve precise and complex structures with good dimensional accuracy, making it suitable for high-performance engineering parts and medical implants.

The use of larger powder particle sizes (45-105 μ m) in the EBM process can result in certain manufacturing deviations⁴⁸⁻⁵¹. No manufacturing strategy currently satisfies the production of three-dimensional porous materials with controlled surface roughness. Moreover, the introduction of support structures between the substrate and the printed part leads to defects and increased roughness in the contact surface. During the solidification process, elongated columnar dendrites reduce the material's isotropy and, therefore, its fatigue performance⁵². Consequently,

surface treatment or other post-processing techniques are typically required to alleviate the high residual stresses generated during the printing process and ensure the proper functioning of the components in service⁵³.

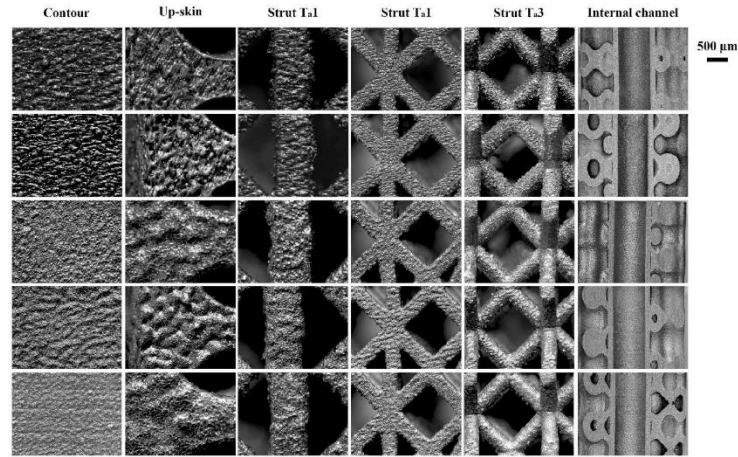


Fig. 1.2 The rough surface of additively manufactured AlSi10Mg struts⁵³.

1.2.2 Titanium alloy

1) Biocompatibility of Ti Alloys

Degenerative conditions such as osteoporosis, osteoarthritis, and bone injuries can lead to pain and tissue dysfunction^{54,55}. Consequently, higher requirements are imposed on bone and joint implants, specifically for cortical bone and articulating joints. Biomedical materials used as implants must possess adequate mechanical properties, corrosion resistance, excellent tribological performance, biocompatibility, osseointegration, and non-toxicity⁵⁶. Among these requirements, biocompatibility and non-toxicity are of primary importance as they determine the compatibility of the implants with the host tissue⁵⁷⁻⁵⁹.

After meeting the biological requirements, the selection of implant materials should consider their specific mechanical properties based on their applications in different parts of the human body. One common issue in biomaterials is stress shielding. When implant materials adhere to cortical bone with different stiffness behaviors, they experience wear stress due to relative motion under applied cyclic loads⁶⁰. The difference in elastic modulus results in uneven load distribution between the bone and the implant, with the bone bearing lower stress⁶¹. The mechanical mismatch between rigid implant materials and soft tissues can cause damage or irritation to the soft tissues, leading to the rejection of the implant by the human system⁶². This mechanical incompatibility, which leads to the death of bone cells, is known as stress shielding.

To minimize the impact of stress shielding, improvements in implant design focusing on material stiffness and geometric shape have been considered.

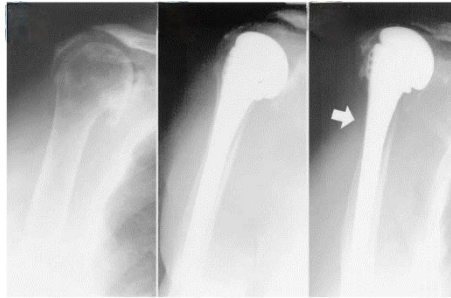


Fig. 1.3 Bone resorption caused by stress shielding effects in a bone implant after 7 years of service⁶¹.

Since the 19th century, the most commonly used metallic biomaterials for skeletal implants in the human body include stainless steel^{63,64}, magnesium and magnesium alloys^{65,66}, and titanium and titanium alloys⁶⁷. Among these, titanium and titanium alloys are considered as one of the optimal custom materials for biomedical implants, often appearing in lattice or topological structures. Their elastic modulus is closer to that of cortical bone, resulting in more uniform stress absorption and distribution around the bone⁶⁸⁻⁷⁰. The elastic modulus can be adjusted by modifying the porosity of the bone. Porous structures with three-periodic lattice unit cells exhibit controllable porosity and tight interconnectivity within the lattice, facilitating nutrient diffusion and waste removal⁷¹. Additionally, the lattice's porous structure and rough internal and external surfaces promote the adhesion, proliferation, and differentiation of osteoblasts, facilitating the growth of new bone tissue and forming a biological bond between the implant and bone. Three-dimensional interconnected pore scaffolds also facilitate fluid and nutrient transfer within the implant, promoting tissue regeneration and reconstruction and accelerating the healing process⁷².



Fig. 1.4 Porous EBM Ti-6Al-4V cage (A) used in creature tests.

The stress shielding effect can also be minimized through structural optimization of the implant. Zhang et al. modified the geometry of the femoral stem to improve load transfer across the cross-sectional area of the stem, thereby reducing stress shielding issues⁷³. Additionally, achieving an excellent combination of high mechanical strength and appropriate elastic modulus values that are closer to that of the replaced bone helps prevent implant loosening⁷⁴.

The mechanical properties of metal implant materials must be designed based on the characteristics of the associated tissues. The main properties that affect the mechanical compatibility of implants are strength, hardness, stiffness, toughness, fatigue strength, and ductility⁷⁵. Most implants operate under static or high-cycle repetitive stress conditions, requiring both high strength and ductility in their structure and materials. Biomaterials must also achieve a certain level of mechanical durability to effectively fulfill their intended functions. For example, hip prostheses need to exhibit high fatigue resistance to function for over 10 years under heavy loads. Titanium alloys are commonly chosen for bone fixation, hip prostheses, and knee implants due to their high toughness, fatigue resistance, and suitability⁷⁶⁻⁷⁸.

Walking is one of the most frequent activities in human movement and represents a major loading scenario for bone and joints in terms of load-bearing and bending. Patients with implants intended for human use may participate in walking activities ranging from 10^5 to 10^7 steps per year. The mechanical characteristics to be primarily considered during the 10-year service life of implants in the human body are the application conditions of low stress and high frequency^{32,79}.

Up to now, most of the research has primarily focused on traditional titanium alloys with uniform single-cell pore sizes in an open lattice structure and foam materials. However, to promote bone growth, a higher porosity of the cellular structure is desirable, but unfortunately, this compromises their mechanical performance. Considering these limitations, attention has been drawn to artificial titanium and titanium alloy lattice structures with density or structural gradients. Research has shown that a continuous graded design approach can be employed to design biomimetic bone implants with improved lifespan⁸⁰. However, uniform structures exhibit better cell proliferation compared to the other two structures⁸¹. Current research aims to find a balance between eliminating stress shielding and enhancing fatigue performance through cellular structure optimization and material modification⁸².

2) The influence of microstructure on the performance of Ti alloys

Due to the thermodynamic differences in the process routes, additive manufacturing parts exhibit significantly different microstructures compared to traditionally manufactured parts, resulting in distinct mechanical and tribological properties. The strength of Ti6Al4V produced by Electron Beam Melting (EBM) is largely dependent on the process parameters employed. The microstructure morphology primarily consists of nanoscale lamellar α -Ti grains. It is composed of columnar primary β -grains oriented parallel to the build direction, forming a layered fine $\alpha+\beta$ phase transformation microstructure^{83,84}. Following the Hall-Petch relationship, the strength increases as the size of the lamellar α -Ti grains and the scale factor of the α -Ti clusters decrease⁸⁵.

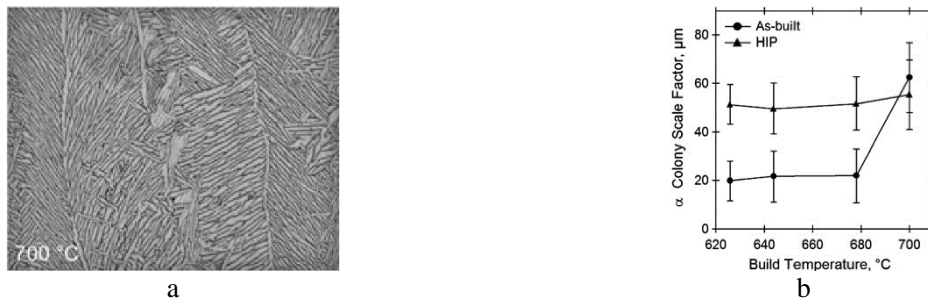


Fig. 1.5 a: The scale factor of α -Ti phase clusters in relation to the β -Ti transus temperature b is described by the following relationship⁸⁵.

Alpha (α) alloys possess higher melting points, which are conditions for the transformation to secondary beta (β) phase, higher flow stress, better weldability, and elevated temperature strength. Beta (β) alloys exhibit higher room temperature strength, better heat treatment adaptability, improved formability, and sensitivity to strain rate. However, beta alloys have poorer creep resistance, and prolonged service time can lead to loss of structural rigidity and deformation. On the other hand, binary $\alpha+\beta$ alloys exhibit stronger fracture resistance, better high-cycle fatigue response, and higher strength under high-temperature conditions, making them the most suitable titanium alloy types for biomedical implants. Additionally, appropriate addition of titanium (Ti) elements in the alloy composition helps to lower the alloy's elastic modulus and enhance its plasticity^{69,86}.

Titanium alloys with a high proportion of β -Ti stabilizing elements are known as beta (β) alloys. These alloys, characterized by their low elastic modulus and excellent biocompatibility, are an excellent choice for medical implants. Among them, the metastable β -type titanium alloy

Ti-33Nb-4Sn (wt%) developed by Guo et al. exhibits an elastic modulus of 36 GPa, which can mimic the mechanical properties of human bones and meet the requirements of high strength and low elastic modulus⁶. However, the specific characteristics of Electron Beam Melting (EBM) technology result in significant orientation deviations between adjacent grains, and fatigue cracks propagate in regions where columnar grains undergo deviation⁸⁷.

The microstructural differences in Ti-6Al-4V caused by solidification rate significantly affect the mechanical properties of the material. Samples cooled slowly exhibit a typical equilibrium $\alpha+\beta$ lamellar structure, while samples quenched show a fine needle-like α' -Ti phase. The X-ray diffraction (XRD) pattern of the rapidly quenched samples is very similar to the as-printed state of the AM without post-processing, with only peaks associated with HCP-Ti observed. In contrast, the XRD pattern of slowly cooled samples detects peaks related to both HCP-Ti and β -Ti, with the latter having lower yield strength and compressive strength. This result may be attributed to the lower elastic modulus of the β -Ti phase compared to the α -Ti and α' -Ti phases⁸⁸.

In the above studies, the process parameters of additive manufacturing technology have a significant influence on the microstructure of Ti6Al4V alloy, and the differences in microstructure lead to substantial variations in the macroscopic mechanical properties. Therefore, in-depth research and necessary steps are required to modify the material through microstructural control.

1.2.3 Lattice structure

1) Strut-lattice structures

Small-scale structures developed based on lattice structures allow for customized materials with multifunctional properties, which are not naturally occurring. In general, lattice materials can be conceptualized as periodic arrangements of beam elements forming a grid, with straight beams commonly used as the standard practice. Gibson et al. proposed that porous materials can be constructed by periodically arranging various types of porous geometrical shapes, such as triangles, squares, rhombi, and rhombic dodecahedrons, and provided relationships between the porosity and size parameters of these partial porous structures¹⁰.

Additive manufacturing lattice structures made of metals exhibit excellent performance in energy absorption, biomedical, and heat exchanger applications⁸⁹⁻⁹¹. Compared to traditional octet-truss lattice structures, three-dimensional periodic arrangement porous structures demonstrate higher static mechanical properties at the same volume fraction¹⁵. They can even exhibit

unusual mechanical behaviors such as negative Poisson's ratio, shape memory behavior, and superelasticity⁹².

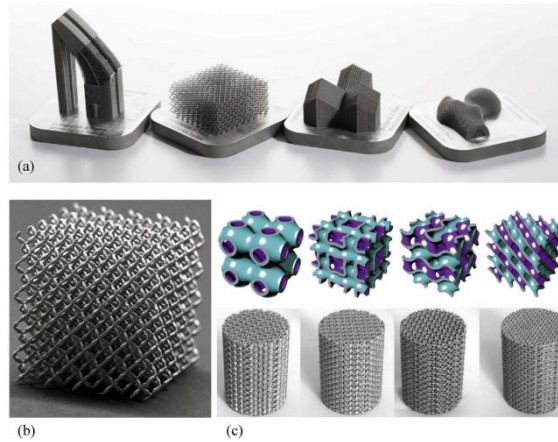


Fig. 1.6 Porous Ti-6Al-4V biomaterials and functional implants with different designs and functionalities include: (a) Porous Ti-6Al-4V biomaterials and implants with various designs and functionalities; (b) Rhombic dodecahedron structures; (c) Three-periodic minimal surface sheet-like lattice structures based on various types⁹².

The key parameters that influence the AM lattice materials include: strut diameter, equivalent size of the specimen, base material density, porosity, surface roughness, and post-process⁹³. Increasing the strut diameter leads to an increase in the equivalent compressive strength, yield strength, and fatigue strength of the lattice structure. However, due to process influences, the actual porosity of the printed part shows a trend of initially increasing and then decreasing with the increasing strut diameter. This may be attributed to incomplete melting of the metal on the struts that are inclined at a certain angle with respect to the printing plane, particularly when the strut diameter approaches the lower limit of printing accuracy. Smaller-sized struts exhibit higher sensitivity to variations because their changes have a greater impact on the accuracy response⁹⁴.

2) Truss lattice structure

The truss lattice structure is primarily composed of interconnected beams to form an open porous truss. It is widely used in high-end precision industries such as aerospace, naval, and biomedical fields due to its high strength-to-density ratio, excellent energy absorption capability, and high heat transfer efficiency⁹⁵⁻⁹⁷. The truss structure usually lacks regular geometric symmetry, making deformation prediction complex. A common approach is to establish the struc-

tural equilibrium equations using beam theory and combine them with finite element analysis to characterize the performance of metal sandwich panel structures. Numerical simulations can be employed to study the structural response under compression, shear, and tension conditions⁹⁸.

For truss structures with relatively high relative density, an embedded node model is suitable for predicting their response, while for truss structures with relatively low relative density, a pin node model is used to achieve more accurate predictions⁹⁹. When the truss lattice with higher relative density is sufficiently rigid, bending deformation should not be neglected. The relative density and mapping ratio of the supports determine the mechanical performance of the truss lattice structure, where the mapping ratio is the ratio of height to rotational radius. For thicker struts, a lower mapping ratio should be considered, and sufficient shear and bending moments should be taken into account when predicting the mechanical performance¹⁰⁰. Finite element analysis can be used to predict the deformation of truss lattice structures composed of struts under bending, and the deformation is highly sensitive to factors such as the equivalent density, triangular cell size, and cell arrangement of the structure¹⁰¹.

Based on the aforementioned studies, when using beam theory to model the homogeneous block of lattice structures, it is important not only to consider the role of local geometric models but also to analyze the deformation of nodes and supports. The response to stress becomes more pronounced in denser structures. Analytical models for porous materials may not be universally applicable to all cells; therefore, a unique stress analysis for each structure may provide more accurate predictions.

3) Equivalent modulus of lattice structure

The structure composed of a periodic arrangement of lattice cells is characterized by an effective elastic modulus that differs from that of dense materials but is closely related to the modulus of the base material. This is because the presence of regularly arranged voids in the structure significantly affects the effective elastic modulus, which is influenced by the porosity. High porosity, low elastic modulus, and excellent fatigue resistance are desirable properties for porous materials used as biomedical implants. Compared to array structures composed of continuous surfaces, lattice structures filled with beams more closely approach the desired performance. In particular, when the porosity exceeds 95%, thin-layered structures cannot provide sufficient strength, while beam structures dominated by bending exhibit excellent properties¹⁰². For thin-walled porous structures, the mechanical properties of the porous structure can be con-

trolled by topological optimization, achieving anisotropic controllability. However, standard beam structures exhibit significant boundary effects, and when the target porosity is fixed, it is challenging to change the structural mechanical properties by adjusting the dimensions of the struts. Although the elastic modulus in the loading direction of the thin-walled porous structure can be controlled through structural optimization, the elastic moduli in the other two directions will also change significantly. Currently, the development of isotropic porous materials capable of accommodating multidirectional loads through topological design remains a challenge.

For lattice cells, when subjected to force in a specific direction, the deformation is uniform, and the deformation in the cross-section perpendicular to the corresponding coordinate axis can be considered as equal everywhere. However, when multiple types of cells exist in the overall structure or when there is a gradient change within a single cell, the deformation in the corresponding cross-sections can vary significantly.

The relative density of standard diamond-cuboctahedral lattice structures in applications typically ranges from 20% to 30%, corresponding to an approximate range of equivalent elastic modulus from 0.7 to 4.4 GPa. For equivalent homogenous blocks of the same size and with the same porosity, increasing the cell edge length leads to a decrease in both the yield strength and the equivalent elastic modulus of the homogenous block. When quantifying the equivalent elastic modulus, relative density is commonly used as an expression. For pore structures without gradient changes, their mechanical properties should meet the engineering requirements for impact absorption and load-bearing. The cell size, shell thickness, and relative density have a significant influence on the customized mechanical properties, while they are closely related to energy absorption and compressive modulus¹⁰³.

The complexity of the rhombic dodecahedron lattice structure makes numerical simulations of the structure time-consuming and cumbersome. Achieving homogenization of the structure under compression conditions can yield an equivalent homogeneous solid with an effective elastic modulus in the compression direction, making numerical simulations more efficient. Ba-bae et al. derived analytical relationships for the equivalent mechanical properties of the rhombic dodecahedron lattice based on the principles of material mechanics. They determined that the equivalent elastic modulus is a function of the porosity, providing valuable insights for subsequent research.¹⁰⁴

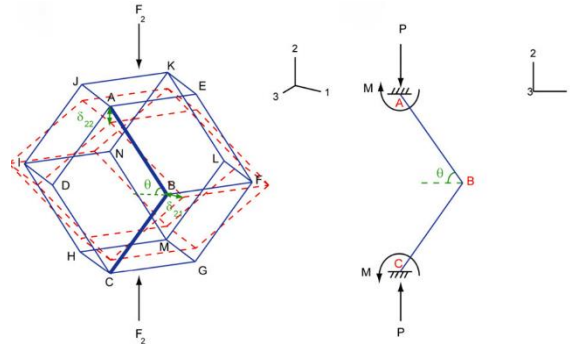


Fig. 1.7 Schematic of a rhombic dodecahedron unit cell under uniaxial compression¹⁰⁴

When there is a significant gradient variation in lattice structures, Yang et al. performed analytical calculations of the elastic modulus under different deformation modes using a BCC lattice structure composed of iron-mimicking beams. They found that different boundary conditions had a significant impact on the mechanical properties of the interlayered BCC lattice structure, corresponding to different deformation modes of the struts. Damage in the cubic interlayered BCC lattice tended to occur at the interfaces of different strut deformation modes, making the gradient lattice structure highly susceptible to failure at the gradient interfaces¹⁰⁵.

For composite structures consisting of two types of cells, it is feasible to control the anisotropy and elastic modulus selection of the structure by adjusting the local volume fraction¹⁰⁶. Additively manufactured gradient Ti6Al4V lattice structures using EBM technology exhibit lower elastic modulus¹⁰⁷. Studies have found that the porosity of lattice structure materials has a significant influence on the mechanical properties of alloys, with elastic moduli and compressive strengths ranging from 0.5-15 GPa and 10-300 MPa, respectively. By optimizing the porosity of individual cells, the effective elastic modulus can be reduced, achieving the desired structural stiffness and deformation behavior. The cell model, which maintains a constant porosity in gradient variations, can provide stronger elastic performance and compressive fatigue resistance in the denser parts of the structure.

Comparing the influence of gradient direction on the performance of additively manufactured lattice structures, it has been found that compared to regular and uniform single-cell structures, the gradient structures in the compression direction exhibit superior plateau stress and compressive modulus. Additionally, the fatigue response of this structure is also better than the other two structures. The static compression response of the gradient structure is significantly affected by the gradient direction.

Compared to the standard angled lattice structure, when the specimen is designed with gra-

gradient variation and the gradient direction is parallel to the loading direction, the multi-cell structure exhibits better mechanical performance and energy absorption rate. Both structures exhibit failure modes of shear banding and localized collapse. The fatigue failure mechanism combines fatigue damage and cyclic ratcheting effect, with the gradient direction being a key factor influencing fatigue performance¹⁰⁸.

In a customized complete workpiece, there may not only be gradient variations but also multiple mixed structures in different regions, with interconnected cells. Comparing the elastic modulus of mixed lattice structures with the individual elastic moduli of each local substructure, it is generally observed that the mechanical performance of the mixed structure lies between the performance of the original structures and does not exceed any of the individual substructures. It is essentially a compromise. Mixed structures can also result in anisotropy of the structural body.

Through research, it has been found that the mechanical performance differences among substructures in a mixed lattice structure can be balanced by adjusting the local relative density and solid support size of the mixed structure^{109,110}. In gradient porous materials, the failure deformation under compressive loads also follows shear bands at a 45° angle. Additionally, local 45° shear bands exist in each gradient region of the structure¹¹¹. However, these methods may face limitations such as the discontinuity of monotonic anisotropy, the anisotropy coupled with volume fractions, or the misalignment of supports between substructures.

Not only the elastic modulus, but also the shear modulus of lattice structures plays an important role in characterizing the suitability of different materials in various multifunctional systems and devices. It is relevant for deformation in shear and torsion modes, as well as for vibration behaviors involving twisting, wrinkling, and ripple effects. The shear modulus, along with various other mechanical properties, can be modulated by employing appropriate network structures within conventional periodic lattices¹¹². Mathematically programmed designs of porous lattice structures are easily adaptable and manipulable, allowing for the customization of pore structures to achieve desired mechanical properties in heterogeneous gradient geometries. This approach enables precise control of the shear modulus and other mechanical properties by adjusting the shape, distribution, and connectivity of the pores. By careful design and optimization, tailored mechanical properties of lattice structures can be achieved to meet the specific requirements of different applications¹¹³.

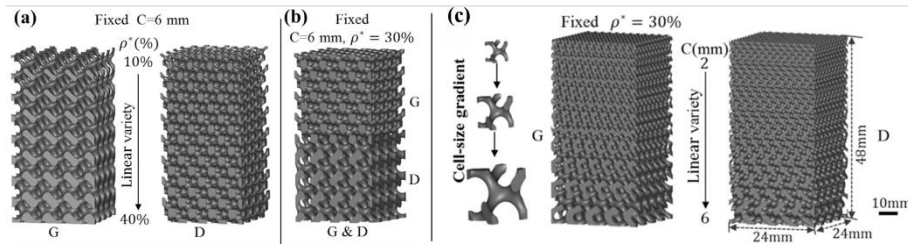


Fig. 1.8 Designed models of gradient samples (a) in relative density, (b) in heterostructure and (c) in cell size¹¹³

The research on gradient lattice structures mentioned above all points to one fact: the anisotropy caused by gradient variations within the structure not only greatly compromises the performance of the component in actual service but also significantly increases the difficulty of analyzing its stress distribution. Consequently, it becomes challenging to predict the deformation and lifespan of the structure. Since the mechanical performance of mixed structures cannot surpass that of any individual substructure, it is reasonable and feasible to focus the research on the substructures with excellent performance. By targeting these high-performing substructures, it becomes possible to design products with more predictable deformation and lifespan characteristics.

1.3 The fatigue performance of additive manufacturing lattice structures

At present, most of the research in the field focuses on fatigue testing of lattice structures. A fatigue S-N curve for a given lattice structure with the same unit cell is established⁹². Some analytical models consider lattice structures as open-cell structures composed of cubic beams. Compared to diamond lattice porous materials, cubic samples with buckling as the main deformation mode exhibit higher elastic modulus and strength but demonstrate catastrophic fracture behavior. Beam-based lattice structures, with bending as the main deformation mode, are suitable for compression loading conditions. Despite the predominance of bending, these structures exhibit good fatigue resistance due to the presence of load-bearing beams in all directions¹¹⁴.

The dominant deformation modes differ between the two types of structures, and the fatigue life of internal struts in lattice structures cannot be estimated using traditional prediction models. The diameter of the struts and the stiffness of the base material are the main parameters influencing the fatigue characteristics of lattice structures, and correcting factors need to be applied to account for variations in the size of internal struts¹¹⁵.

1.3.1 Fatigue Mechanisms of Lattice Structures at the Microscale

At the microscale, the fatigue initiation mechanisms of lattice structures differ from those of dense materials. In uniaxial compression conditions, dense materials exhibit minimal crack closure behavior, making fatigue damage less likely to occur. Whereas, localized tensile stresses are concentrated at the contact points in lattice structure, leading to fatigue failure. For such structures, the lattice type is more important than topological design. The fatigue failure mechanism of lattice structures under cyclic loading is similar to that of dense materials, involving the processes of crack initiation, propagation, and final fracture¹¹⁶. However, fatigue failure in lattice structures is not solely attributed to the failure of individual struts but rather a gradual collapse of the structure accompanied by stress redistribution.

In porous structures composed of interconnected struts, under cyclic compression loading, the struts reach their yield limits and undergo irreversible plastic deformation. This is manifested at the microscale as the motion of defects, namely dislocations, ignoring the recovery effect. With an increasing number of dislocations, localized strain hardening inhibits the reversibility of slip, resulting in the accumulation of dislocation pile-ups. At the same time, the accumulation of cyclic strain increases the dislocation density.

1) Crack initiation

Continuous irreversible dislocation slip within the grains forms steps, and the propagation of extrusion and intrusion in the slip bands initiates crack formation. The cracks initially propagate at a 45° to the loading direction, which is the first stage of fatigue crack growth. As the cracks extend towards the grain boundaries, their propagation direction gradually changes to be perpendicular to the loading axis, marking the second stage of fatigue crack growth. Inclusions within the struts also serve as crack initiation sites, with a higher degree of strain hardening due to the hindrance from surrounding grains to dislocation slip.

2) Crack propagation

At the microscale, microcracks start to propagate from the slip bands near the surface. As they approach grain boundaries, their propagation speed slows down, and some cracks may stop growing. Depending on the orientation of the next grain, some of the microcracks can traverse the grain boundaries and continue to grow in a slightly different crystallographic direction. Grain boundaries are not the sole obstacles to microcrack propagation.

In Ti and Ti-Al alloys, the crack propagation rate is influenced by grain size. The crack

paths exhibit tortuosity, with significant crack deflection, diversion, and secondary cracking, primarily due to the combined effects of coarse grain size and specific orientations of crack growth in lamellar structures¹¹⁷.

1.3.2 Influencing factors for the fatigue performance of lattice structures

1) Shape and size of lattice structures

The shape and size of lattice structures, as well as factors like porosity and errors in cell shape and size, can affect the mechanical performance of lattice structures. The irregular geometry induced by the shape and size of the lattice cells can lead to stress concentration and affect the fatigue strength of the structure.

Fatigue testing of lattice specimens under compression is challenging because it is difficult to achieve perfect contact between the specimen and the compression plates of the testing machine due to geometric tolerances. This imperfect contact can lead to highly scattered experimental results¹¹⁸.

Studies have shown that porosity plays a significant role in reducing fatigue life and increasing the unpredictability of material behavior under mechanical loading. Additionally, lattice structures dominated by bending or tension exhibit different mechanical properties and failure mechanisms compared to other loading conditions¹¹⁹.

Overall, the shape and size of lattice cells, porosity, and factors such as the number of arrays or printing precision can result in differences in the mechanical performance of lattice structures. Porosity has a significant impact on fatigue life and the behavior of materials under mechanical loads, and structures dominated by different loading modes can exhibit different mechanical properties and failure mechanisms¹²⁰.

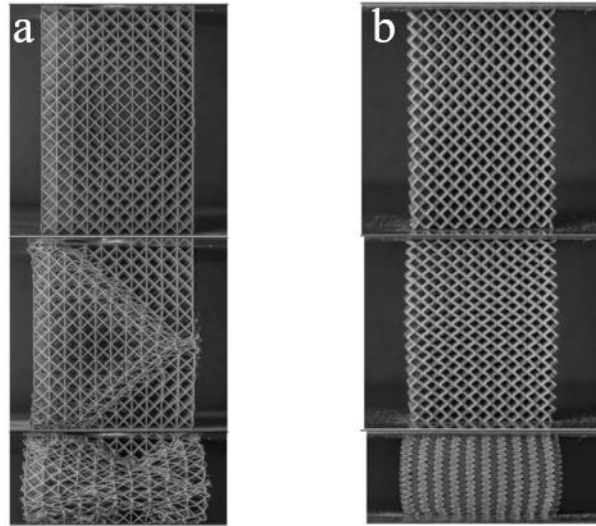


Fig. 1.9 Typical compressive failure for a: bending-, and b: stretching-dominated cellular materials with same relative density¹²⁰

In general, the larger the diameter of the struts, the higher the equivalent elastic modulus and the greater the fatigue performance¹²¹. However, due to the characteristics of the manufacturing process, the offset of the center of gravity of the joints reduces the equivalent elastic modulus of the structure. There are significant geometric deviations between the printed parts and the designed lattice structure. From a global stress perspective, these geometric deviations caused by the manufacturing process exhibit strong anisotropic fatigue behavior in Ti6Al4V lattice structures¹²². During the printing process, the distribution of the material depends not only on the geometric shape of the design but also on the local variations in process parameters and thermal performance of the system, resulting in struts being formed with different accuracy. Specifically, the angle formed between the struts and the printing plane causes a suspended effect of the accumulated molten material, indirectly increasing the deposition thickness and causing the center of the cross-section to deviate from the connection point, resulting in a 'wavy' texture on the forming surface. At the same time, the uneven distribution of the material on the joint results in a center of gravity shift and the formation of sharp notches between the struts¹²³. The roughness and mechanical properties of individual Ti-6Al-4V struts manufactured by EBM have been analyzed, and the vertical struts show significantly lower roughness than the oblique struts formed at certain angles in space. However, the mechanical properties obtained from static and fatigue experiments of oblique struts are superior to those of vertical struts¹²⁴. Increasing the angle of the struts in the porous material composed of struts leads to improved

compressive strength, yield strength, and plateau stress. The fatigue performance is also significantly enhanced. By changing the angle of the struts, the cyclic hysteresis strain and fatigue damage strain of the porous structure can be greatly reduced, thereby improving the fatigue life of the structure¹²⁵. The angle between adjacent struts at the joint is the main area of stress concentration. Topological optimization of this angle area during design, such as increasing the angle radius, can significantly improve the fatigue performance. With an increase in volume fraction, the optimization of the fillet brings about a more pronounced improvement in structural performance and energy absorption. Furthermore, the effect of the ratcheting, as the main failure mode under cyclic loading for this structure, can also be reduced by optimizing the fillet, thereby improving the structure's deformation resistance¹²⁶. Adding rounded corners at the joints of regular Ti6Al4V cubic lattice struts can significantly improve the fatigue fracture performance of the lattice structure. Failure always occurs in the vicinity of sharp angles in the joint due to insufficient fusion or irregular surface texture lines. Manufacturing defects have a smaller impact on larger-sized lattice cells compared to smaller-sized ones, and enlarging the lattice cell size can effectively improve the fatigue performance¹²⁷. Fatigue fracture of the porous material struts was found to be widely present in or near the joints, while plastic deformation of the struts was not significant¹²⁸.

Under compression conditions, the lattice structure exhibits uneven interlayer dissipation energy and strain distribution, with the middle layers experiencing more compression. This may be due to the upper and lower surfaces in contact with the testing system losing their support first when subjected to pressure.

2) Surface quality and internal defects

The high porosity of lattice structures reduces the elastic modulus of titanium alloys, which helps to avoid stress shielding effects between the implant and natural bone. However, due to the porosity and rough surface morphology, it weakens the fatigue strength¹²⁹. Therefore, this poses significant challenges for predicting the fatigue life of implant struts.

The cyclic mechanical performance of additively manufactured metal parts needs to be assessed and optimized, and the characteristics of manufacturing defects, such as size, shape, location, density, and distribution, play a crucial role in the fatigue performance of additively manufactured metals. Therefore, the influence of pore structures at small scales should be thoroughly characterized. The smoother the surface of the specimen and the smaller the deviation

from engineering design, the higher the monotonic compression mechanical performance^{130,131}. Due to the complex geometrical shapes of additively manufactured parts, the stress state at critical locations for fatigue is often multiaxial. The non-uniformity of the metal structure and the variability of defects in additively manufactured metals contribute to significant uncertainty and scatter in the fatigue behavior of these parts. Although the continuous curved surfaces in lattice structures can effectively eliminate stress concentration effects under static loading, the notch effect on the rough surfaces of Ti-6Al-4V lattice structures produced by EBM weakens their fatigue performance¹³². This is because this technology is known to produce parts with rougher surfaces compared to other AM technologies. The main reason behind this high surface roughness is likely the larger average size of the powder used in this process (approximately 76 μm). Surface roughness has also been found to vary depending on the build direction. Surfaces parallel to the build direction exhibit higher surface roughness compared to surfaces perpendicular to the build direction. Optical microscopy analysis of perpendicular surfaces revealed grooves along the width direction, which may be related to the scanning direction of the electron beam. Circular regions of partially sintered powder particles were observed on parallel surfaces, as a large number of powder layers were deposited on these surfaces, and the thermal conductivity favored larger surface areas of the component rather than the surrounding powder. Under high-cycle fatigue loading, texture bands on the surface of the struts can induce stress concentration at unmelted metal particles, leading to the formation of shear bands. The initiation mechanisms of cracks on the material surface highlight the significant role of surface quality in fatigue. This influence becomes more pronounced when plastic deformation is low. Surface treatments can greatly improve fatigue performance. Compared to internal defects in the material, the material's resistance to fatigue is more sensitive to surface irregularities (such as small-angle notches at joints).

However, the fatigue performance of additively manufactured metals is influenced by defects such as gas pores. The size of these defects is one of the main reasons for variations in the material's fatigue resistance. A fatigue crack growth model based on the ΔJ_{eff} concept can be established by inputting a finite set of parameters, which allows for the assessment of the high-cycle and low-cycle fatigue failure performance of dense additively manufactured parts¹³³. However, the lethal effects caused by the rough surface are difficult to overcome by a few internal defects, as cracks usually initiate from the surface. The fatigue limit measured from sur-

face defect analysis is more significant than that measured from internal defect analysis, making surface defects a determining factor in fatigue strength¹³⁴.

Introducing compressive residual stress through post-processing is an effective method to prevent fatigue crack initiation. Significant stress concentrations are observed at the junction of specimens that have not undergone post-processing. Post-processing, by reducing defects, eliminating residual stress, modifying microstructure, and improving surface quality, can have a significant impact on the fatigue performance of the parts. However, due to the complex internal porous structure of the scaffold, it is not possible or challenging to improve its fatigue life through surface treatments¹³⁵. The most straightforward and effective means to enhance the fatigue performance of porous structures at small scales is through appropriate post-processing methods that modify the material's internal properties.

3) The post-treatment

Microstructural inhomogeneity and residual stress also affect the fatigue performance of additively manufactured metals, particularly their yield strength under cyclic loading. The influence of residual stress gradually decreases with increasing number of cycles, and it weakens with increasing initial strain amplitude³⁰. Considering local stress is the most effective approach for studying the mechanical response of lattice structures, as it takes into account the porosity of the structure, strut size, and manufacturing defects. The majority of fatigue failures occur due to stress concentration at the junctions of the struts. Appropriate post-processing methods are the most effective means of improving the fatigue performance of Ti6Al4V lattice structures¹³⁶. Studies on the fatigue performance of Ti6Al4V components produced by additive manufacturing show that the fatigue life of AM parts is improved after stress relief²⁵. In additively manufactured alloys, initial defects exist, and specimens subjected to stress relief post-processing exhibit significantly improved fatigue strength, with the propagation of small cracks reaching threshold levels²⁵. Residual stresses generated during powder consolidation by rapid solidification are mainly elastic energy stored around fatigue cracks. The residual stresses around the cracks increase by 200% compared to other regions, which also affects grain rotation during deformation¹³⁷.

In terms of microstructure, the fine microstructure of AM seems to be an effective obstacle to dislocation motion, especially at longer lifetimes. Process parameters such as powder size and quality, power, scanning strategies and speeds, as well as preheating and temperature con-

trol of the substrate during the cooling process that affect cooling rates, all influence the microstructure and defect characteristics of the parts, thereby affecting the fatigue performance of the components¹³⁸. In titanium alloy microstructures, the size, orientation, and proportion of needle-like α -grains and β -grains, as well as the secondary α -Ti phase, contribute to the differences in material strength, hardness, and fatigue performance. Finer microstructures and weakened texture can provide better compressive performance and strength.

1.3.3 Failure of lattice structures under cyclic loading

1) Fatigue failure

Failure of lattice structures under cyclic loading is one of the failure modes, and it is commonly referred to as fatigue failure. Depending on the difference in cyclic stress amplitudes, it can be divided into low-cycle fatigue (LCF) and high-cycle fatigue (HCF). Under high-stress amplitude conditions, the failure of the material is primarily due to plastic deformation, and crack propagation occurs at a faster rate. Analyzing low-cycle fatigue in such extreme environments can be complex. Numerical simulation of fatigue in porous materials requires establishing data from fatigue testing of the base material. By using the low-cycle fatigue S-N curve and uniaxial tensile mechanical properties of the base material as inputs, numerical simulations based on the concepts of elastic-plastic homogenization and critical distance theory can determine the yield point and failure strain of lattice structures. This allows for the derivation of critical distances required for fatigue assessment and prediction of the low-cycle fatigue life¹³⁹.

In the case of low-cycle fatigue (LCF) fracture surfaces, multiple crack initiation points can be detected, and their morphologies can vary. The primary crack initiation points appear flat, while the secondary crack initiation points exhibit depressions. If the stress concentration at the secondary crack initiation point is sufficiently low, crack nucleation and propagation sensitive to the microstructure can be observed. This is characterized by intergranular fracture surfaces between lamellar α -Ti grains and the tearing of the primary β -phase grain matrix¹⁴⁰. As the crack propagates along grain boundaries, continuous grain boundary α -Ti phase leads to straight propagation, while discontinuous grain boundary α -Ti phase results in a bending propagation mode.

Currently, an approach has been proposed to analyze low-cycle fatigue by addressing the notch effect in the low-cycle fatigue cyclic environment. The reference curve method represents

the relationship between the strain energy density range and the number of cycles to failure. It calculates the short-range strain energy density range at the notch location and ultimately obtains a reasonable fatigue concentration factor value. However, dealing with complex geometric shapes of structural components remains a challenging task¹⁴¹.

For porous titanium alloy implants, the long-term cyclic performance under low stress amplitudes is the most important aspect to consider. Compared to single-cell geometry and porosity, the material type and manufacturing defects play a more significant role in determining the S-N curve of additively manufactured (AM) biomedical materials, particularly in the high-cycle fatigue regime. The fatigue response of these materials depends not only on the static and fatigue strengths of the base material but also on other factors such as the surface roughness of the struts (which affects crack initiation), the distribution of micropores within the struts generated during the additive manufacturing process (which affects crack propagation), and the plastic deformation mechanism (which affects crack initiation and propagation)¹⁴².

High-cycle fatigue analysis was performed on Ti6Al4V rhombic dodecahedron porous structures fabricated using Electron Beam Melting (EBM). It was found that the gradient grading within the structure resulted in variations in mechanical properties across different regions. As the number of cycles increased, cracks propagated from high-strength regions to low-strength regions until complete failure. During this process, stress continually redistributed, leading to changes in the cyclic ratcheting rates of the graded cellular structure. Stress redistribution in the low-strength struts could delay crack propagation in the high-strength struts⁶. The substructures with gradient variations are key to optimizing the performance of porous titanium alloy implants.

2) Ratcheting effect

The performance of human trabecular bone under fatigue behavior is characterized by a decrease in modulus, with creep accompanying the entire fatigue process. The number of cycles, cycle time, steady-state creep rate, and load intensity are closely related to the strength behavior of isotropic trabecular bone samples under constant fatigue. Creep analysis of fatigue and creep data indicates that the creep failure strain is constant and independent of density or the applied load. These similarities suggest that creep plays an important role in the fatigue behavior of trabecular bone¹⁴³.

The deformation behavior of lattice structures under high-cycle cyclic loading is similar to

creep behavior. The fatigue failure mechanisms of porous titanium structures are fatigue crack propagation and cyclic ratcheting, with cyclic ratcheting playing a dominant role. The compressive fatigue behavior of porous titanium exhibits strain accumulation characteristics, and there is a critical fatigue cycle (NT) on the curve of accumulated cyclic strain versus the number of cycles. When the cycle period is below NT, the strain accumulation is slow and constant, and the porous specimen deforms uniformly. Once the fatigue cycle exceeds NT, uneven deformation caused by fatigue crack propagation occurs, leading to the formation of collapse bands in the porous specimen and sudden failure¹⁴⁴. Other studies have also found that the strain accumulation in compressive fatigue damage of porous materials occurs in different stages during the cyclic process. Within 70% of damage, the strain accumulation is slow; between 70% and 95%, the accumulation gradually accelerates; after exceeding 95%, distinct 45° shear bands appear in the uniform region, followed by rapid fracture. This indicates that shear damage is the primary damage mechanism of fatigue damage in the specimen¹⁴⁵. Dislocations within the struts always generate along the α -Ti phase interfaces, and this phenomenon becomes more pronounced with increasing relative density. They are likely to help delay cyclic ratcheting and improve the fatigue strength of the specimen¹⁴⁶.

3) Fatigue life prediction

Fatigue prediction models often fail to provide satisfactory results for high stress levels. For most common porous structures, regardless of the stress level, catastrophic failure occurs when the number of failed elements reaches 1% of the total number of elements in the structure. Subsequently, the accumulated damage in the remaining struts quickly reaches the failure criterion¹⁴⁷.

In general, the fatigue life prediction of lattice structures under cyclic loading is often carried out using numerical simulation methods. Research has been conducted on low-cycle fatigue experimental data of lattice structures fabricated using selective laser melting (SLM) with Ti6Al4V alloy. A comprehensive finite element model incorporating the SLM Ti-6Al-4V composite hardening model and continuum damage criterion was developed to predict the stress-strain behavior and damage failure of lattice structures through numerical simulations. It was found that the initial location of LCF damage and the evolution path of damage in the lattice structure are influenced by the local tensile stress distribution in the lattice. Fatigue cracks tend

to initiate and propagate in regions with high tensile stresses¹⁴⁸. Constitutive relationships for titanium alloys under low-cycle fatigue were modeled by considering back stress, threshold stress, and slip resistance strain. Plastic strain accumulation and energy dissipation were used to predict fatigue damage. From the microstructure analysis, it was observed that fatigue damage tends to occur preferentially at the grain boundaries between α and β -grains due to slip impedance¹⁴⁹. Another approach for analyzing the low-cycle fatigue life of porous structures is based on numerical simulation using homogenization and critical distance theory. This approach minimizes computational requirements by using periodic boundary conditions and employs numerical simulation based on elastoplastic homogenization theory to determine the yield point and failure strain of the lattice, thus deriving the critical distance required for fatigue assessment. This method has been applied to study the deformation behavior of 2D or 3D lattice materials under low-cycle fatigue, contributing to the advancement in this field¹⁴⁷. For customized porous titanium alloy products, numerical methods remain feasible, although the structural complexity increases the computational cost. Particularly for high-cycle fatigue where the number of cycles is typically in the range of 10^6 , the detection of local failure in a large number of cells becomes challenging. Therefore, analytical methods are the preferred choice for handling small-strain high-cycle fatigue predictions.

Materials undergo significant cyclic softening during fatigue testing, where even at high strain amplitudes, the deformation is primarily elastic. Basquin's law can effectively be extended to high-cycle fatigue conditions. The high-cycle fatigue state is mainly determined by the average stress and material defects. In high-cycle fatigue, plastic hardening and compressive residual stresses can effectively prevent surface cracks but not subsurface cracks¹⁵⁰. Basquin's law is primarily applied based on the fatigue S-N curve of the base material and cannot accurately predict the fatigue life of lattice structures, which are non-dense materials. Internal struts gradually fracture after reaching the yield limit, leading to stress redistribution. The subsequent fracture process is dominated by cyclic ratcheting deformation of the equivalent homogeneous body until the load limit is reached. However, this process requires fatigue testing to establish the relationship between the fatigue life corresponding to the maximum local stress at the first broken strut and the life of the lattice structure. The stress on the corresponding strut cannot be represented by the Von Mises equivalent stress because von Mises equivalent strain does not correlate well with additive manufacturing (AM) materials. However, the use of the maximum

principal stress criterion shows better correlation among fatigue data under different loading conditions. This is attributed to the brittle behavior of AM Ti6Al4V alloy¹⁵¹.

Based on the research mentioned above, the main approach of this study is to predict the high-cycle fatigue life of specific lattice structures by homogenizing the structure and establishing a relationship between the S-N curve of the base material and the local maximum principal stress. This approach considers the predominance of elastic deformation in high-cycle fatigue failure. By relating the fatigue life to the maximum principal stress at the local level, specific predictions can be made for the fatigue performance of lattice structures.

1.4 Research significance and subject

1.4.1 Research significance

The rhombic dodecahedron lattice structure of Ti6Al4V fabricated by Electron Beam Melting (EBM) can be used as a biomedical implant in various replaceable skeletal sites. Each site has different requirements for implant performance. To accommodate these structural variations, the three-fold symmetric arrangement of rhombic dodecahedron unit cells can be mapped along specific coordinate axes in a unidirectional manner. The aim is to regulate the mechanical properties of lattice structures under different designs by altering the mapping relationship.

The rhombic dodecahedron structure is complex, and previous studies have typically used numerical simulations, personalized modeling, and finite element analysis to obtain the compression load-displacement relationship of this structure. However, in practical applications, individual cells usually operate at a small scale, and the number of cells can be quite large. Both geometric modeling and numerical computations require significant computational costs that often exceed the capabilities of the available resources.

Some studies have attempted to establish an analytical relationship between the bending deformation of the beam-column structure within the individual cell and the overall structure deformation through a simple homogenization approach. However, these studies did not consider the influence of the number of cells on the structure. As the number of cells increases, the struts on the boundary of the structure suffer from boundary effects, resulting in free deformation. This leads to a certain gradient of stress on the cross-section perpendicular to the compression direction, making it difficult to accurately reflect the deformation relationship of multiple cells.

Other studies have attempted to equivalent the rhombic dodecahedron structure to an open cubic lattice structure. However, this approach faces challenges due to the significant differences in the stress and deformation of the cells. The deformation of the rhombic dodecahedron structure is primarily dominated by bending, while the cubic structure is dominated by buckling. These two behaviors cannot be treated as the same.

In this study, we performed a force decomposition analysis on rhombic dodecahedron structures with different mapping ratios. We analyzed the structures from the macroscopic level to the individual struts, taking into account the effects of various sizes and variations in the number of cells. The main focus was on the changes in the number of cells. A solution program based on analytical methods was developed to rapidly and accurately determine the load-deformation relationship for any mapping ratio and any number of cells. This approach is more targeted, faster in solving, and can address the challenges posed by a large number of cells that cannot be predicted by other methods.

In addition, to meet the specific application environment of the rhombic dodecahedron structure, a unique high-cycle fatigue model was established. Traditional fatigue calculations are primarily targeted at dense materials, and the unique characteristics of lattice structures render the existing fatigue prediction models effective only for the initial failure of the struts. However, the fact is that the failure of the first strut is far from reaching the fatigue life of the entire structure. In this study, the local maximum stress of the cell under compression-compression cyclic loading conditions was solved analytically, and an experimental approach was employed to establish a fatigue life prediction model for the cell under the load limit condition. Furthermore, post-processing techniques for modifying the cells at small scales are effectively characterized, providing support for fatigue failure analysis of a wider range of lattice structures.

1.4.2 Research objectives

The research focuses on the rhombic dodecahedron structures using Electron Beam Melting (EBM). The standard dodecahedron cells are mapped in the X direction to establish the relationship between the load and deformation of the cell structures with different mapping ratios under Z-direction compression. Subsequently, fatigue testing and numerical simulations are combined to predict the high-cycle compression-compression fatigue life using analytical methods. The specific research contents are as follows:

1) Mechanical Properties of Rhombic Dodecahedron:

The mechanical properties of Ti6Al4V rhombic dodecahedral lattice structures with different mapping ratios, fabricated using the EBM technique, are currently being evaluated. This evaluation involves testing the equivalent elastic modulus, compressive strength, and high-cycle compression-compression fatigue properties of the cells under compression conditions. Preliminary calibrations are being conducted to determine the roughness of the strut surface and the diameter of the struts. The influence of the mapping ratio on the compressive and high-cycle fatigue properties of the cells is also being studied. Furthermore, the mechanical properties of the rhombic dodecahedral cells in response to different post-processing methods are being assessed to select an appropriate post-processing regime.

2) Study on the influence of cryogenic treatment on the microstructure and mechanical properties of the material:

The microstructure characterization of Ti6Al4V alloy fabricated using EBM before and after deep cryogenic treatment will be conducted to explain the generation of substructures, the evolution of texture, and the influence of phase transformation on the mechanical properties of rhombic dodecahedron macrostructure. The analysis of fatigue fractures will also be carried out to investigate the differences in fatigue failure due to surface and geometric defects in the struts. This research aims to enhance the understanding of material property changes and provide guidance for optimizing the structure.

3) Development of analytical models for the elastic modulus and Poisson's ratio of the rhombic dodecahedron structures:

The standard dodecahedron cells are mapped in the X direction. Effective analytical models and finite element models will be established to calculate the compression equivalent elastic modulus and Poisson's ratio under both boundary-constrained and unconstrained conditions, thereby understanding the mechanical properties of the materials under compression.

4) Mechanism derived predication of the high-cycle fatigue life of the rhombic dodecahedron structures:

Expressions parameterizing the cross-sectional properties of the struts in rhombic dodecahedron structures with different mapping ratios are currently in developing. Simultaneously, an analytical model is being established to analyze the local maximum stress under compression conditions. The objective is to examine the stress distribution in structures with varying map-

ping ratios and provide a foundation for predicting fatigue performance. Additionally, extensive research is underway to investigate the high-cycle fatigue mechanisms specific to rhombic dodecahedron structures with different mapping ratios. By integrating theories of fatigue failure and notched effects, predictive formulas are being derived to estimate the fatigue life and failure modes of the structures.

Through the aforementioned research, a comprehensive understanding of the mechanical performance and life expectancy of EBM-fabricated rhombic dodecahedron structures under compressive load and high-cycle fatigue conditions will be obtained. This will provide important references for the design and application of skeletal implants and promote further applications and development of this structure in the field of biomedical engineering.

Chapter 2 Methodology

2.1 Design of the mapped rhombic dodecahedron in Ti6Al4V

A mapping ratio α characterizes a designed unit-cell of the rhombic dodecahedron structure in the X direction in three-dimensional coordinates. After mapping, the porosity of each crystal cell with different mapping ratios remained consistent at 89.1%. Three types of cells with a mapping ratio of 1, 0.7 and 0.5 were selected as typical cases to study, as shown in Fig. 1. Fig. 1(a) and 1(b), the side lengths of the single cells corresponding to the mapping direction were 5 mm, 3.5 mm, and 2.5 mm, respectively. In CAD design, the diameter of the circular section in the cell is consistent with the long axis of the elliptical section, and the diameter is 0.5 mm. The samples selected in the experiment are grid cells with three mapping ratios arrayed along the coordinate system's three directions. The external frame of the lattice grid block is defined as an equivalent homogeneous block with a side length of 25 mm. The porosity of the homogeneous block would not change with the mapping ratio, and the total volume of the solid strut represented in the CAD model is consistent. The density of the equivalent homogeneous block is related to cellular porosity.

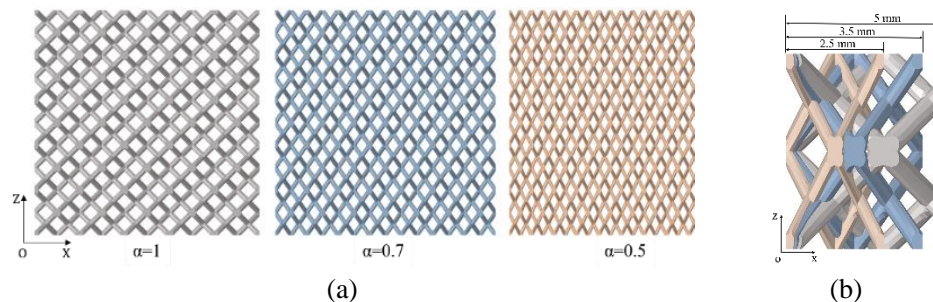


Fig. 2.1 Designed rhomboidal dodecahedral porous samples with mapping ratios of $\alpha=1/0.7/0.5$ under the same volume (a); Unit cells with mapping ratios of $\alpha=1/0.7/0.5$ (b)

2.2 Fabrication via EBM

The Ti-6Al-4V powder used in the manufacture was supplied by Arcam AB (Sweden). The average granularity of the powder was 76 μm . The porous structure was built using an Arcam A1 EBM system with a processing voltage of 60 kV. An approximately $\sim 200 \mu\text{m}$ electron beam was used, and the construction process was performed in a vacuum of 10^{-3} mbar, with controlled helium as a control gas. The process was initiated by pre-heating the powder prior to fu-

sion. For each layer, a pre-scan was performed, which scanned the powder bed 11 times with a 30 mA beam current and 15,000 mm/s acquisition speed.

2.3 Cryogenic treatment

The prepared EBM sample was placed in a double-layer thermally insulated liquid nitrogen device. The cryogenic process temperature is approximately -196°C . 48-hour cryogenic treatment has the most evident enhancement in the mechanical properties of Ti6Al4V¹⁵². Multiple cycles can improve performance even more than a single holding time. Consequently, all samples were subjected to 12 h of continuous cooling and then returned to room temperature for four cycles. After the cryogenic treatment, the samples were left at room temperature for rinsing with ethanol. Then ultrasonic cleaning equipment was used for secondary washing and dried for later use.

2.4 Microstructural characterization

The lattice microstructure was investigated and characterized using an Olympus GX-51 optical microscopy (OM, Japan), and a HITACHI S-3400N scanning electron microscopy (SEM, Japan). The samples for the OM characterization were mechanically polished and engraved in a solution containing 10 vol% HF, 30 vol% HNO₃ and 60 vol% H₂O. The phase components were examined by using a FEI Tecnai F20 transmission electron microscopy (TEM, the US) operating at 200 kV. The samples for the TEM analyses of the mesh struts were prepared by ion milling with 5- kV and 3.5- kV argon ions at an incidence angles of 4° and 6° . The samples prepared for electron backscatter diffraction (EBSD) were used for electrolytically polished in a 5% volume perchloric acid, 30% n-butanol, and 65% methanol electrolyte at a voltage of 25 V for 40 seconds. The EBSD data were collected using a Zeiss Gemini300 field-emission scanning electron microscope (Germany) in combination with an HKL EBSD camera and software. HKL Channel 5 software was used to process the data. An acceleration voltage of 20 kV and a step size of 1.2 μm were chosen for EBSD data acquisition. All maps were colored relative to the z-axis when the EBSD data were presented using inverse pole figure (IPF) coloring.

2.5 Mechanical properties

The roughness of the strut and block surfaces were measured using aby OLS4100 LEXT 3D Measuring Laser Microscope OLS4100(Japan). The uniaxial compression tests were carried out using accordance with an electronic extensometer on a WGW-100II mechanical test machine

(China) WGW-100II with a deformation rate of 0.02 mm/s. The porous- material crushing test was evaluated on the same equipment at a compression rate of 1 mm/s. The test was stopped when the struts were almost completely pulverized, and the load curve increased substantially. An extensometer was used to record the strain during loading and unloading. The mechanically polished fatigue test bars of Ti6Al4V raw material were evaluated conducted on a hydraulic testing machine (MTS 858 Mini Bionix II, the US) at ambient temperature with a stress ratio $R=-1$, and frequency of 10 Hz. As the local stress of the strut cannot be accurately obtained, the cyclic local stress is replaced by the cyclic load. The maximum stress of the strut is linearly related to the external load by the analytical method, so it is logical to replace the local stress with the homogeneous equivalent stress here [47]¹⁵³. The high- cycle fatigue test of the porous structure block was carried out on the same testing machine with an equivalent stress ratio of $R=0.1$, and a frequency of 30 Hz. Hardness tests were conducted using on a microhardness tester (THV-1MDT, China). In the fatigue test, the equipment determines that the test stopped the test when the fatigue life reached with a sudden load drop of approximately about 1 kN in one cycle. Mapping ratio variations resulted in the differences in the cyclic bearing capacities of the structures. Compared to the complete fracture of homogeneous materials, the definition of the fatigue life of porous materials is variable, and can be a percentage loss of stiffness, a sudden drop in load, or a displacement limit.

2.6 Numerical modelling

2.6.1 Finite element theory of beam element

For a bending beam deformed around z -direction, the nodal displacements and rotation angles are used as the unknown variables as shown in Fig. 2.2.

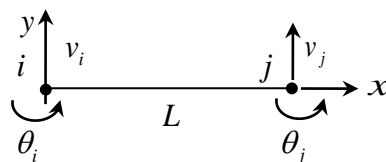


Fig. 2.2 A single beam element

By considering 4 boundary conditions on the two nodes of a beam, the displacement in the Y-direction for a beam in bending around z-direction is supposed to be a polynomial with 4 coefficients to determine as follows:

$$v(x) = ax^3 + bx^2 + cx + d \quad (2-1)$$

With small elastic deformation, the rotation angle is supposed as follows:

$$\theta(x) \approx \tan \theta(x) = v'(x) = 3ax^2 + 2bx + c \quad (2-2)$$

With the following boundary conditions:

$$v(0) = v_i; v(L) = v_j; \theta(0) = \theta_i; \theta(L) = \theta_j \quad (2-3)$$

Using Equations (2-2), (2-3) and (2-4):

$$v(x) = [N_1 \quad N_2 \quad N_3 \quad N_4] \{u\} \quad (2-4)$$

with $\Rightarrow \langle u \rangle = \{u\}^T = \langle v_i \quad \theta_i \quad v_j \quad \theta_j \rangle$, and

$$N_1 = 1 - 3\bar{x}^2 + 2\bar{x}^3; \quad N_2 = L(\bar{x} - 2\bar{x}^2 + \bar{x}^3)$$

$$N_3 = 3\bar{x}^2 - 2\bar{x}^3; \quad N_4 = L(-\bar{x}^2 + \bar{x}^3); \quad \bar{x} = \frac{x}{L}$$

Strain energy of the beam is:

$$U = \frac{EI}{2} \int_0^L \left(\frac{\partial^2 v}{\partial x^2} \right)^2 dx \quad (2-5)$$

And assuming the strain energy in form of matrix:

$$U = \frac{1}{2} \langle u \rangle [K] \{u\} \quad (2-6)$$

Using Equation (2-5) in (2-6), and comparing to (2-7):

$$[K] = \frac{EI}{L^3} \begin{bmatrix} 12 & 6L & -12 & 6L \\ & 4L^2 & -6L & 2L^2 \\ & & 12 & -6L \\ & & & 4L^2 \end{bmatrix} \quad (2-7)$$

In which:

$$K_{ij} = K_{ji} = \int_0^L \frac{\partial^2 N_i}{\partial x^2} \frac{\partial^2 N_j}{\partial x^2} dx$$

The transformation from local coordinate system to global one is:

$$\begin{aligned} [K]_l \{u\}_l = \{f\}_l &\Rightarrow [R_c][K]_l ([R_c]^T \{u\}) = [R_c]([R_c]^T \{f\}) \\ \Rightarrow [R_c][K]_l [R_c]^T \{U\} = \{F\} &\Rightarrow [K]_g = [R_c][K]_l [R_c]^T \end{aligned} \quad (2-8)$$

2.6.2 Fatigue model

Fatigue prediction needs to be based on the fatigue performance of the base metal, and the fatigue prediction model is an approximate empirical model. To establish in order to complete the establishment of the high-cycle fatigue prediction model of the rhombic dodecahedron, the fatigue test data of the base material were first fitted using Basquin's law¹⁵⁴, which is only valid for high-cycle fatigue ($> 10^4$).

$$\sigma_f = a \times N_f^b \quad (2-9)$$

where σ_f is fatigue strength in MPa, and N_f is the number of cycles to failure.

Based on Basquin's law and considering the cyclic mean stress effect using the Soderberg equation¹⁵⁵:

$$\frac{\sigma_a}{\sigma_f} + \frac{\sigma_m}{\sigma_{ut}} = 1 \quad (2-10)$$

Where σ_a and σ_m are the alternating and mean stresses respectively, and σ_{ut} is the tensile strength of the struts. This fatigue model describes a failure event corresponding to a single strut's failure where the maximum local stress happens.

This fatigue model describes a failure event corresponding to the failure of a single strut, a single strut's failure where the maximum local stress occurs.

Megahed et al.¹⁵³ modified the Gibson-Ashby classical creep model¹⁰ by replacing the deformation behavior of the foam material under a compression-compression fatigue load with an open-cell structure composed of square columns and finally expressed the prediction model with the strain rate in a single cycle. They suggested that the strain rate is highly correlated with the stress amplitude; a high-stress amplitude causes the manifestation of more deformations in the accumulated strain. Therefore, they proposed a relationship between the stress amplitude and strain rate in the cyclic ratchet effect. The amplitude and maximum stress can also be replaced by other related stresses, such as the mean stress or the difference between the maximum and yield stresses.

The strain rate is expressed by the maximum local stress of the strut and the equivalent stress of the homogeneous block, which as follows:

$$\dot{\epsilon}_N = K \sigma_{\max}^n \cdot \Delta \sigma^m \quad (2-11)$$

where K, n and m are creep constants.

McCullough et al. attributed the fatigue failure of foam aluminum alloys to the gradual build-up of strains induced by ratcheting the weakest cross-section of the material. Cracking was observed at the cell edges before the fatigue life was reached¹⁵⁶. They expressed the relationship between the fatigue life N_f , relative density $\bar{\rho}$, and load ratio R as follows:

$$\frac{d\varepsilon}{dN} = C(1-R)^p \frac{0.6}{n+2} \left[\frac{1.7(2n-1)}{n} \frac{|\sigma|_{\max}}{\sigma_0} \right]^n \bar{\rho}^{\frac{3n+1}{2}} \quad (2-12)$$

$$\frac{1}{N_f} = \frac{C(1-R)^p}{\varepsilon_y} \frac{0.6}{n+2} \left[\frac{1.7(2n-1)}{n} \frac{|\sigma|_{\max}}{\sigma_0} \right]^n \bar{\rho}^{\frac{3n+1}{2}} \quad (2-13)$$

Where C, n, p, q, σ_0 are material constants used in the ratcheting.

Chapter 3 Material properties and microstructure characterization

The analysis of the compression and fatigue performance of the rhombic dodecahedron lattice structure needs to be based on the mechanical properties of the base material. Comprehensive mechanical performance analysis and testing are necessary means to understand the deformation mechanisms of Ti6Al4V alloy and the deformation response of lattice structures. Additionally, post-processing of additive manufacturing components can influence macroscopic mechanical properties by modifying the microstructure. Prior to the use of the product, post-processing modifications can help alleviate residual stresses and achieve tailored microstructures to meet the diverse mechanical performance requirements of the components.

In this chapter, surface quality and elastic modulus of the Ti6Al4V alloy base material and the rhombic dodecahedron lattice cell prepared by Electron Beam Melting (EBM) were evaluated. Subsequently, mechanical properties such as tensile strength, elongation, compressive strength, hardness, and fatigue strength were tested. These are essential performance parameters for subsequent calculations of elastic modulus and fatigue. The compression and fatigue performance of the material were influenced by different heat treatment conditions, and the effects on the macroscopic performance were explained and analyzed through microstructural evolution, texture changes, and differences in fatigue fracture surfaces. These findings provide further insights for studying the performance of additive manufactured Ti6Al4V lattice structures.

The EBM prepared multi-mapped Ti6Al4V rhombic dodecahedron workpieces which used for mechanical performance testing in the research with mapping ratios α are 1, 0.7 and 0.5, are shown in Fig. 3.1. The results of surface roughness measurement, mechanical property testing and microstructure analysis will be detailed in this section.

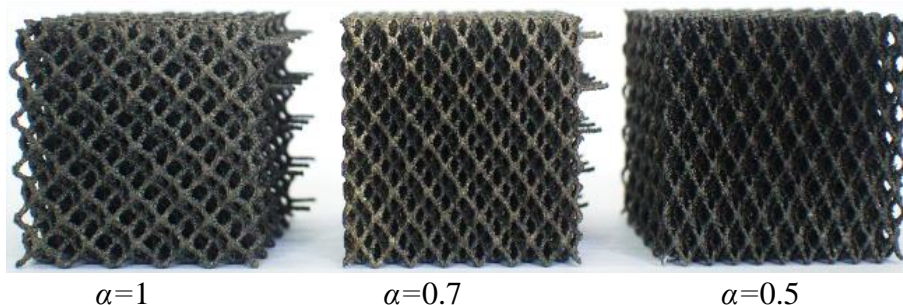


Fig. 3.1 Porous structures prepared by EBM

3.1. Samples and surface roughness

The measured surface roughnesses are measured in Fig. 3.2a and 3.2b. Parameter Ra describes the surface roughness and the average height of the 3D surface roughness. The roughness of the strut and the surface are tested separately, and the surface coefficient K_t was determined with reference to the surface coefficient definition in the commercial finite element software Fe-safe Theory manual¹⁵⁷. Owing to the influence of the electron beam accuracy and deposition direction, the surface of the printed strut was relatively rough, with an irregular geometric shape and ¹⁵²poor smoothness. The middle contained many grooves, and many unmelted metal particles were attached to the outer surface. The average diameter of the strut measured with a vernier caliper was approximately 0.64 mm; the diameter calibrated on the SEM was approximately 0.68 mm, as shown in Fig. 3.2c.

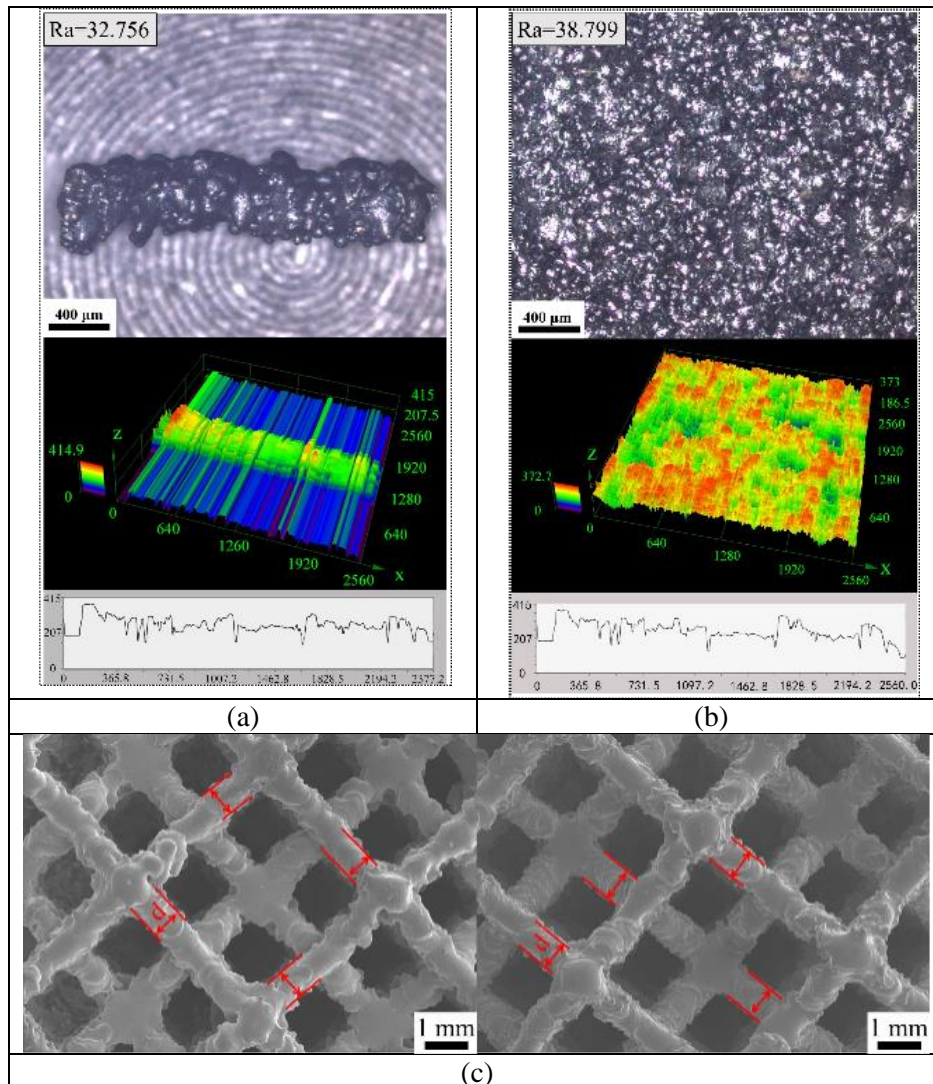


Fig. 3.2 Surface roughness and topography images of 3D-printed Ti6Al4V alloy for a single strut (a), dense surface (b), and initial measurements of strut diameter by SEM (c)

The dimensions of the homogeneous block and the surface coefficient of the rhombic dodecahedron for the fatigue test are set out in Table 3.1. Even after determining the surface roughness coefficient K_t , the diameter of the strut cannot be accurately predicted because a small change in size dramatically influences the local stress and force of the entire cell during the deformation of the strut. A previous study¹⁵⁸ demonstrated this phenomenon by analytically calculating the equivalent elastic modulus. Therefore, estimating the average strut diameter based on cell deformation under compression is more reasonable, which is discussed later.

Table 3.1 Homogeneous block dimensions and mechanical properties of base material

	Morphological characteristics				
	$d_{as\ designed}$ [mm]	$d_{as\ measured}$ [mm]	$b_{as\ designed}$ [mm]	R_a	K_t
Untreated	0.5	0.63	5	(16,40)	1.61
Cryogenic					1.57

3.2 Mechanical properties

3.2.1 Mechanical properties of base metal

1) Elastic modulus and hardness

The dimensions of the homogeneous block of the rhombic dodecahedron structure used for the fatigue test is set out in Table 3.2. After the tensile specimens were cleaned from the substrate, the post-treatment of the sample is carried out according to different heat treatment regimes. The schemes are listed in Table 3.3. The variation of elastic modulus of the material after different post-processing treatments is shown in Fig. 3.3.

Table 3.2 Homogeneous block dimensions and mechanical properties of base material

	Morphological characteristics					Mechanical properties of strut material	
	$d_{as\ designed}$ [mm]	$d_{as\ measured}$ [mm]	$b_{as\ designed}$ [mm]	R_a	K_t	Elastic modulus [MPa]	Poisson's ratio
Untreated	0.5	0.63	5	(16,40]	1.61	112177	0.36
Cryogenic					1.57	107207	

It can be observed that heat treatment has a significant influence on the elastic modulus of the material, with a maximum difference of up to 20% compared to the elastic modulus of the base material. On the other hand, the elastic modulus of the deep cryogenic treated samples differs from the base material by only 4%. Vickers hardness of Ti6Al4V base material under different post-treated conditions are shown in Fig. 3.4. Similarly, to the trend observed for elastic modulus, the hardness of the material shows significant variations after heat treatment, with a

maximum difference of up to 19.3%. On the other hand, the Vickers hardness of the material after deep cryogenic treatment remains nearly the same as the untreated state.

Table 3.3 Tensile properties of base metal under post-treatments

Number	Heat-treatment	Cryogenic treatment	Aging treatment
1-1	840°C × 2h/Air cooling	-	-
1-2	840°C × 2h/Air cooling	○	-
2-1	940°C × 1h/Quenching +540°C × 4h/Air cooling	-	-
2-2	940°C × 1h/Quenching +540°C × 4h/Air cooling	○	-
3-1	540°C × 4h/Air cooling	-	-
3-2	540°C × 4h/Air cooling	○	-
4-1	940°C × 1h/Quenching	-	-
4-2	940°C × 1h/Quenching	○	540°C × 2h
5	-	○	-
6	-	○	540°C × 2h
7	-	-	-

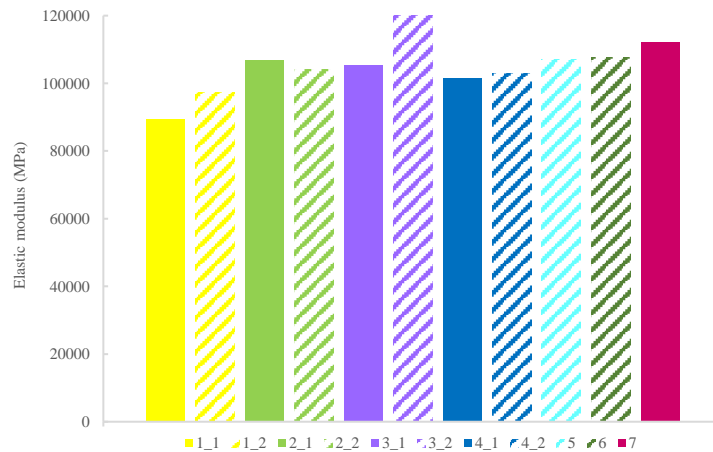


Fig. 3.3 The influence of post-processing on the elastic modulus

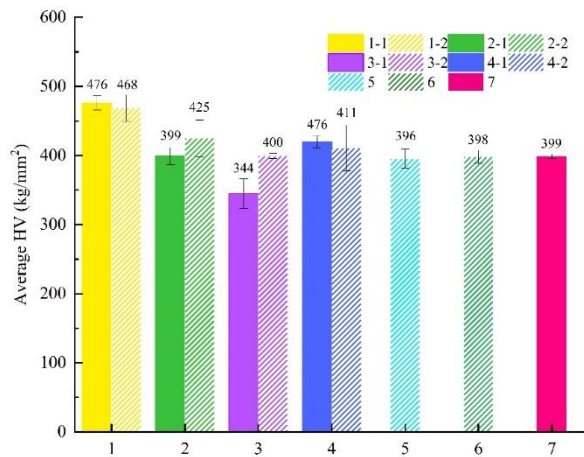


Fig. 3.4. Vickers hardness

2) Tensile test

The tensile direction of the uniaxial tensile sample prepared by EBM is the growth direction of additive manufacturing, which is shown in Fig. 3.5. The uniaxial tensile curve of Ti6Al4V base material under different post-treated conditions are shown in Fig. 3.6. The specific values of strength and elongation are shown in Table 3.4.

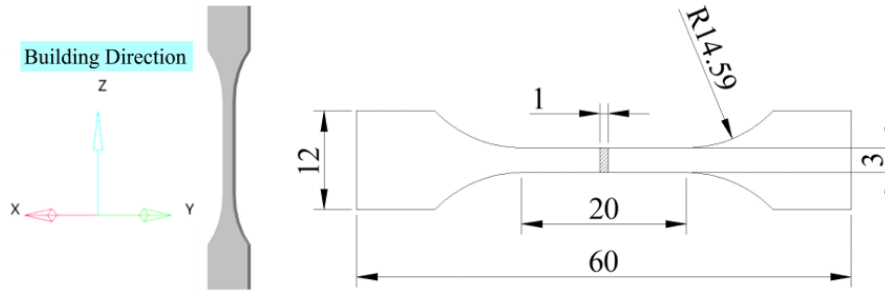


Fig. 3.5 Dimensions and building direction of tensile specimens

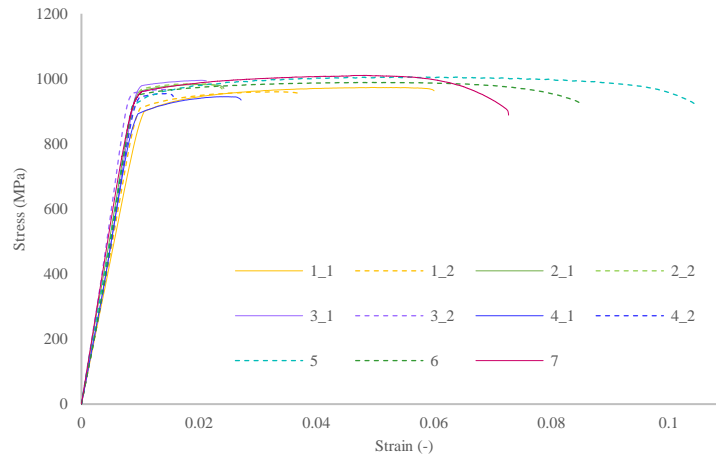


Fig. 3.6 Uniaxial tensile stress-strain curves

Table 3.4 Tensile properties of base metal under post-treatments

Number	σ_b (MPa)	σ_y (MPa)	δ (%)
1-1	937.46	899.1	4.6
1-2	959.91	909.	3.4
2-1	982.86	961.76	3.0
2-2	984.74	969.29	3.3
3-1	995.51	978.94	1.6
3-2	967.38	955.87	1.6
4-1	944.9	892	3.6
4-2	954	945	1.8
5	1006.03	917.56	10.5
6	988.84	949.77	8.8
7	1010.54	960.1	7.27

Combined with the test results, it is found that the optimization of metal by heat treatment almost only improves the hardness of the material, while the strength and plasticity are significantly reduced. The hardness of the sample after cryogenic treatment is almost the same as that of the original sample, and the strength is not decreased so much, but the plasticity is significantly improved. After cryogenic treatment, the average yield strength of the material decreased by approximately 3.6%. In contrast, the average elongation increased by approximately 56%. The average values of Vickers hardness and tensile strength after cryogenic treatment are basically at the same level as that of the base metal. Remarkably, the cryogenic treatment significantly enhanced the ductility of the material while maintaining comparable levels of strength and hardness.

3) High-cycle fatigue test

The loading direction of the fatigue sample prepared by EBM is the growth direction of additive manufacturing, which is shown in Fig. 3.7. The Basquin curve was fitted according to the high cycle fatigue data of the test bars. Generally, the fatigue life is assumed to be endless when the number of cycles exceeds 10^7 . However, the cost of cyclic stress control associated with this fatigue limit is insufficient; therefore, the test results of 10^4 to 3×10^6 cycles were chosen as valid data. Fig. 3.8 illustrates the fatigue test results and the S-N fit curve. The fatigue properties of the base material improved after cryogenic treatment, and the fatigue limit increased by approximately 10%. The fitted Basquin's constants are given in Table 3.5.

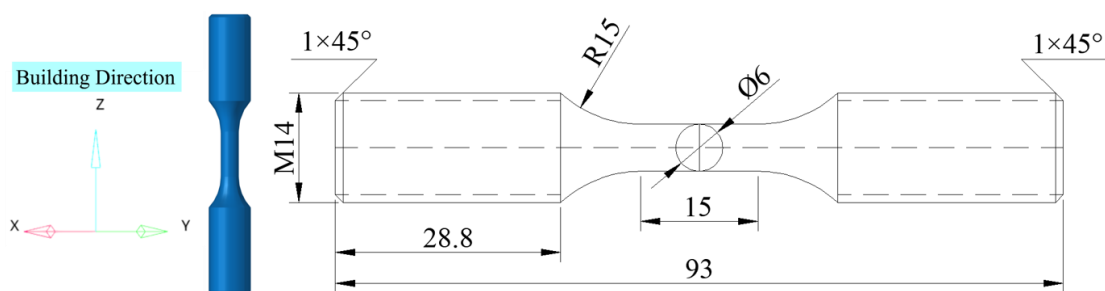


Fig. 3.7 Dimensions and building direction of fatigue specimens

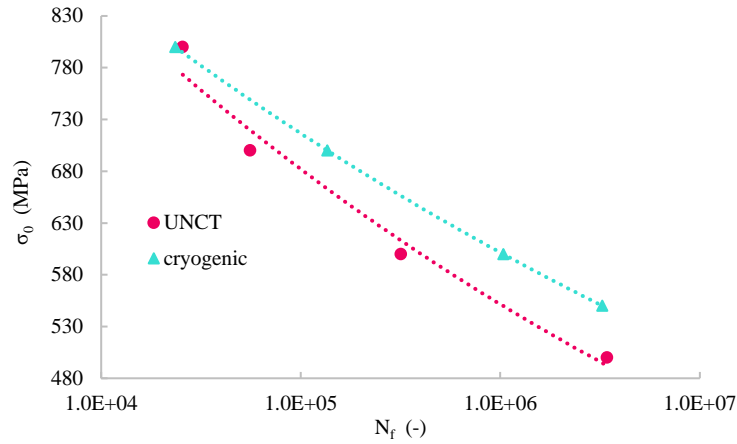


Fig. 3.8 Fatigue tests and fitting S-N curve

Table 3.5 Constants of Basquin's S-N curve of base materials

	Unprocessed	Cryogenic
a	1971.6	1718.9
b	-0.092	-0.076

3.2.2 Mechanical properties of Rhombic dodecahedron

1) Equivalent elastic modulus

High-magnification images of struts with three mapping ratios detected by Scanning Electron Microscope (SEM) has been presented in Fig. 3.9, which are the unmapped orientation: a, the mapped orientation: b, and a single strut: c. The struts are mapped along the X-direction, with the number of cells remaining constant in the unmapped direction and a corresponding increase in the number of cells in the X-direction. The equivalent dimensions and porosity of the specimens remain unchanged and the cross-section of the struts gradually changes from circular to elliptical. The long axis of the ellipse equals to the diameter of the original circular cross-section, which could be measured in Fig. 3c. The average actual diameters are approximately 5.70 mm, 5.52 mm and 5.33 mm for α of 1, 0.7 and 0.5 respectively. For the additively manufactured lattice structure, the strut grows in an inclined direction to the substrate, the surface is covered with a large number of metal particles formed by rapid cooling of the electron beam sweep and exhibits strong irregularities, and the texture accumulated on the surface of the struts are clearly visible, which has a serious impact on the surface roughness of the product^{51,159,160}.

In this case, the diameter of the strut cross-section can be defined as the inner diameter surrounded by a smooth surface and the average outer diameter surrounded by an external layer of metal particles. Besides the effects of deviations between the actual print dimensions and the

design dimensions, the discrepancy between the inner and outer diameter on the strut comes from the effect of surface roughness, and thus affects the mechanical properties of lattice structure^{161,162}.

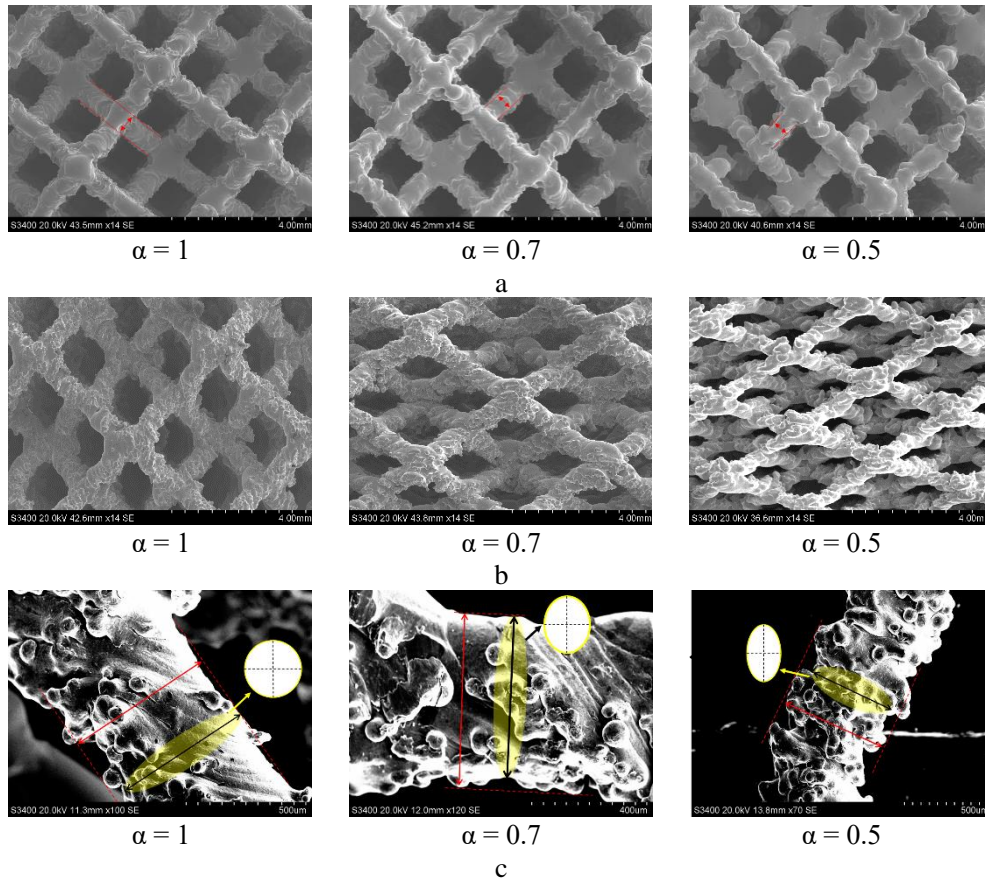


Fig. 3.9 Struts topography with different mapping ratios by SEM: a unmapped orientation; b mapped orientation; c Strut sections with different mapping ratio

As α becomes smaller, the area of the metal particle layer covering the surface of the strut becomes larger, resulting in the actual short axis length of the elliptical strut being significantly higher than the design value. The tested elastic modulus is shown in Fig. 3.10. Among the three mapping ratios, the equivalent elastic modulus is lowest when $\alpha=1$, and as α decreases monotonically, the equivalent modulus increases. Additionally, the samples after deep cooling exhibit slightly lower equivalent moduli compared to their untreated counterparts, indicating that deep cooling treatment reduces the rigidity of the alloy to some extent. To fully understand the reasons behind this, further analysis is required, considering the evolution of the microstructure.

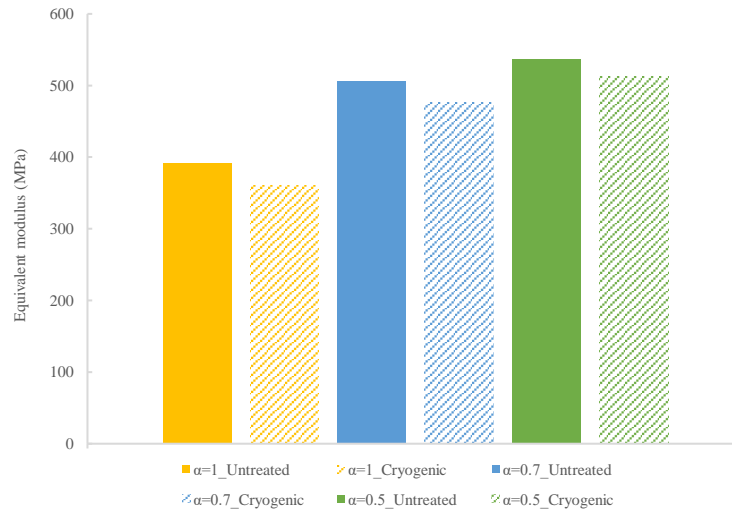


Fig. 3.10 Equivalent elastic modulus of the cells

2) Crushing tests

Crushing tests were conducted on the samples of the mapping ratios(1/0.7/0.5) for untreated and cryogenic treated state, and the results are illustrated in Fig. 3.11. The porosity of the structure does not change with the mapping ratio α . However, when the α decreases, the compressive strength and equivalent elastic modulus of the cells increases, which is consistent with the results calculated by the analytical method¹⁵⁸. Although the elastic modulus of the base material decreased after cryogenic treatment, the block's equivalent compressive strength and elastic modulus increased slightly. It can be found from the curves that there are multiple peaks in the process of crushing, which is the manifestation that the contact surface between the cells and the clamp begins to collapse layer by layer due to boundary effects. The compressive strength of almost every layer of the cryogenic sample is higher than that of the untreated one. The strut in the regular lattice structure ($\alpha=1$) has a large angle from the compression direction in space, so the compressive strength of the cell is obviously not ideal for the structure whose deformation is dominated by bending. The compressive deformation is more severe under the same load, and the compressive strength is obviously lower than that of the mapped structure.

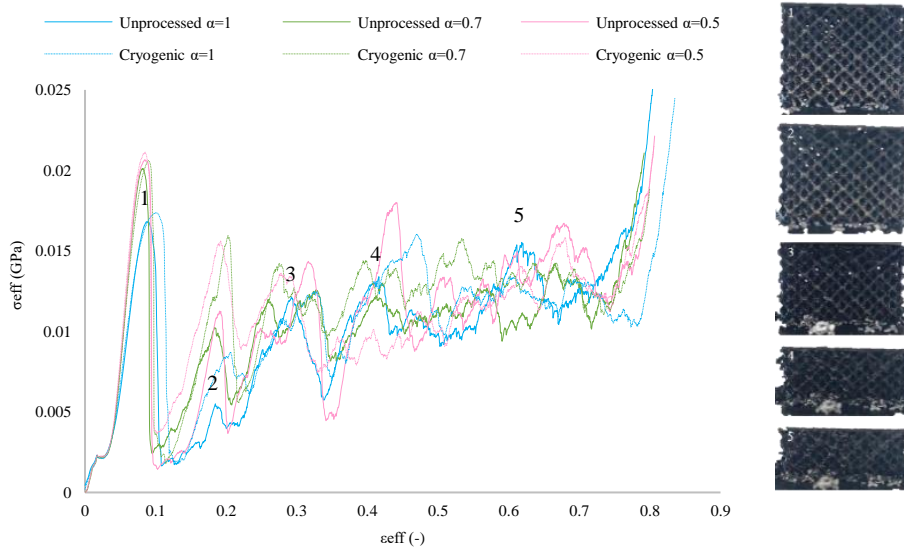


Fig. 3.11 Crushing tests

3) Fatigue tests of cells

As the local stress of the strut cannot be accurately obtained, the cyclic local stress is replaced by the cyclic load, that is, the equivalent stress of the homogeneous block is shown in Fig. 3.12. The previous work has made it clear that the maximum stress of the strut is linearly related to the external load by the analytical method, so it is logical to replace the local stress with the homogeneous equivalent stress here. In the fatigue test, the equipment determines that the test stops and the fatigue life is reached when the load suddenly drops 1kN in one cycle. The cyclic bearing capacity of samples with different mapping ratios is obviously different. In contrast to complete fracture of homogeneous material, there are various types of definitions for the maximum number of cycles in fatigue testing, which can be a percentage loss of rigidity, a sudden drop of the load, displacement limitations or a certain number of cycles reached.

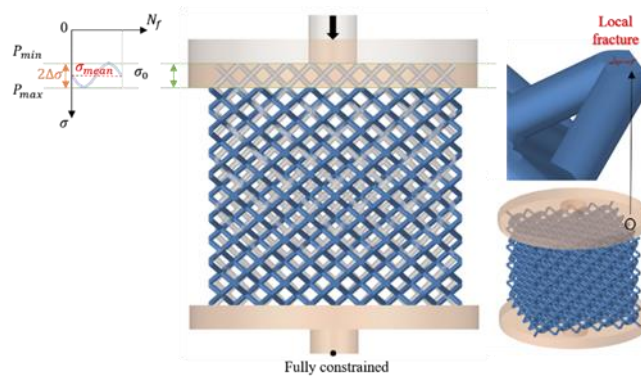


Fig. 3.12 Compression-compression fatigue of rhombic dodecahedron

Fig. 3.13 shows the deformation of samples with different mapping ratios samples prepared by EBM under a high cycle load compression-compression fatigue test after cryogenic treatment. Under the same conditions, the samples are arranged in decreasing order from left to right according to the cyclic load in decreasing order.

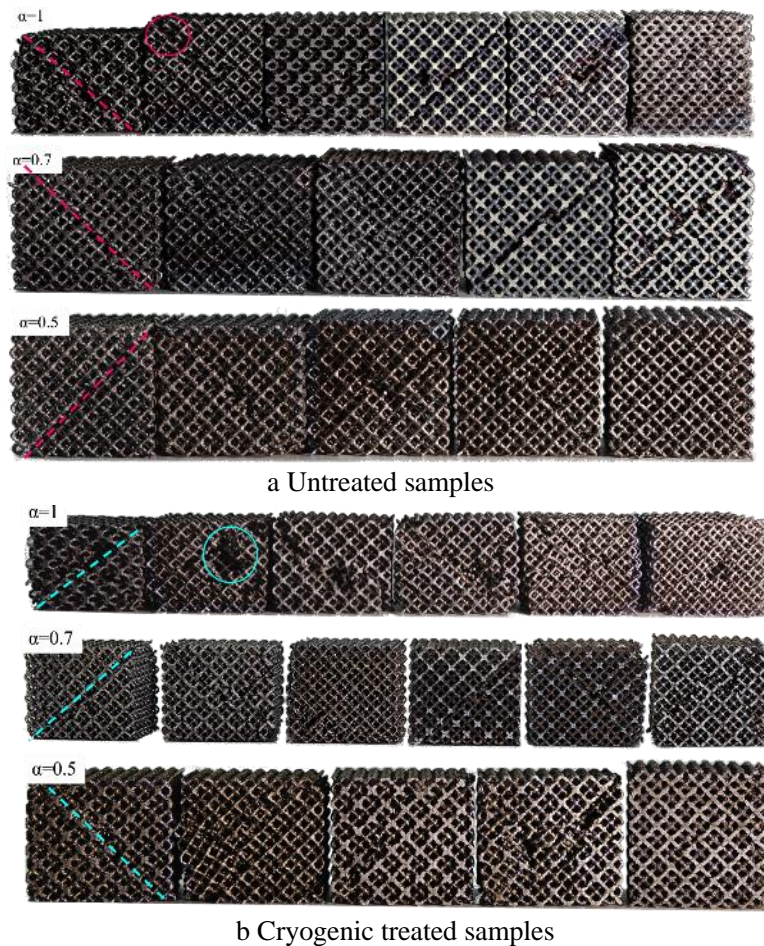


Fig.3.13 Fatigue failure of the cells

The plastic deformation accumulated after fatigue failure accumulated more under a larger cyclic load. A 45° failure of the extrusion zone, marked by the highlighted dashed line, appeared for all specimens under the loading conditions. As shown by the circle marked in the figure, owing to the unsatisfactory plastic performance of the untreated sample, one or more irregular strut aggregates on the sample broke away from the surface of the block at a certain speed during the process of compression process. The sudden absence of these aggregates caused the collapse of the cell body in the direction of compression, triggering the load limit of the system and ending the fatigue tests. The cyclic ratcheting strain was the main factor causing fatigue failure, which increased significantly in the late stage of fatigue failure. Increasing the

angle of the strut angle can reduce the influence of the strut bending deformation, thereby reducing the cyclic the strut to reduce the strut's cyclic ratcheting strain during the fatigue failure process. Simultaneously At the same time, the bending contribution to the joint is also reduced, and the local stress reduction of the joint delays the crack formation and propagation caused by surface roughness or internal defects.

The results show that when $\alpha=1$, the accumulation of deformation in the compression direction of fatigue failure is smaller than that of the cell structure with lower α values. Cryogenic treatment significantly improved the plasticity of the material. During fatigue fracture, the aggregates dropped but did not step away. At this point, the cells continued to collapse along the extrusion area, and the accumulated deformation was greater than that of the untreated sample. As a bone implant, this mild destruction mode is likely provided by better plastic properties with greater damping and excellent energy absorption performance.

3.3 Characterization of microstructure evolution

The evolution of the microstructure leads to differences in the macroscopic mechanical properties. In the study, the microstructure of EBM-fabricated Ti6Al4V and the mechanism of microstructural evolution after deep cooling treatment were investigated through metallographic analysis.

3.3.1 Metallographic observation

The longitudinal section of the metallograph parallel to the direction of formation is shown in Fig. 3.14a for the untreated sample and in Fig. 3.14b for the sample after cryogenic treatment. From the microstructure of the low-magnification SEM images, both specimens have similar phase composition. After electron beam scanning, the alloy rapidly dissipated heat to both sides of the matrix and the molten pool during solidification, and the columnar primary β -grains in a state of nearly millimeter deposition grow epitaxial from the top to the bottom of the image. Large columnar grains resulted from the temperature gradient along the direction of accumulation. During the deposition process, the bottom plate and deposition material acted as heat sinks, and the electron beam provided the heat source from above. The deposition of each beam will dissipate the heat from top to bottom, from the center to the edge. A significant feature of the microstructure of the Additive fabricated titanium alloy is the formation of coarse primary β -columnar grains, whose structure and texture direction are consistent with the structural direc-

tion of printing¹⁶³. The adjacent long strips of β -columnar grains were separated by grain boundaries α -Ti phase. The grain boundaries of the primary β -grains are marked by yellow dashed lines, while some stomatal defects can be found in the cross-section. Each β -columnar grain contains a lamellar α -Ti phase and a small amount of β -Ti phase wrapped in α -Ti phase. They were arranged approximately in a crisscrossed arrangement with α -Ti clusters, and no obvious grain boundaries are found between them.

The α -phase clusters with different sizes are distributed in the primary β -grains in an approximate orientation shown in Fig. 3.14c. During cooling, the primary β -grains decompose through the non-diffusive shear form to form the aciculate α' martensite phase. The solidified metal swept by the electron beam is heated and melted by the heat of the electron beam in the continuous base layer around it and in the stacking direction. When the subcooling degree decreases, the nucleus first formed at the grain boundary and grew into a network grain boundary α -Ti phase. In the temperature reduction process, the α -Ti phase at the grain boundary nucleated and precipitated, and some lamellar α -grain grew from the grain boundary into the grain to form a lamellar structure. The coarse primary β -grain and the complete grain boundary α -Ti phase characterized the lamellar structure. the lamellar α -Ti phase is a woven basket network, and the secondary β -Ti phase with few components is parallel to each other. The printed products cooled slowly as the temperature gradually moved away from the heat source. The microstructure changed into a mixture of $\alpha+\beta$ Weistensite structure with α -Ti clusters, reticular structure and massive structure.

After cryogenic treatment, a portion of α -Ti phase clusters was transformed into basket networks, as shown in Fig. 3.14d. The thickness of the lamellar α -grains in the microstructure was further refined. When the cryogenic holding time exceeds 48h, the thickness of the lamellar α -grains in the microstructure was further refined. It has been pointed out in some studies that when the holding time is short, such as 12h, the thickness of the lamellar α -grains decreases slightly, accompanied by the dispersion distribution of some fine α -grains, but the level of grain refinement and distribution uniformity is far less than that of the holding time of 48h. When the holding time increases from 48h to 96h, the refining process approaches saturation with the precipitation of α -grains. The conclusion is that the thickness of the α -grain is almost unaffected by the holding time when the cryopreservation time is more than 48h¹⁵².

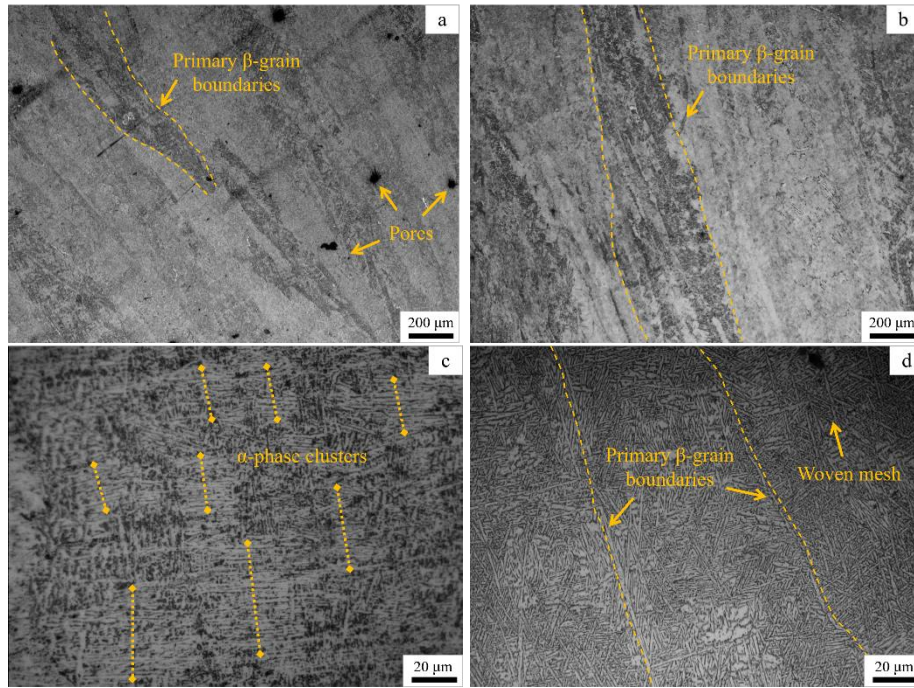


Fig. 3.14 Optical microstructure of EBM Ti-6Al-4V for untreated state: a, c; and cryogenic treated state: b, d

The surface of Ti6Al4V samples before and after cryogenic treatment was scanned by XRD, and the test results were processed by Jade 6 software, and the obtained phase analysis results are shown in Fig. 3.15. The diffraction peaks corresponding to the 2θ angle of Ti6Al4V samples measured in the test were compared with the standard diffraction patterns of α -Ti phase and β -Ti phase. The diffraction peaks corresponding to each 2θ angle matched the corresponding α -Ti phase and β -Ti phase crystal plane, which are $(10\bar{1}0)\alpha$, $(0002)\alpha$, $(10\bar{1}1)\alpha$, $(10\bar{1}2)\alpha$, $(200)\beta$, $(10\bar{2}0)\alpha$, $(10\bar{1}3)\alpha$, and $(11\bar{2}2)\alpha$, respectively.

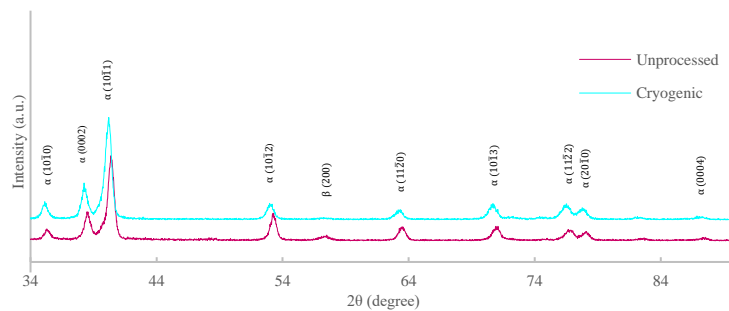


Fig. 3.15 XRD diffraction pattern

3.3.2 EBSD analysis

The inverse pole figure (IPF) map is shown in Fig. 10(a) and 10(b), where the basal plane $\{0001\}$ is labeled in red, and the prismatic planes $\{\bar{1}2\bar{1}0\}$ and $\{01\bar{1}0\}$ are labeled in green and

blue, respectively. The black lines represent low-angle grain boundaries (LAGB) ($2^\circ < \text{LAGB} < 15^\circ$), and the grey lines represent high-angle grain boundaries (HAGB) ($15^\circ < \text{HAGB}$). According to the statistics, the average grain size is $6.33\mu\text{m}$. IPF is an effective method to distinguish the α -Ti clusters from the lamellar α -grains' appearance¹⁶⁴. The LAGBs of the untreated samples were mainly concentrated at the grain boundaries and α -Ti clusters were generally present around them, which are enclosed by the white curves in Fig. 3.16 (a). However, among the various microstructures of Ti6Al4V, the alloys with the lamellar α -grains accompanied by clusters show more intense anisotropy¹⁶⁵. The color gradients of the coarse primary β -grains and α -Ti clusters indicate the existence of grain orientation gradients in the IPF coloring diagram. The stress concentration at the grain boundary results in an orientation gradient, leading to the initiation and proliferation of dislocations and sub-grain generation. After cryogenic treatment, the average grain size was approximately $4.62\mu\text{m}$ with evident refinement. The LAGBs, which are concentrated at the primary β -grain boundary, existed both at the grain boundary and in the grain after refinement. Metal volume shrinkage led to the extrusion of grains, and the plastic deformation that cannot be recovered will accumulated in the weaker phase. Residual stresses accumulated during growth can cause local plastic deformation, resulting in these sub-grain structures, that which represent adaptive strain adjustment within the material¹³⁰.

The printing strategy affects the shape of primary β -grains, showing strong texture, which corresponds to the preferred direction of heat flow provided by the temperature gradient during solidification, namely the deposition direction and scanning direction¹⁶⁶. Fig. 3.16c and 3.16d shows the pole figures of the untreated and cryogenic samples, respectively. Fig. 3.16c shows a strong α -Ti texture with a maximum intensity of 37.8 times the random texture in the $\{0001\}$ pole figure rotating in the direction of 60° on the orthogonal z-axis, which is highly symmetrical and has high-intensity clustering in the deposition direction. This indicates that the orientation of the α -Ti phase in additive manufacturing may be controllable. According to the research, the change in crystal orientation can significantly affect the slip and cause a difference in mechanical properties. In general, the basal plane $\{0001\}$ shows the highest Young's modulus, as well as the highest microhardness and mechanical strength¹⁶⁴. After cryogenic treatment, the distribution of orientation diffused and the intensity of the α -Ti texture component presented in the $\{0001\}$ pole figure decreased to 15.3 times the random texture component and 10 times the random texture component rotating at 120° relative to the orthogonal z-axis. The change in the

grain orientation resulted in a disparity in the mechanical properties.

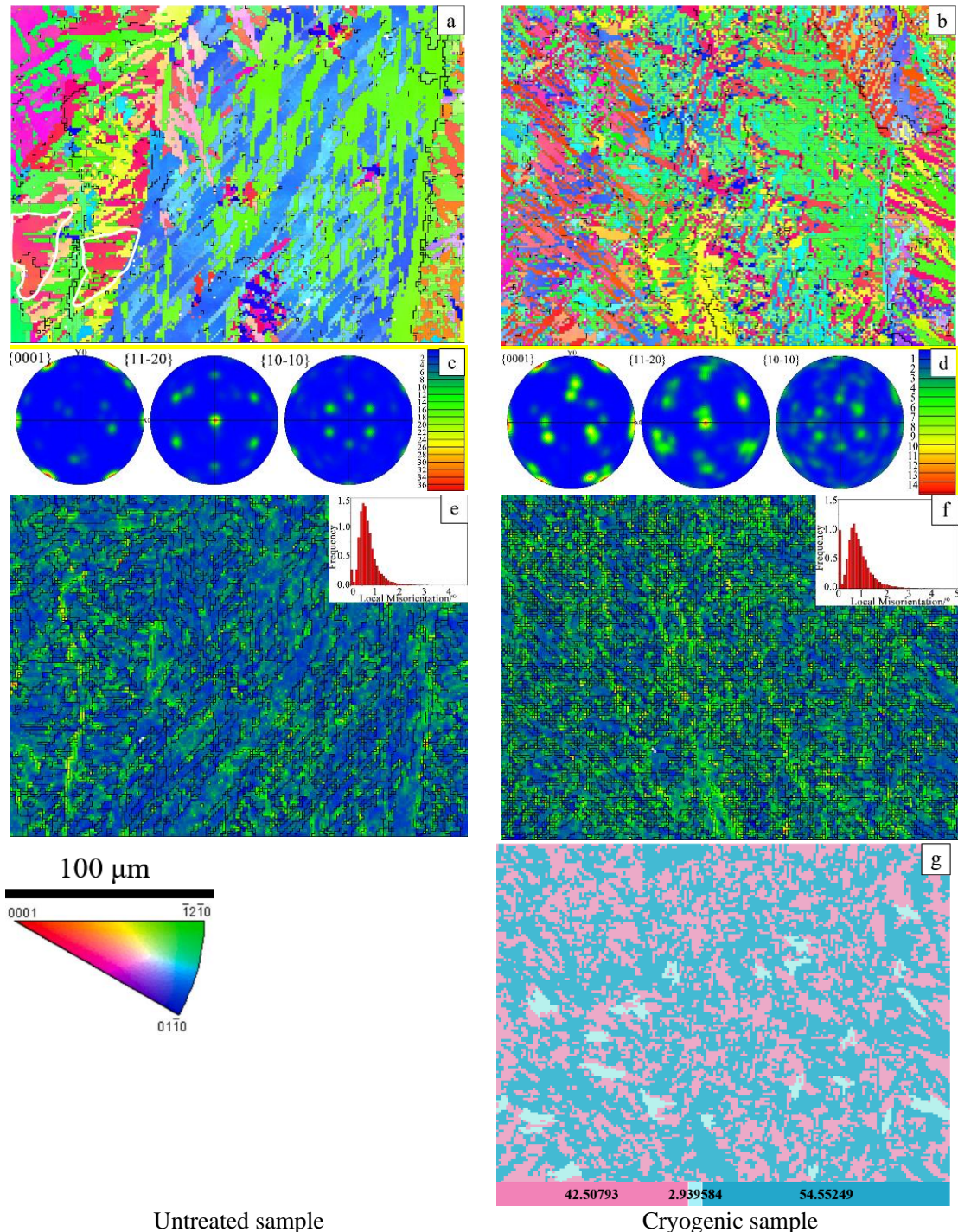


Fig. 3.16 The EBSD diagram of Ti6Al4V alloy for untreated and cryogenic-treated samples: IPF map: a, b; PF map: c, d; KAM diagram: e, f; Recrystallization fraction map: g

The local orientation difference between the untreated and cryogenically-treated materials are shown in Fig. 3.16e and 3.16f, respectively. The movement of the dislocations to the grain boundary was blocked, and the dislocation accumulated, resulting in stress concentration. The

KAM diagram of the untreated sample clearly shows the highest dislocation density at the coarse primary β -grain boundary, which is also the aggregation position of the α -Ti clusters. After cryogenic treatment, the metal lattice was distorted and the intracrystalline dislocations proliferated. Grain refinement also increased the total grain boundary area, and the distribution of local orientation differences was more random. A certain level of recrystallization occurred under periodic temperature changes and was randomly distributed inside the metal. These proportions are shown in pink in Fig. 3.16g.

3.3.3 TEM analysis

The samples were analyzed using TEM for a fine microstructural morphology. As shown in Fig. 3.17a and 3.17b, the lamellar α -grains of the untreated samples were arranged in parallel, and a few fine β -grains are included. These α -Ti clusters were surrounded by pluggy dislocation bands, consistent with the region of LAGB in the previous EBSD analysis and the area of high dislocation density in the KAM diagram. After cryogenic treatment, α -Ti clusters decomposed into an $\alpha+\beta$ staggered arrangement, showing a large area with an interwoven state, as shown in Fig. 3.17c and 3.17d. Simultaneously, a large number of substructures appeared in the grain, and the dislocations were more dispersed. The decomposition of clusters results in a change in mechanical properties.

Under conventional loading conditions, Ti6Al4V alloys have difficulty generating twins under conventional loading conditions, and plastic deformation occurs via dislocation slip^{167,168}. The deformation mechanism is affected by the grain size and orientation, which depend on the difficulty in activating the slip system^{169,170}.

The addition of Al element to the Ti6Al4V alloy enhanced the activation of the basal slip system and formed three types of slip systems that can be activated at room or deep cold temperatures. Meanwhile, as the stable element of α -Ti shown in Fig. 3.17e, Al was enriched in α -Ti phase, which can significantly increase the α/β -Ti phase-transition temperature and expand the α -Ti phase region. The hexagonal close-packed (HCP) lattice structures along the basal plane $\{0001\}$ and prismatic plane $\{01\bar{1}0\}$ in the slip system were easily activated, with a preference for prismatic slip and simultaneous basal slip¹⁷¹⁻¹⁷⁵.

V was enriched in the β -Ti phase as a stable element of β -Ti. With the extension of cryogenic treatment holding time, a decrease in the atomic diffusion ability led to a significant de-

crease in the solubility of V in the β -Ti phase and precipitation, as shown in Fig.3.17f. Subsequently, due to the absorption of the V element by α -Ti phase, the lattice structure changes, resulting in the thickness of the α -Ti decreases. The morphology of these secondary α -Ti phases appears as small granules distributed around the laminated α -Ti phase and wrapped by the β phase. This phenomenon is found in Ti6Al4V prepared by EBSM and reported in the study of other alloys^{176,177}. This is due to the severe lattice distortion caused by the local stress concentration at low temperatures, which initiates a large number of dislocations and blocks the slip system of HCP α -Ti. With the increasing of cryogenic treatment time, the dislocations proliferated and strain energy increased. Simultaneously, strong internal stress promoted the generation of sub-grains at low temperatures to release high strain in the alloy¹⁷⁸.

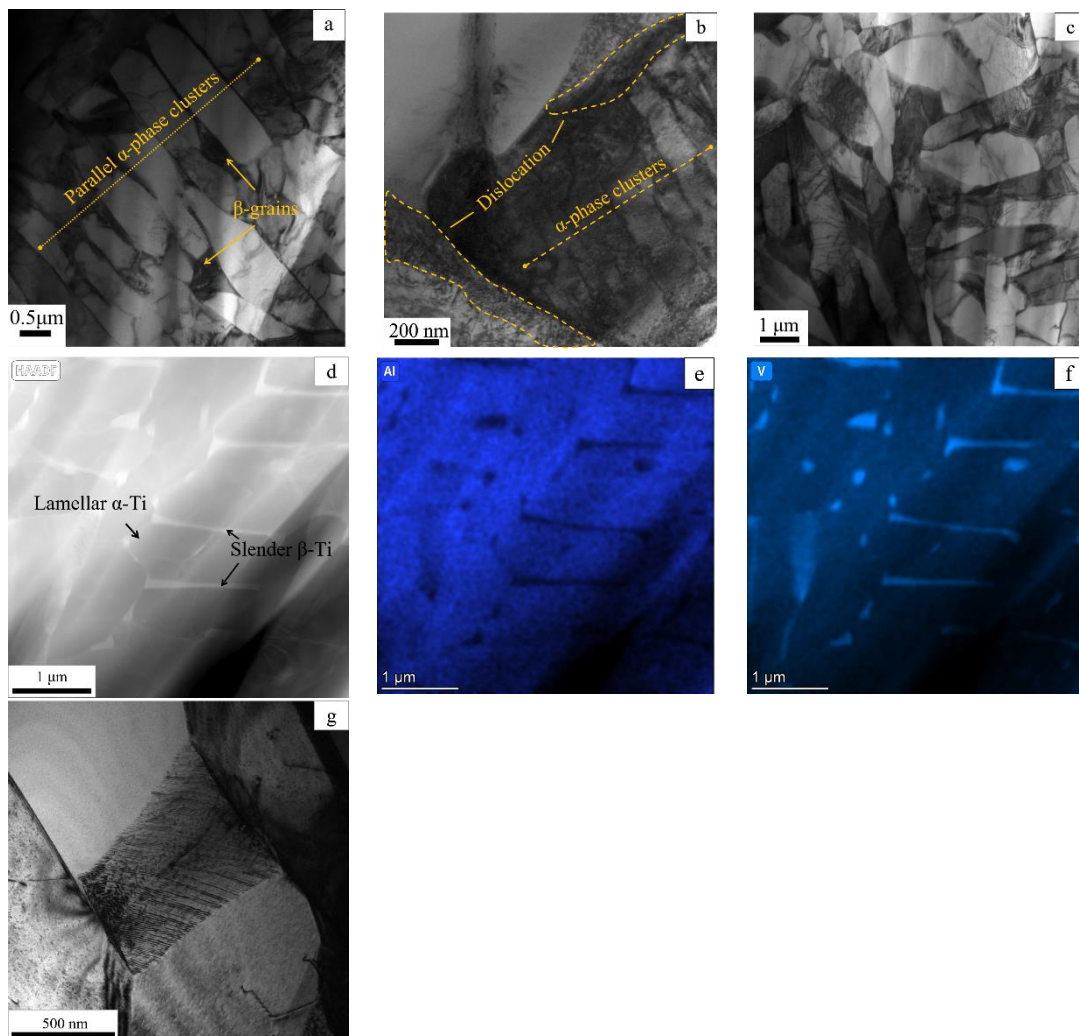


Fig. 3.17 TEM analysis for untreated state (a, b), and cryogenic state (c-g)

Fig. 3.17g shows layered α -grains surrounded by equal-thickness striations with numerous substructures. The proliferating dislocations in the original α -grains are rearranged into bands of

dislocations by sliding or climbing, and the heterotropic dislocations offset each other¹⁷⁹. The metastable microstructure is decomposed along the dislocation band to generate new α sub-grains¹⁸⁰.

When the samples gradually returned to room temperature, the low-angle grain boundaries regenerated into standard grain boundaries, and the new α -grains generated by decomposition no longer maintained their original ordered grain-boundary-angle arrangement. At this time, the metastable β -Ti phase in the system was dissipated and the lattice tended to be stable.

3.4 Fracture morphology analysis

3.4.1 Failure analysis of joint

Fatigue crack initiation rule and fracture mechanism were analyzed by fatigue fracture morphology. It is found that the failure of rhomboidal dodecahedron under high-cycle fatigue loading occurs at both joints (Fig. 3.18) and struts (Fig. 3.19). Although the local stress at the joint is the highest, the texture line on the surface of the strut is also prone to crack initiation. The technical characteristics of EBM often lead to the surface roughness of complicated designed products. According to the scanning strategy, fatigue failure of the joint is mostly presented in the form of petal-like spalling of the part bordering one end of the strut, as shown in Fig. 3.18a. At the fracture of the joint, the fracture plane at different angles is almost perpendicular to the axial direction of the corresponding strut, and the residual peel layer can still be found on some of the fractures, as shown in Fig. 3.18b. Because of the difference in grain growth direction at the joint, the joint center of the two struts is prone to produce gully cracks after fatigue fracture. The radial stripes of fatigue crack propagation can be seen on the fracture planes on both sides of the crack, as shown in Fig. 3.18c.

There are two prevailing views on the initiation of fatigue cracks, one is that they are caused by internal defects^{6,142,181}, and the other is that they are caused by irregular external surfaces^{118,120}. The two fracture modes occurred in opposite directions. From the analysis of the fracture morphology, there were some unmelted metal particles inside the metal, which were insignificant compared to the texture lines and a large number of unmelted particles on the outer surface of the strut. There are multiple crack sources around the strut section. The cracks meet on the outer surface and then extend inward to form the main crack. Final ductile tearing occurs when the main crack advances to the internal defect. In other words, although the crack leading

to the final fracture was generated at the internal defect of the strut, the multiple crack sources converged into the main crack are generated on the external surface of the strut, which confirms that the joint is the key position of the fatigue fracture of the cells.

As shown in Fig. 3.18d, the texture layer of the strut is obviously peeled off on the joint section's outer surface, which shows two distinct cross-section morphologies from the metal inside the joint. The section of the texture layer is neat and smooth, like brittle fracture. The crack on the section of the joint extends from outside to inside in multiple directions and is clearly visible with the separation layer after the fracture of the strut. There are completely different fracture mechanisms between them. The angle of construction between the adjacent struts is displayed through the cross-section of the fracture. In this study, it is considered that the initial crack source of fatigue failure generally appeared in the texture layer on the outer surface or the unmelted and sintered Ti6Al4V metal powder particles attached near the joint without considering the existence of fatal pore defects inside the strut. Therefore, a smooth surface is critical for preparing open-cell structures using AM¹⁴⁶.

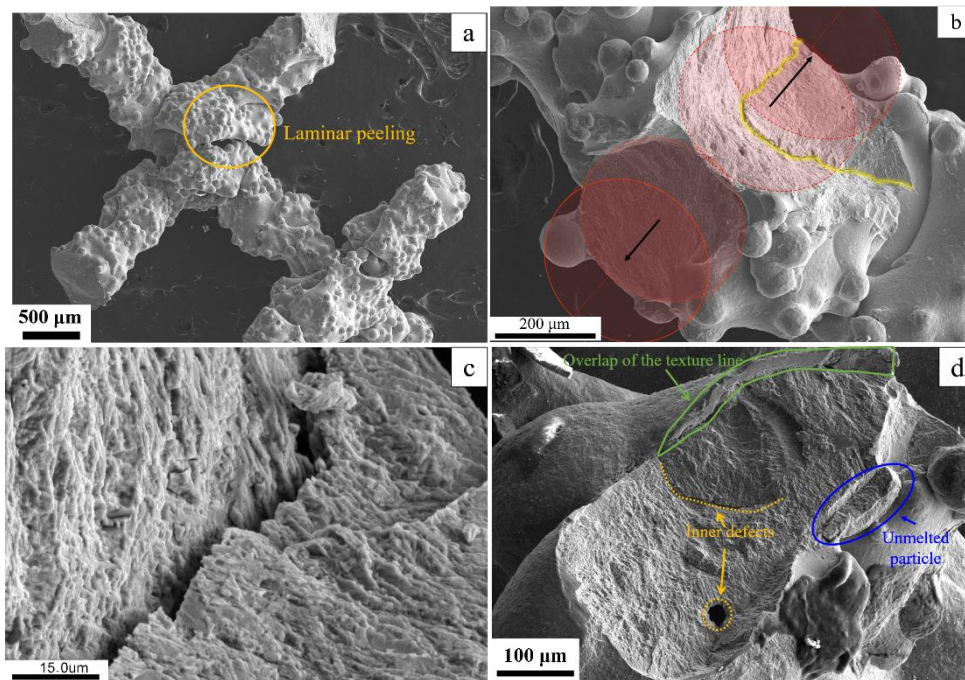


Fig. 3.18. Fatigue fracture morphology on joints

3.4.2 Failure analysis of struts

As shown in Fig. 3.19, two typical areas are displayed from the fracture in the middle of the strut. Region 1 is the radial flow zone of the brittle fracture mechanism, which shows a typ-

ical corrugated fracture, representing the rapid advance from crack initiation to crack propagation. Region 2 is a typical ductile fracture dimple region, and the aggregated pits represent the tearing process of the crack that eventually breaks instantaneously¹³⁰. Similarly, fatigue cracks begin in the metal particles or layers of texture attached to the surface and extend to the center of the strut.

There are surface defects at the initiation of cracks, which begin to expand into the section after several cycles. The final fracture occurs when the remaining jointed area of the material is too small to withstand the maximum cyclic load. The radial ridge appears as a trans-granular crack of α -grains, the initiation period of the crack is short, and the micro fringe on the grain surface expands in the crack region¹⁸². It is speculated that the crack evolution process is a rapid fracture from a trans-granular crack to a typical fatigue crack and then to a final dimple shape.

The orientation of the fatigue fringe varies with the grain, and the dimple morphology is characterized by micropore condensation in the final rapid fracture zone. The fatigue cracks in these dimple accumulation areas appear smooth in low magnification SEM which is difficult to observe¹⁸³.

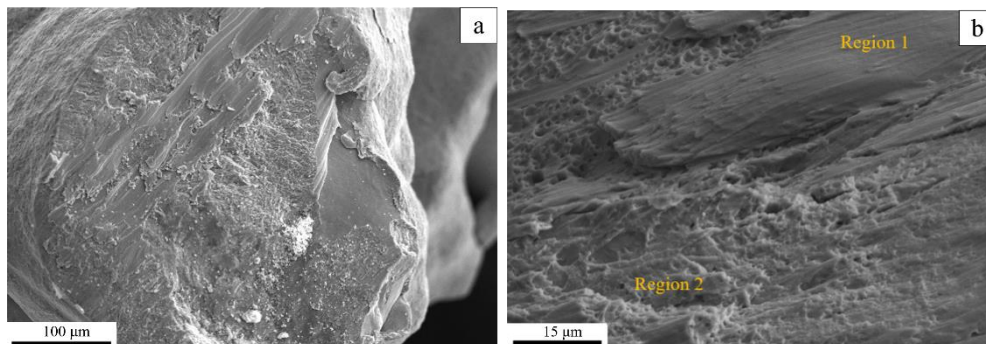


Fig. 3.19 Fatigue fracture morphology on struts

3.4.3 Effect of cryogenic treatment on fatigue fracture

In order to investigate the difference of fracture mode caused by cryogenic treatment, the fracture morphology before and after cryogenic treatment was analyzed. Fig. 3.20a shows the strut cross-section of the original specimen, like that of the strut in Fig. 3.19. The surface of the fracture was relatively smooth, and a radial flow zone could still be observed outside the circular section. Under cyclic loading, the crack started from the outer surface defect and expanded inward in a fan-shaped radial ridge fringe, as shown in Fig. 3.20c. Finally, a dimple band formed near the inner hole defect to complete the fracture.

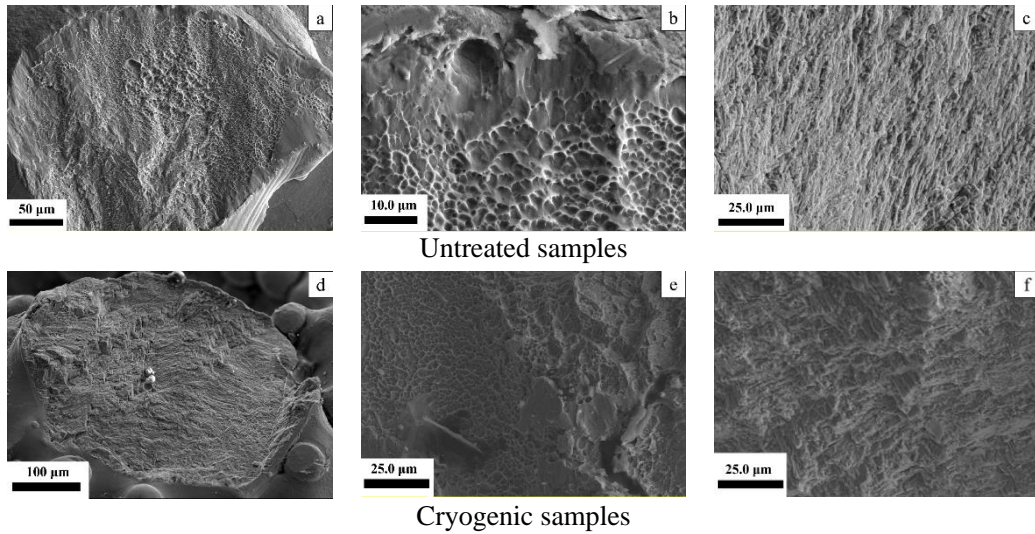


Fig. 3.20. The effect of cryogenic treatment on the fracture morphology on the overall fracture morphology a, d; the dimple morphology b, e; radial fringes of crack propagation c, f

Compared to the smooth section in the untreated state, the cliff height difference in the cross-section of the strut fracture after cryogenic treatment was noticeable, as shown in Fig. 3.20d. Unmelted metal particles are found inside the section, which can cause the generation of internal hole defects and devastate materials such as brittleness and ductile fracture. All struts have the same angle as the forming direction in the spatial local coordinate system. Excluding the deformation effect caused by the structural geometric model, the fracture of the samples after cryogenic treatment expands along the axial direction of the strut. Dimples of different sizes were formed on the high and low planes, as shown in Fig. 3.20e. The overall surface topography of the fracture depends on the distribution of pore nuclei and the sequence of pore nucleation and expansion. When a crack composed of connected pores begins to expand, a hydrostatic stress field is created in the material in front of the crack, causing new pores to nucleate and continue to expand. These new holes are linked to the main crack when the bridged molecular chain breaks. It is assumed that all the holes in the material are nucleated under the same stress and expand at the same rate shortly before the holes are connected. The material between the pores is in the shape of lamelliform, an irregular cross-section of a columnar structure. These reticular or columnar structures undergo plastic deformation and eventually separate to form an equiaxial dimple array on the two fracture surfaces. Some associated secondary micropores are found in larger columnar structures, so dimples of different sizes are distributed. As shown in Fig. 3.20f, after cryogenic treatment, the fracture morphology was hill-like in the radiating ridge fringes in the crack growth region, indicating that the random distribution of grain orien-

tation and decomposition of α -Ti phase clusters weakened the original texture. When fatigue failure occurred, under the synergistic action of the basal and prismatic slip system, the propagation selection of cracks increased and the axial fracture morphology of the strut appeared simultaneously.

The sliding of grain boundaries is an important creep mechanism for creep. Grain refinement increases the total area of the grain boundaries, which promotes the creep. Therefore, grain refinement does not always improve the deformation resistance of metals. The failure of the porous structures under periodic compression loads was dominated by the ratchet effect. The activation of more slip systems improves the plastic properties of metals and leads to the accumulation of larger deformations during fatigue failure. However, porous-structured products prepared by EBM technology are too precise and have high requirements for the application environment. Post-treatment is an effective method for eliminating the residual stress generated during solidification, and can prevent the defects in structural parts from cracking or spontaneous deformation. Meanwhile, the improvement of plasticity improvement makes the deformation behavior of bone implants less radical under the action of stress.

3.5 Summary

Due to the small size of the lattice structure design, a large number of unmelted metal particles adhere to the surface of the struts, and geometric rounding occurs due to the hanging effect during the melting process, resulting in overlapping texture lines on the surface. Issues related to printing accuracy and quality contribute to the roughness of the component surface.

The Ti6Al4V base material fabricated by EBM exhibited high strength but relatively poor ductility. The compressive strength, equivalent elastic modulus, and fatigue performance of the lattice structure all increase monotonically as the mapping ratio α decreases. The angular variation of the struts gradually transitions the deformation mode from bending-dominated to buckling-dominated. The ultimate fatigue failure of the structure primarily occurs through the collapse of shear bands along the 45° direction. In the untreated specimens, the aggregated struts on the surface detach from the body at a certain rate. Fatigue fractures exhibited typical brittle fracture morphology, with relatively smooth surfaces, and crack propagation often occurred radially on the fracture plane.

The microstructure of the alloy revealed elongated primary β -grains generated by solidifi-

cation gradients, which gradually decomposed into lamellar α -Ti as the main phase along with a small amount of blocky and strip-like β -Ti in a mixed pattern. Agglomerated α -Ti grains aligned parallel to each other, forming a strong texture.

Deep cryogenic treatment is considered the most reasonable approach among various post-processing methods. After undergoing deep cryogenic treatment, the base material exhibits an elastic modulus that differs from the untreated specimens by approximately 4.4%, while the hardness remains nearly at the same level. Although the yield strength of the material decreases by approximately 4.5%, the tensile strength remains almost unchanged, and the elongation at fracture increases by nearly 44.4%, significantly improving the material's ductility.

During the fatigue tests, detachment of the surface strut aggregates is more gradual. Under the same cyclic load, the deep cryogenic treated specimens exhibit slightly higher fatigue life than the untreated specimens, but they accumulate more deformation. This is because the refinement of grains leads to an increased number of grain boundaries, resulting in decreased creep resistance of the structure.

The volume contraction of the material leads to the absorption of the stable V element precipitates in the β -Ti phase by the α -Ti phase after cryogenic treatment, resulting in significant lattice distortion. Dislocation multiplication occurs within the grains and tends to align in the same direction. These substructures form numerous unstable sub-grains, causing the aggregation of α -Ti grains to disperse, resulting in grain deflection and weakening of the original texture. The initiation of slip systems on prismatic and basal planes provides more favorable options for dislocation motion, and the decreased flatness of fatigue fractures provides strong evidence of improved plasticity, accompanied by an enhancement in fatigue performance.

Chapter 4 Geometric modeling

4.1 Homogenization of rhombic dodecahedron

To analyze the deformation of the multi-cell structure, it is necessary to consider the elastic deformation mode of the individual cells in compression. Prior to analysis, a homogenization treatment is applied to the cells, and the struts and nodes are parameterized based on the geometric characteristics of the individual cell. It is also important to consider the changes in the cross-sections of the struts after mapping, which can easily be overlooked. Therefore, a combination of finite element analysis and numerical methods is used to describe the various geometric parameters of the cells.

Homogenization method of the rhombic dodecahedron lattice structure involves a process of transitioning from local reactions to a global perspective. As shown in Fig. 4.1, the homogenous structure of the cell, known as the homogenized body, is formed by the outer eight free nodal points of the cell, creating a square framework. The density of the homogenized block is determined based on the percentage of porosity in the cell relative to the volume of the corresponding bulk material. After arranging the cells in a periodic manner to form a cube in three dimensions, the definition of the homogenized block remains the same as the cube formed by the outer eight free nodal points of the multicellular structure.

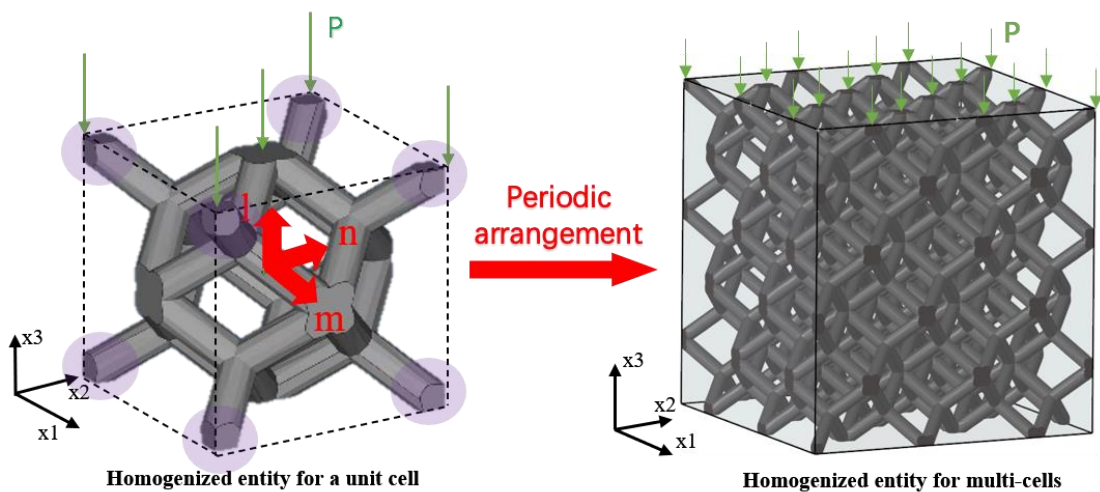


Fig. 4.1 Homogenization of the rhombic dodecahedron lattice structure

Here, it is assumed that the interior of the cube is homogeneous, and the specific material properties are determined by the deformation behavior of the struts. In particular, the stiffness

of the homogenized structure is influenced by the boundary effects of the outermost struts, which vary depending on the number of cells. The joints that experience force on the surface of the cells come into direct contact with the compression testing machine's platen. The resultant force at these joints represents the action force on the upper surface of the homogenized structure under compression loading. The equivalent stress at these joints satisfies the following equation:

$$\sigma_{eff} = \frac{P_c}{S_{area}} \quad (4-1A)$$

Where, σ_{eff} represents the equivalent stress, P_c represents the compression force on the upper surface, and S_{area} represents the rectangular area of the upper surface of the homogenized structure.

The stress in the compression-compression test is given by:

$$\Delta\sigma_0 = 2\Delta\sigma = \frac{P_{max} - P_{min}}{S_{area}} = \frac{P_{max}(1-R)}{S_{area}} \quad (4-1B)$$

As shown in Fig. 4.2, the axial strain in the compression direction of the cell structure with different mapping ratios is determined by the deformation relative to the height of the cell:

$$\mathcal{E}_{eff} = \frac{\Delta l}{b} \quad (4-2)$$

Where, \mathcal{E}_{eff} is the equivalent strain, Δl is the compression deformation of the cell, and b is the height of the cell's homogenous block.

The equivalent elastic modulus of the homogenous block is given by:

$$E_{eff} = \frac{\sigma_{eff}}{\mathcal{E}_{eff}} = \frac{P_c \cdot b}{S_{area} \cdot \Delta l} \quad (4-3)$$

The calculation of the equivalent elastic modulus assumes that the deformation of the homogenous block under compression occurs within the elastic range.

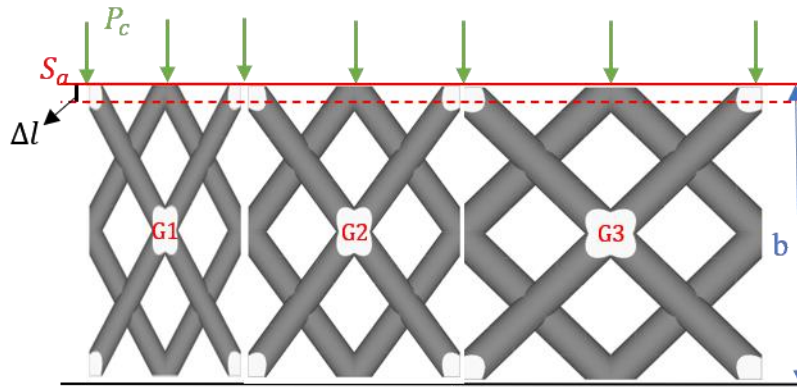


Fig. 4.2 Elastic deformation of the homogenized block under compression

4.2 Geometry of the unit cell

The mechanical properties of the cellular rhombic dodecahedron structure under compression in the vertical direction will be studied as shown in Fig. 4.3. Actual printed workpiece with a 5x5x5 cell configuration, as shown in Fig. 4.3a. The structure is based on the rhombic dodecahedron and supposed to be composed of $m \times n \times l$ identical cellular cells. As shown in Fig. 4.3b, one unit cell of the structure is a cubic space containing an entire rhombic dodecahedron of 24 struts and 8 struts connected to its neighbor cells in all the three directions. This is different from the structure whose unit cell volume contains entire rhombic dodecahedrons due to the range choice of rhombic dodecahedron's direction. As the number of layers l in the vertical direction does not influence the effective elastic modulus in this direction, l is supposed to be 1 without losing the generality. Therefore, the structure with $m \times n$ cells will be studied and the number of rows m and the columns n varies theoretically and mathematically from 1 to infinite. The effective elastic modulus of the structure in the vertical direction is a function of m and n . One unit cell gives the lower bound of the effective elastic modulus and a structure with infinite numbers of cells in row () or/and in column () gives the upper bounds for one direction (row or column) or the upper bound for two directions (row and column).

As shown in Fig. 4.3b, a unit cell based on the rhombic dodecahedron is composed of 32 cylinder struts with the diameter d and length L for each. This cell is framed by a cubic box with the edge length b .

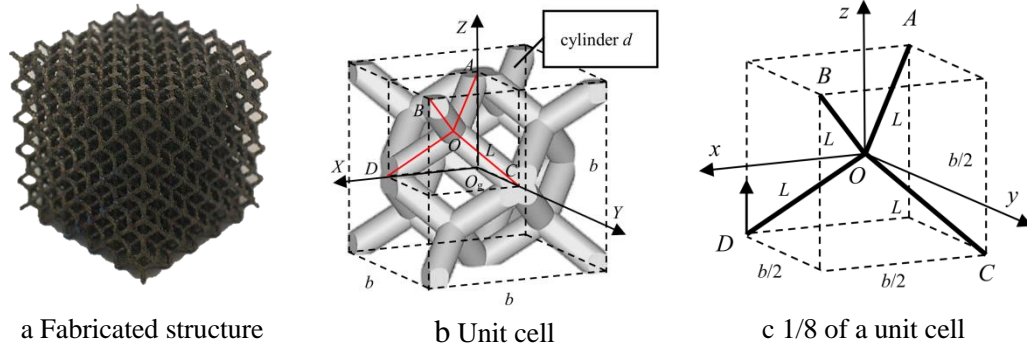


Fig. 4.3 Cell of rhombic dodecahedron structure

1/8 of a unit cell in a cubic box is taken for the analysis of the upper and lower bounds of the effective elastic modulus due to its triple symmetric geometry. The length of the beam L and the edge length of the box b holds:

$$L = \frac{\sqrt{3}}{4} b \quad (4-4)$$

As shown in Fig. 4.3b and 4.3c, the local coordinate system O - xyz shares the same directions of X -, Y - and Z -axis in the global coordinate system attached at the center of the cubic box point O_g . In the 1/8 of the unit cell shown in Fig. 4.3c, the coordinates of the nodes in the local coordinate system O - xyz are as follows:

$$A(-a, -a, a), B(a, a, a), C(-a, a, -a), D(a, -a, -a) \quad (4-5)$$

$$\text{with } a = L/\sqrt{3}.$$

And for each beam Oi ($i = A, B, C, D$), a local coordinate system attached to the origin point O is established and its directional vectors on the axes are designed as \vec{n}_i , \vec{t}_{i1} and \vec{t}_{i2} , respectively. The normal vector \vec{n}_i of the beam's section is given by:

$$\vec{n}_i = \text{norm}(\vec{O}i) \quad (4-6)$$

where the normalization function $\text{norm}()$ is defined as:

$$\text{norm}(\vec{u}) = \vec{u} / \|\vec{u}\|$$

By using Eqs. (4-5) and (4-6), a local coordinate system attached to the origin point O by its unit directional vectors \vec{n}_i , \vec{t}_{i1} , \vec{t}_{i2} as:

$$\begin{cases}
 \vec{n}_A = \frac{1}{\sqrt{3}} \begin{Bmatrix} -1 \\ -1 \\ 1 \end{Bmatrix}, \vec{n}_B = \frac{1}{\sqrt{3}} \begin{Bmatrix} 1 \\ 1 \\ 1 \end{Bmatrix}, \vec{n}_C = \frac{1}{\sqrt{3}} \begin{Bmatrix} -1 \\ 1 \\ -1 \end{Bmatrix}, \vec{n}_D = \frac{1}{\sqrt{3}} \begin{Bmatrix} 1 \\ -1 \\ -1 \end{Bmatrix} \\
 \vec{t}_{A1} = \frac{1}{\sqrt{6}} \begin{Bmatrix} -1 \\ -1 \\ -2 \end{Bmatrix}, \vec{t}_{B1} = \frac{1}{\sqrt{6}} \begin{Bmatrix} 1 \\ 1 \\ -2 \end{Bmatrix}, \vec{t}_{C1} = \frac{1}{\sqrt{6}} \begin{Bmatrix} 1 \\ -1 \\ -2 \end{Bmatrix}, \vec{t}_{D1} = \frac{1}{\sqrt{6}} \begin{Bmatrix} -1 \\ 1 \\ -2 \end{Bmatrix} \\
 \vec{t}_{A2} = \frac{1}{\sqrt{2}} \begin{Bmatrix} 1 \\ -1 \\ 0 \end{Bmatrix}, \vec{t}_{B2} = \frac{1}{\sqrt{2}} \begin{Bmatrix} -1 \\ 1 \\ 0 \end{Bmatrix}, \vec{t}_{C2} = \frac{1}{\sqrt{2}} \begin{Bmatrix} -1 \\ -1 \\ 0 \end{Bmatrix}, \vec{t}_{D2} = \frac{1}{\sqrt{2}} \begin{Bmatrix} 1 \\ 1 \\ 0 \end{Bmatrix}
 \end{cases} \quad (4-7)$$

The unit cell shown in Fig. 4.3 can be mapped in the X-direction with affine mapping: $x \rightarrow \alpha x$, where α is the mapping ratio as shown in Fig. 4.4.

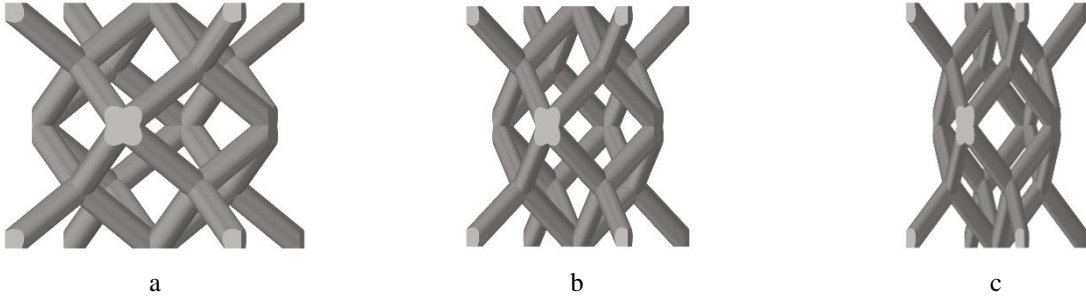


Fig. 4.4. Affine mapping of the unit cell in the X-direction: a unmapped cell ($\alpha = 1$), b mapped cell ($\alpha = 0.7$), c mapped cell ($\alpha = 0.5$)

The structure is mapped in x -direction with $x \rightarrow \alpha x$, α is called the mapping ratio. After the mapping in x -direction, a point i is denoted as i_α and the beam's direction is a function of the mapping ratio α :

$$\vec{n}_{A\alpha} = \frac{1}{\sqrt{\alpha^2 + 2}} \begin{Bmatrix} -\alpha \\ -1 \\ 1 \end{Bmatrix}, \vec{n}_{B\alpha} = \frac{1}{\sqrt{\alpha^2 + 2}} \begin{Bmatrix} \alpha \\ 1 \\ 1 \end{Bmatrix}, \vec{n}_{C\alpha} = \frac{1}{\sqrt{\alpha^2 + 2}} \begin{Bmatrix} -\alpha \\ 1 \\ -1 \end{Bmatrix}, \vec{n}_{D\alpha} = \frac{1}{\sqrt{\alpha^2 + 2}} \begin{Bmatrix} \alpha \\ -1 \\ -1 \end{Bmatrix} \quad (4-8)$$

And the length of a mapped strut (beam) is a function of α :

$$L_\alpha = \frac{\sqrt{\alpha^2 + 2}}{\sqrt{3}} L \quad (4-9)$$

4.3 Mathematic description of the beam's section

For the beginning, the beam OA is taken as an example to demonstrate the geometrical relations. After the mapping in x -direction, the beam's direction is a function of the mapping ratio

α . The form of the section that is perpendicular to $\vec{n}_{A\alpha}$ is an ellipse. The projection of this ellipse on the plane yoz is also an ellipse. These two ellipses share the same long axe (when $\alpha \leq 1$): the direction and the length are the same.

The long-axis direction of the ellipse, which is a horizontal projection on the plane YOZ is as follows:

$$\vec{\Delta}_1 = \begin{Bmatrix} 0 \\ \cos t \\ \sin t \end{Bmatrix} \quad (4-10)$$

As $\vec{\Delta}_1$ and \vec{n}_A are perpendicular to each other:

$$\vec{\Delta}_1 \cdot \vec{n}_A = 0 \quad (4-11)$$

By using Eqs. (4-10) and (4-11), the components of $\vec{\Delta}_1$ can be found as follows:

$$\begin{cases} \cos t = \frac{-n_{Az}}{\sqrt{n_{Ay}^2 + n_{Az}^2}} \\ \sin t = \frac{n_{Ay}}{\sqrt{n_{Ay}^2 + n_{Az}^2}} \end{cases} \text{ or } \begin{cases} \cos t = \frac{n_{Az}}{\sqrt{n_{Ay}^2 + n_{Az}^2}} \\ \sin t = \frac{-n_{Ay}}{\sqrt{n_{Ay}^2 + n_{Az}^2}} \end{cases} \quad (4-12)$$

The first vector in Eq. (4-12) is chosen as $\vec{\Delta}_1$, which is the direction of the long half-axis of the ellipse. Using the value of \vec{n}_A , $\vec{\Delta}_1$ is numerically expressed as:

$$\vec{\Delta}_1 = \frac{1}{\sqrt{2}} \begin{Bmatrix} 0 \\ -1 \\ -1 \end{Bmatrix} \quad (4-13)$$

As the calculation may between the strut before and after mapping, two local coordinate systems are needed.

1) Local coordinate system of beam OA before mapping

The base of this local coordinate system of beam OA is chosen as $[\vec{n}_A \vec{\Delta}_1 \vec{\Delta}_2]$ in which

$$\vec{\Delta}_2 = \vec{n}_A \times \vec{\Delta}_1 = \frac{1}{\sqrt{3}} \begin{Bmatrix} -1 \\ -1 \\ 1 \end{Bmatrix} \times \frac{1}{\sqrt{2}} \begin{Bmatrix} 0 \\ -1 \\ -1 \end{Bmatrix} = \frac{1}{\sqrt{6}} \begin{Bmatrix} 2 \\ -1 \\ 1 \end{Bmatrix} \quad (4-14)$$

2) Local coordinate system of beam OA_α after mapping from OA

The long axe direction is used as the first coordinate direction for the local coordinate system in the mapped beam. A local coordinates system for the mapped beam OA is established by

using the base $[\vec{n}_{A\alpha} \vec{t}_{A\alpha_1} \vec{t}_{A\alpha_2}]$, in which:

$$\vec{t}_{A\alpha_1} = \vec{\Delta}_1 = \frac{1}{\sqrt{2}} \begin{Bmatrix} 0 \\ -1 \\ -1 \end{Bmatrix} \quad (4-15)$$

$$\vec{t}_{A\alpha_2} = \vec{n}_{A\alpha} \times \vec{t}_{A\alpha_1} = \frac{1}{\sqrt{\alpha^2 + 2}} \begin{Bmatrix} -\alpha \\ -1 \\ 1 \end{Bmatrix} \times \frac{1}{\sqrt{2}} \begin{Bmatrix} 0 \\ -1 \\ -1 \end{Bmatrix} = \frac{1}{\sqrt{2\alpha^2 + 4}} \begin{Bmatrix} 2 \\ -\alpha \\ \alpha \end{Bmatrix} \quad (4-16)$$

And the base is expressed as follows by using Eqs. (4-8), (4-15) and (4-16):

$$[\vec{n}_{A\alpha} \vec{t}_{A\alpha_1} \vec{t}_{A\alpha_2}] = \begin{bmatrix} \frac{-\alpha}{\sqrt{\alpha^2 + 2}} & 0 & \frac{2}{\sqrt{2\alpha^2 + 4}} \\ \frac{-1}{\sqrt{\alpha^2 + 2}} & \frac{-1}{\sqrt{2}} & \frac{-\alpha}{\sqrt{2\alpha^2 + 4}} \\ \frac{1}{\sqrt{\alpha^2 + 2}} & \frac{-1}{\sqrt{2}} & \frac{\alpha}{\sqrt{2\alpha^2 + 4}} \end{bmatrix} \quad (4-17)$$

In the initial non-mapped unit, a radius vector holds on the section of radius r :

$$\overline{AP} = [\vec{n}_A \vec{\Delta}_1 \vec{\Delta}_2] \begin{Bmatrix} 0 \\ r \cos \theta \\ r \sin \theta \end{Bmatrix} = \begin{bmatrix} \frac{-1}{\sqrt{3}} & 0 & \frac{2}{\sqrt{6}} \\ \frac{-1}{\sqrt{3}} & \frac{-1}{\sqrt{2}} & \frac{-1}{\sqrt{6}} \\ \frac{1}{\sqrt{3}} & \frac{-1}{\sqrt{2}} & \frac{1}{\sqrt{6}} \end{bmatrix} \begin{Bmatrix} 0 \\ r \cos \theta \\ r \sin \theta \end{Bmatrix} = \frac{r}{\sqrt{2}} \begin{Bmatrix} \frac{2}{\sqrt{3}} \sin \theta \\ -\cos \theta - \frac{1}{\sqrt{3}} \sin \theta \\ -\cos \theta + \frac{1}{\sqrt{3}} \sin \theta \end{Bmatrix} \quad (4-18)$$

As the structure is mapped in x -direction with $x \rightarrow \alpha x$, it is supposed that in mapped structure, $\overline{A_\alpha P'}$ is obtained by the mapping from \overline{AP} , therefore,

$$\overline{A_\alpha P'} = \begin{Bmatrix} \frac{2\alpha}{\sqrt{3}} \sin \theta \\ -\cos \theta - \frac{1}{\sqrt{3}} \sin \theta \\ -\cos \theta + \frac{1}{\sqrt{3}} \sin \theta \end{Bmatrix} \quad (4-19)$$

And then using the base of the local coordinate system of the mapped beam OA_α in Eq. (4-17A), $\overline{A_\alpha P'}$ can expressed as follows:

$$\begin{aligned}
 \overline{AP'} &= [\vec{n}_{A\alpha} \vec{t}_{A\alpha 1} \vec{t}_{A\alpha 2}] [\vec{n}_{A\alpha} \vec{t}_{A\alpha 1} \vec{t}_{A\alpha 2}]^T \overline{AP'} \\
 &= [\vec{n}_{A\alpha} \vec{t}_{A\alpha 1} \vec{t}_{A\alpha 2}] \begin{bmatrix} \frac{-\alpha}{\sqrt{\alpha^2+2}} & 0 & \frac{2}{\sqrt{2\alpha^2+4}} \\ \frac{-1}{\sqrt{\alpha^2+2}} & \frac{-1}{\sqrt{2}} & \frac{-\alpha}{\sqrt{2\alpha^2+4}} \\ \frac{1}{\sqrt{\alpha^2+2}} & \frac{-1}{\sqrt{2}} & \frac{\alpha}{\sqrt{2\alpha^2+4}} \end{bmatrix}^T \frac{r}{\sqrt{2}} \begin{Bmatrix} \frac{2\alpha}{\sqrt{3}} \sin \theta \\ -\cos \theta - \frac{1}{\sqrt{3}} \sin \theta \\ -\cos \theta + \frac{1}{\sqrt{3}} \sin \theta \end{Bmatrix} \\
 &= [\vec{n}_{A\alpha} \vec{t}_{A\alpha 1} \vec{t}_{A\alpha 2}] r \begin{Bmatrix} \frac{\sqrt{2}(-\alpha^2+1)}{\sqrt{3}\sqrt{\alpha^2+2}} \sin \theta \\ \cos \theta \\ \frac{\sqrt{3}\alpha}{\sqrt{\alpha^2+2}} \sin \theta \end{Bmatrix}
 \end{aligned} \tag{4-20}$$

The vector $\overline{A_\alpha P''}$ is the projection of $\overline{A_\alpha P'}$ on the section that is perpendicular to $\vec{n}_{A\alpha}$, it can be obtained directly from $\overline{AP'}$ by imposing $x=0$ in the local coordinate system:

$$\overline{A_\alpha P''} = [\vec{n}_{A\alpha} \vec{t}_{A\alpha 1} \vec{t}_{A\alpha 2}] r \begin{Bmatrix} 0 \\ \cos \theta \\ \frac{\sqrt{3}\alpha}{\sqrt{\alpha^2+2}} \sin \theta \end{Bmatrix} \tag{4-21}$$

$\overline{A_\alpha P''}$ shows that the section is an ellipse, whose half-axe lengths are r and $\frac{\sqrt{3}\alpha}{\sqrt{\alpha^2+2}} r$ respectively.

Compared to the enormous solid element computational cost of the solid element, the beam element significantly improves the computational efficiency within a controllable accuracy range. However, the expression of the strut section expression after mapping determines the accuracy of the calculation. The change in the base vector of the strut section are shown in in Fig. 4.5.

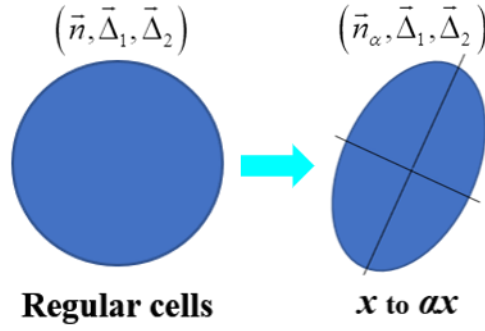


Fig. 4.5 Change of strut section with mapping

Fig. 4.6a shows the geometric comparison between the defined rear strut section and the regular cylindrical strut section for α values of 0.7 and 0.5, respectively. For such a precise structures, small differences can result in lead to wildly very different predictions. The change from a circle to an ellipse provides a complete deviation from the actual geometric parameters: the normal of the elliptical cross-section, the angle of the strut, and the section size are not the same after the mapping transformation. Therefore, the parameterization of the cross-section is essential to obtain the actual cross-section parameters of the elliptical strut, such as the moment of inertia. The expression of strut-section attributes are expressed as follows:

For an ellipse $\begin{cases} y = p\rho \cos \theta \\ z = q\rho \sin \theta \end{cases}$, and the quadratic moments of an ellipse are given by the following equations:

$$I_y = \iint z^2 dydz = 4 \int_{\theta=0}^{\theta=\frac{\pi}{2}} \int_{\rho=0}^{\rho=1} q^2 \rho^2 \sin^2 \theta pq \rho d\rho d\theta = \frac{\pi}{4} pq^3 \quad (4-22A)$$

$$I_z = \iint y^2 dydz = 4 \int_{\theta=0}^{\theta=\frac{\pi}{2}} \int_{\rho=0}^{\rho=1} p^2 \rho^2 \cos^2 \theta pq \rho d\rho d\theta = \frac{\pi}{4} p^3 q \quad (4-22B)$$

The moment of inertia is then obtained as follows:

$$I_o = I_y + I_z = \frac{\pi}{4} pq(p^2 q + pq^2) \quad (4-22C)$$

And

$$I_{yz} = \iint yz dydz = \int_{\theta=0}^{\theta=2\pi} \int_{\rho=0}^{\rho=1} \rho^2 \sin \theta \cos \theta pq \rho d\rho d\theta = 0$$

Using $p = r$; $q = \frac{\sqrt{3}\alpha}{\sqrt{\alpha^2 + 2}} r$, the above moments with respect to the two half-axes are expressed as follow:

$$I_{yA\alpha} = I_{A\alpha 1} = \frac{3\sqrt{3}\pi}{4} \frac{\alpha^3}{(\alpha^2 + 2)\sqrt{\alpha^2 + 2}} r^4 \quad (4-23A)$$

$$I_{zA\alpha} = I_{A\alpha 2} = \frac{\sqrt{3}\pi}{4} \frac{\alpha}{\sqrt{\alpha^2 + 2}} r^4 \quad (4-23B)$$

$$I_{OA\alpha} = I_{A\alpha 1} + I_{A\alpha 2} = \frac{\sqrt{3}\pi}{2} \frac{(2\alpha^2 + 1)\alpha}{(\alpha^2 + 2)\sqrt{\alpha^2 + 2}} r^4 \quad (4-24C)$$

The surface of this section of ellipse form is:

$$S = \pi pq = \pi \frac{\sqrt{3}\alpha}{\sqrt{\alpha^2 + 2}} r^2 \quad (4-25)$$

By using the same method for the other struts,

$$\vec{t}_{B\alpha 1} = \frac{1}{\sqrt{2}} \begin{Bmatrix} 0 \\ -1 \\ 1 \end{Bmatrix}; \vec{t}_{C\alpha 1} = \frac{1}{\sqrt{2}} \begin{Bmatrix} 0 \\ 1 \\ 1 \end{Bmatrix}; \vec{t}_{D\alpha 1} = \frac{1}{\sqrt{2}} \begin{Bmatrix} 0 \\ 1 \\ -1 \end{Bmatrix} \quad (4-26A)$$

$$\vec{t}_{B\alpha 2} = \frac{1}{\sqrt{2\alpha^2 + 4}} \begin{Bmatrix} 2 \\ -\alpha \\ -\alpha \end{Bmatrix}; \vec{t}_{C\alpha 2} = \frac{1}{\sqrt{2\alpha^2 + 4}} \begin{Bmatrix} 2 \\ \alpha \\ -\alpha \end{Bmatrix}; \vec{t}_{D\alpha 2} = \frac{1}{\sqrt{2\alpha^2 + 4}} \begin{Bmatrix} 2 \\ \alpha \\ \alpha \end{Bmatrix} \quad (4-26B)$$

And the bases of their local coordinate system are expressed as follow:

$$[\vec{n}_{B\alpha} \vec{t}_{B\alpha 1} \vec{t}_{B\alpha 2}] = \begin{bmatrix} \frac{\alpha}{\sqrt{\alpha^2 + 2}} & 0 & \frac{2}{\sqrt{2\alpha^2 + 4}} \\ \frac{1}{\sqrt{\alpha^2 + 2}} & \frac{-1}{\sqrt{2}} & \frac{-\alpha}{\sqrt{2\alpha^2 + 4}} \\ \frac{1}{\sqrt{\alpha^2 + 2}} & \frac{1}{\sqrt{2}} & \frac{-\alpha}{\sqrt{2\alpha^2 + 4}} \end{bmatrix} \quad (4-27A)$$

$$[\vec{n}_{C\alpha} \vec{t}_{C\alpha 1} \vec{t}_{C\alpha 2}] = \begin{bmatrix} \frac{-\alpha}{\sqrt{\alpha^2 + 2}} & 0 & \frac{2}{\sqrt{2\alpha^2 + 4}} \\ \frac{1}{\sqrt{\alpha^2 + 2}} & \frac{1}{\sqrt{2}} & \frac{\alpha}{\sqrt{2\alpha^2 + 4}} \\ \frac{-1}{\sqrt{\alpha^2 + 2}} & \frac{1}{\sqrt{2}} & \frac{-\alpha}{\sqrt{2\alpha^2 + 4}} \end{bmatrix} \quad (4-27B)$$

$$[\vec{n}_{D\alpha} \vec{t}_{D\alpha 1} \vec{t}_{D\alpha 2}] = \begin{bmatrix} \frac{\alpha}{\sqrt{\alpha^2 + 2}} & 0 & \frac{2}{\sqrt{2\alpha^2 + 4}} \\ \frac{-1}{\sqrt{\alpha^2 + 2}} & \frac{1}{\sqrt{2}} & \frac{\alpha}{\sqrt{2\alpha^2 + 4}} \\ \frac{-1}{\sqrt{\alpha^2 + 2}} & \frac{-1}{\sqrt{2}} & \frac{\alpha}{\sqrt{2\alpha^2 + 4}} \end{bmatrix} \quad (4-27C)$$

And the quadratic moments are formulated as:

$$I_{yB\alpha} = I_{yC\alpha} = I_{yD\alpha} = I_{yA\alpha} = I_y \quad (4-28A)$$

$$I_{zB\alpha} = I_{zC\alpha} = I_{zD\alpha} = I_{zA\alpha} = I_z \quad (4-28B)$$

and

$$I_{OB\alpha} = I_{OC\alpha} = I_{OD\alpha} = I_{OA\alpha} = I_O \quad (4-28C)$$

A comparison between the elliptical beam and the cylinder after the single cell mapping is shown in Fig. 4(a), where $\alpha=0.7$ is shown in blue and $\alpha=0.5$ is shown in brown. The section inertia after the assignment of Eq. (9) is displayed by the beam element (Fig. 4(b)), which is completely consistent with that of the solid element (Fig. 4(c)), thus verifying the correctness and feasibility of the section attribute.

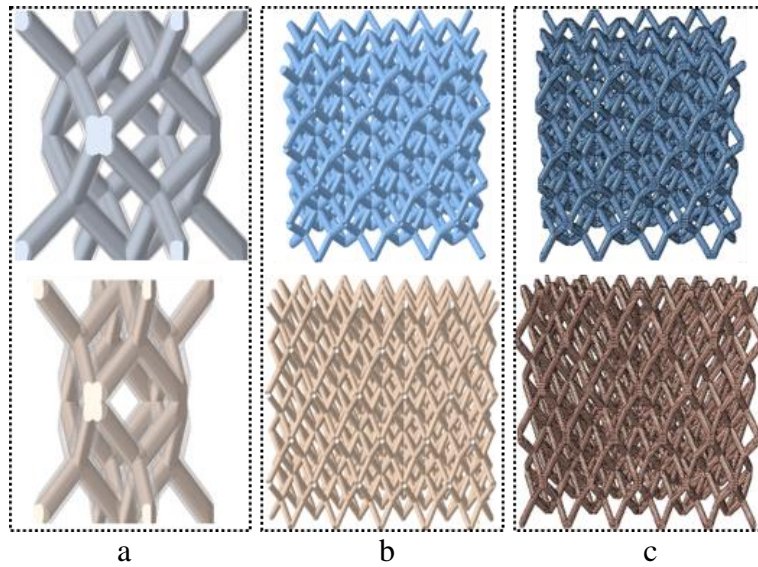


Fig. 4.6 The geometric difference between circular and elliptic section a; the consistency of the elliptic section strut with beam element b; solid element c

For the structure mapped or not mapped in the X -direction, two different cases of application conditions of the rhombic dodecahedron structure under compression will be studied: 1)

without border constraint in the the X-direction and the Y-direction; 2) with border constraint in the the X-direction and the Y-direction.

The analytical method and finite element (FE) method both based on beam theory will be used to predict the effective modulus: each strut is considered as a beam. As the analytical and the FE methods are based on the same theory, these two methods will give the same results. Therefore, the analytical method is only chosen to calculate the bounds without constraint and the case with border constraint that doesn't need much manual calculation. That is, the analytical method will be used to calculate the lower bound ($m=n=1$) and upper bound for two directions () of the effective elastic modulus for case 1) and the bulking elastic strength for case 2); the FE method will be used to calculate any value of m and n for case 1) due to its calculation capacity that can establish the graphic of the effective elastic modulus related to m and n . For the upper bound due to the infinite number of rows or/and columns, special boundary conditions will be applied with the minimum number of cells in both analytical and the FE methods.

4.4 Summary

In this chapter, the cell consisting of struts is equivalently represented as a square frame formed by the outermost free struts. The vector equations for the struts and nodes in the local coordinate system are established for a single cell. The mapping ratio α is introduced in the equations to describe the parametric equations of the cell after mapping along the X-axis. The variation of the cross-section of the beam after mapping has a significant influence on the deformation accuracy. The parameter equations for an elliptical cross-section are established in polar coordinates. By projecting the cross-section onto the coordinate plane after mapping, the cross-section properties are effectively expressed. The accuracy of the parameter equations is validated through numerical simulations and visualizations.

Chapter 5 The analytical calculation of the equivalent elastic modulus

The elastic modulus is one of the most important properties that affect the compressive performance of lattice structures, especially for applications involving biomedical implants. Lattice structures can be broadly classified into two categories: closed-cell and open-cell. Closed-cell lattice structures can provide higher strength, making them suitable for applications with high strength requirements. On the other hand, open-cell lattice structures are more suitable for applications where energy absorption or high biocompatibility with human tissues is desired, such as in biomedical implants. Therefore, it is essential to predict and calculate the elastic modulus of the diamond cubic lattice structure based on different working conditions.

5.1 Application conditions of the structure under compression

Two cases of application conditions of the structure under compression exist: the borders of the structure are under constraint in the X -direction or/and the Y -direction or not. When the borders are only under constraint in one direction (X - or Y -direction), the effective elastic modulus increases considerably with respect to that without constraint.

Fig. 5.1 in the paper illustrates the schematic diagrams of these two different structures. As shown in Fig. 5.1a, when the lattice structure is subjected to compressive load, the struts undergo bending, causing a decrease in the overall height of the structure along the Z -axis. The lattice structure expands freely in the $XOgY$ plane, deforming in all directions. On the other hand, Fig. 5.1b represents a fully constrained boundary condition. Under the same compressive conditions, the lattice structure is fully constrained on all sides, and there is no sliding deformation in the X and Y directions. The volume of the lattice structure is compressed completely. These deformation modes represent the compressive behavior of open-cell and closed-cell lattice structures, respectively. The discussion will further analyze the effects of different constraint conditions.

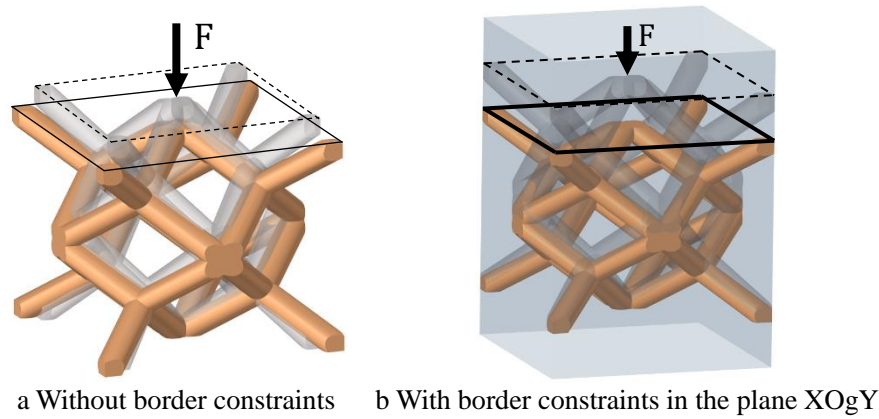


Fig. 5.1 The two different compression boundary conditions of the cell structure

5.1.1 Application without border constraint in the plane XO_gY

If the structure has no border constraint in the plane XO_gY , all borders are free and the effective elastic modulus can be calculated related to the number of rows m and that of columns n . The effective elastic modulus of the structure may be solved by beam theory without considering the shear efforts by using the FE method as a preference due to its strong calculation capacity. When m or/and n tend to infinite, the elastic behaviors of the cells become periodic, with non-zero horizontal displacement in the constrained direction on the borders of each cell, and special boundary conditions will be applied to the structure by using the minimum number of cells.

Particularly, the analytical method may be also used due to its simplicity in the analysis of the structure with one single unit cell without constraint in the plane XO_gY .

5.1.2 Application with border constraint in the plane XO_gY

For a structure under compression in the vertical direction, when the borders of the structure are constrained by two rigid panels, in the X-direction for example (left and right), the structure is periodic in the X-direction. In this case $m \times n$ cells (Fig. 5.2a) and $m \times 1$ cells (Fig. 5.2b) have the same elastic behavior, therefore one border-constrained structure of $m \times 1$ cells can present the border-constrained structure of $m \times n$ cells with any value of n . Different from the periodicity of the precedent case without constraint, the displacement in the constrained direction on the borders of each unit cell is zero.

If the structure is constrained in the Y-direction at the same time, 1×1 cell has the same effective elastic modulus in the vertical direction as that of $m \times n$ cells with any value of m and n .

The FE method is a preferential tool to calculate the effective elastic modulus for the struc-

ture with border constraint, but the effective elastic modulus in this case will be calculated by the analytical method too. Because the analytical method gives an explicit expression that allows a better understanding of the effective elastic modulus.

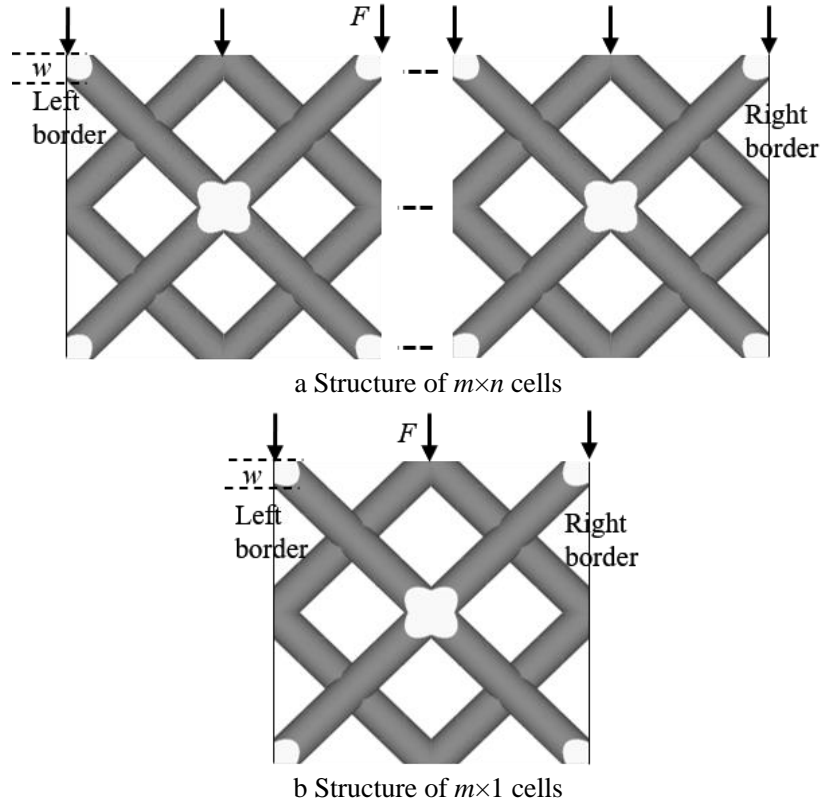


Fig. 5.2 Presentation of structure under compression

In order to simplify the expressions, the notions for the points i_α ($i=A, B, C$ or D) in the mapped unit will be presented as i in this section.

5.1.3 Lower and upper bounds of effective elastic modulus by using analytical method

Due to the triple symmetry of the structure, $1/8$ of the unit cell is taken to calculate the lower and upper bounds of the effective elastic modulus in the Z -direction by using the beam theory in taking into consideration the tension, bending and torsion but neglecting the shearing effect with proper boundary conditions. A unit cell under vertical compression with free borders gives the lower bound of the effective elastic modulus in the Z -direction, in which $m=n=1$ as shown in Fig. 5.3a and the case $m \rightarrow \infty$ and $n \rightarrow \infty$ gives the upper bound as shown in Fig. 5.3b.

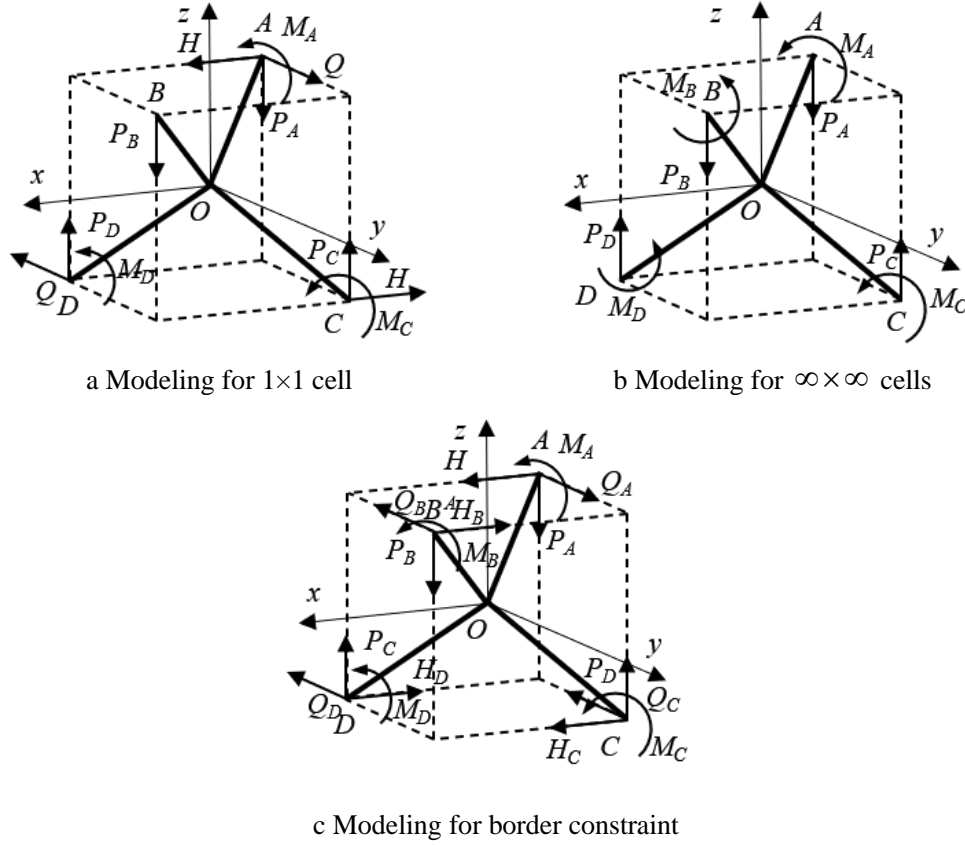


Fig. 5.3 Boundary conditions on the $1/8^{\text{th}}$ unit cell: a: 1×1 cell, b: $\infty \times \infty$ cells, c: $m \times n$ cells with border constraints.

In both cases with free borders and the case with border constraint, the equilibrium of forces holds:

$$\sum \vec{F}_{\text{ext}} = \vec{P}_A + \vec{P}_B + \vec{P}_C + \vec{P}_D = \vec{0} \quad (5-1)$$

and the balance of moments at point O is written as:

$$\sum \vec{M}_{/O} = \vec{M}_A + \vec{M}_B + \vec{M}_C + \vec{M}_D + L_\alpha \vec{n}_{A\alpha} \times \vec{P}_A + L_\alpha \vec{n}_{B\alpha} \times \vec{P}_B + L_\alpha \vec{n}_{C\alpha} \times \vec{P}_C + L_\alpha \vec{n}_{D\alpha} \times \vec{P}_D = \vec{0} \quad (5-2)$$

5.2 Analytical model for lower bound of effective elastic modulus

$1/8$ of the unit cell is taken in study and the global displacements U, V, W, θ are taken as unknown variables. In the global coordinate system, by considering the triple geometrical symmetry plane and the imposed displacement W in the Z -direction at the points A and B , the constant displacement boundary conditions hold:

$$\begin{cases} \text{Point A: } U_A = V_A = 0; W_A = W; \theta_{Ax} = \theta_{Ay} = \theta_{Az} = 0 \\ \text{Point B: } W_B = W \\ \text{Point C: } U_C = W_C = 0; \theta_{Cx} = \theta_{Cy} = \theta_{Cz} = 0 \\ \text{Point D: } V_D = W_D = 0; \theta_{Dx} = \theta_{Dy} = \theta_{Dz} = 0 \end{cases} \quad (5-3)$$

The displacement \vec{u}_{Oi} and rotation $\vec{\theta}_{Oi}$ of a point i ($i=A, B, C, D$) with respect to point O is given by:

$$\begin{cases} \vec{U}_i = \vec{U}_O + \vec{u}_{Oi} \\ \vec{\theta}_i = \vec{\theta}_O + \vec{\theta}_{Oi} \end{cases} \quad (5-4)$$

The relative displacement or rotation between two points will be used to define the displacement boundary conditions instead of the absolute ones given in Eq. (5-3) as follows:

$$\begin{cases} W_A = W_B \\ W_C = W_D \\ W_A - W_D = W \\ U_A = U_C \\ V_A = V_D \end{cases} \quad (5-5)$$

The rotation boundary conditions $\vec{\theta}_A = \vec{\theta}_C = \vec{\theta}_D = \vec{0}$ are used in the equations of displacement-moment of the concerned beams. As the four beams Oi share the same origin point O and the connection between any two beams is a rigid-rigid connection, therefore the supplementary boundary conditions for four beams at point O are given as follows:

$$\begin{cases} \vec{\theta}_{OA}(0) = \vec{\theta}_{OC}(0) \\ \vec{\theta}_{OA}(0) = \vec{\theta}_{OD}(0) \\ \vec{\theta}_{OA}(0) = \vec{\theta}_{OB}(0) \end{cases} \quad (5-6)$$

Particularly, as beam OB is free in torsion, only the rotation due to bending will be considered in Eq. (5-6).

By considering the double symmetry of the unit cell on the plane XOgY and the equilibrium given in Eq. (5-1), the forces on the 1/8th unit cell are supposed to be as shown in Fig. 5.3a, thus:

$$\vec{P}_A = \begin{Bmatrix} H_A = H \\ Q_A = Q \\ -P_A \end{Bmatrix}, \quad \vec{P}_B = -P_B \vec{k} \quad (5-7)$$

As in a symmetric plane of a border-free problem, the sum of the normal force is zero, by

using two symmetric planes ZOgX and YOgZ, \vec{P}_C in the X-direction and \vec{P}_D in the Y-direction are function of \vec{P}_A as:

$$\vec{P}_C = \begin{Bmatrix} -H_A \\ 0 \\ P_C \end{Bmatrix}, \quad \vec{P}_D = \begin{Bmatrix} 0 \\ -Q_A \\ P_D \end{Bmatrix} \quad (5-8)$$

The exterior moments on the boundary nodes are given by:

$$\vec{M}_A = \begin{Bmatrix} M_{Ax} \\ M_{Ay} \\ M_{Az} \end{Bmatrix}, \quad \vec{M}_B = \vec{0}, \quad \vec{M}_C = \begin{Bmatrix} M_{Cx} \\ M_{Cy} \\ M_{Cz} \end{Bmatrix}, \quad \vec{M}_D = \begin{Bmatrix} M_{Dx} \\ M_{Dy} \\ M_{Dz} \end{Bmatrix} \quad (5-9)$$

In the non-zero components of forces and moments listed in Eqs. (5-7), (5-8) and (5-9) there are in 15 unknown variables. As point B is free in bending, beam OB has only two boundary conditions in bending leading to two extra unknown variables. In the following, we develop the equations to determine the 17 unknown variables of the problem.

By using Eq. (5-7) and (5-8) in Eq. (5-1), the latter is reduced in the Z-direction as:

$$-P_A - P_B + P_C + P_D = 0 \quad (5-10)$$

By using Eqs. (4-27), (5-7), (5-8) and (5-9) in Eq. (5-2), the latter is simplified as follows:

$$\begin{Bmatrix} M_{Ax} + M_{Cx} + M_{Dx} \\ M_{Ay} + M_{Cy} + M_{Dy} \\ M_{Az} + M_{Cz} + M_{Dz} \end{Bmatrix} + \begin{Bmatrix} P_A - P_B + P_C - P_D - 2Q_A \\ \alpha(-P_A + P_B + P_C - P_D) + 2H_A \\ -2\alpha Q_A + 2H_A \end{Bmatrix} \frac{L_\alpha}{\sqrt{\alpha^2 + 2}} = \vec{0} \quad (5-11)$$

The normal force in the section of the beams is formulated as follows:

$$N_i = \vec{P}_i \cdot \vec{n}_{i\alpha} \quad (5-12)$$

The normal force to the section of each beam is defined as follows:

$$N_A = \vec{P}_A \cdot \vec{n}_{A\alpha} = \frac{-P_A - \alpha H_A - Q_A}{\sqrt{\alpha^2 + 2}} \quad (5-13)$$

$$N_B = \vec{P}_B \cdot \vec{n}_{B\alpha} = \frac{-P_B}{\sqrt{\alpha^2 + 2}} \quad (5-14)$$

$$N_C = \vec{P}_{CA} \cdot \vec{n}_{C\alpha} = \frac{1}{\sqrt{\alpha^2 + 2}} (-P_C + \alpha H_A) \quad (5-15)$$

$$N_D = \vec{P}_D \cdot \vec{n}_{D\alpha} = \frac{1}{\sqrt{\alpha^2 + 2}} (-P_D + Q_A) \quad (5-16)$$

By taking into consideration the moments, all the four beams have the same formulation for the moments, and beams OA, OC and OD have the same formulation for the boundary conditions. Therefore, the moments can be formulated by Oi (i=A, C and D) and OB will be treated independently by using different boundary conditions.

The moment in a section with distance s from point O in a beam Oi can be written as follows:

$$\vec{M}_{Oi}(s) = \vec{M}_i + (L_\alpha - s)\vec{n}_{i\alpha} \times \vec{P}_i = \begin{bmatrix} \vec{n}_{i\alpha} & \vec{t}_{i\alpha 1} & \vec{t}_{i\alpha 2} \end{bmatrix} \begin{Bmatrix} M_{ixl0} \\ M_{iy l0} + M_{iy l1}(s - L_\alpha) \\ M_{iz l0} + M_{iz l1}(s - L_\alpha) \end{Bmatrix} \quad (5-17)$$

By using Eqs. (4-27), (5-7), (5-8) and (5-9) in Eq. (5-17), the moment components for Oi are determined in the beam local coordinate system l as follows:

$$\begin{cases} M_{Axl0} = -\frac{1}{\sqrt{\alpha^2 + 2}}(\alpha M_{Ax} + M_{Ay} - M_{Az}) \\ M_{Ayl0} = -\frac{\sqrt{2}}{2}(M_{Ay} + M_{Az}); M_{Ayl1} = \frac{1}{\sqrt{2\alpha^2 + 4}}(-\alpha P_A + 2H_A - \alpha Q_A) \\ M_{Azl0} = \frac{1}{\sqrt{2\alpha^2 + 4}}(2M_{Ax} - \alpha M_{Ay} + \alpha M_{Az}); M_{Azl1} = \frac{\sqrt{2}}{2}(-P_A + Q_A) \end{cases} \quad (5-18)$$

$$\begin{cases} M_{Bxl0} = 0 \\ M_{Byl0} = 0; M_{Byl1} = \frac{\alpha}{\sqrt{2\alpha^2 + 4}}P_B \\ M_{Bzl0} = 0; M_{Bzl1} = \frac{1}{\sqrt{2}}P_B \end{cases} \quad (5-19)$$

$$\begin{cases} M_{Cxl0} = \frac{1}{\sqrt{\alpha^2 + 2}}(-\alpha M_{Cx} + M_{Cy} - M_{Cz}) \\ M_{Cyl0} = \frac{\sqrt{2}}{2}(M_{Cy} + M_{Cz}); M_{Cyl1} = -\frac{1}{\sqrt{2\alpha^2 + 4}}(2H_A + \alpha P_C) \\ M_{Czl0} = \frac{1}{\sqrt{2\alpha^2 + 4}}(2M_{Cx} + \alpha M_{Cy} - \alpha M_{Cz}); M_{Czl1} = -\frac{\sqrt{2}}{2}P_C \end{cases} \quad (5-20)$$

$$\begin{cases} M_{Dxl0} = \frac{1}{\sqrt{\alpha^2 + 2}} (\alpha M_{Dx} - M_{Dy} - M_{Dz}) \\ M_{Dyl0} = \frac{\sqrt{2}}{2} (M_{Dy} - M_{Dz}); M_{Dyl1} = \frac{\alpha}{\sqrt{2\alpha^2 + 4}} (P_D - Q_A) \\ M_{Dzl0} = \frac{1}{\sqrt{2\alpha^2 + 4}} (2M_{Dx} + \alpha M_{Dy} + \alpha M_{Dz}); M_{Dzl1} = \frac{\sqrt{2}}{2} (P_D + Q_A) \end{cases} \quad (5-21)$$

By using Eq. (5-17), the equations for the displacement in the y-direction and the moment in the z-direction is written as:

$$EI_z y_{Oi}''(s) = M_{izl0} + M_{izl1} (s - L_\alpha) \quad (5-22)$$

As the equations of beams are all established in their local coordinate system, it is assumed that there is no displacement at point O in the local coordinates system to consider all the connected beams in the same manner without losing the generality, and no rotation at point i (i=A, C and D) that respects the symmetry of the 1/8th unit cell. Therefore, the boundary conditions in the y-direction are given by:

$$y_{Oi}(0) = y_{Oi}'(L_\alpha) = 0 \quad (5-23)$$

Two successive integrations of Eq. (5-22) with the boundary condition in Eq. (5-23) give:

$$EI_z y_{Oi}'(s) = M_{izl0} (s - L_\alpha) + \frac{1}{2} M_{izl1} (s - L_\alpha)^2 \quad (5-24)$$

$$EI_z y_{Oi}(s) = \frac{1}{2} M_{izl0} (s^2 - 2sL_\alpha) + \frac{1}{6} M_{izl1} [(s - L_\alpha)^3 + L_\alpha^3] \quad (5-25)$$

By using Eq. (5-17), the equations for the displacement in the z-direction and the moment in the y-direction is written as:

$$-EI_y z_{Oi}''(s) = M_{iy10} + M_{iy11} (s - L_\alpha) \quad (5-26)$$

The boundary conditions in the z-direction for each beam Oi are:

$$z_{Oi}(0) = z_{Oi}'(L_\alpha) = 0 \quad (5-27)$$

Two successive integrations of Eq. (5-26) with the boundary condition in Eq. (5-27) give:

$$-EI_y z_{Oi}'(s) = M_{iy10} (s - L_\alpha) + \frac{1}{2} M_{iy11} (s - L_\alpha)^2 \quad (5-28)$$

$$-EI_y z_{Oi}(s) = \frac{1}{2} M_{iy10} [(s - L_\alpha)^2 - L_\alpha^2] + \frac{1}{6} M_{iy11} [(s - L_\alpha)^3 + L_\alpha^3] \quad (5-29)$$

The torsion for each beam Oi is:

$$GI_O \alpha'_{Oi}(s) = M_{ixl0} \quad (5-30)$$

where is β the rotation angle, I_O polar moment of inertia and G is the shear modulus.

The boundary condition is given at point i as follows:

$$\alpha_{Oi}(L_\alpha) = 0 \quad (5-31)$$

The integration of Eq. (5-30) with the boundary condition in Eq. (5-31) gives:

$$GI_O \alpha_{Oi}(s) = M_{ixl0}(s - L_\alpha) \quad (5-32)$$

By using Eqs. (5-25) and (5-29), the displacement vector of point i ($i = A, C$ and D) is expressed as follows:

$$\begin{aligned} \vec{u}_{Oi} &= y_{Oi}(L_\alpha) \vec{t}_{i\alpha 1} + z_{Oi}(L_\alpha) \vec{t}_{i\alpha 2} + \frac{N_i L_\alpha}{ES} \vec{n}_{i\alpha} \\ &= \left(-\frac{1}{2EI_z} M_{izl0} L_\alpha^2 + \frac{1}{6EI_z} M_{izl1} L_\alpha^3 \right) \vec{t}_{i\alpha 1} + \left(\frac{1}{2EI_y} M_{iy l0} L_\alpha^2 - \frac{1}{6EI_y} M_{iy l1} L_\alpha^3 \right) \vec{t}_{i\alpha 2} + \frac{N_i}{ES} \vec{n}_{i\alpha} L_\alpha \end{aligned} \quad (5-33)$$

By using the Eq. (4-27), the displacements \vec{u}_{Oi} are expressed as follows:

$$\vec{u}_{OA} = \frac{L_\alpha}{E} \left[\frac{\sqrt{2}}{12I_z} (-3M_{Azl0} L_\alpha + M_{Azl1} L_\alpha^2) \begin{Bmatrix} 0 \\ -1 \\ -1 \end{Bmatrix} - \frac{\sqrt{2}}{12I_y} (-3M_{Ayl0} L_\alpha + M_{Ayl1} L_\alpha^2) \frac{1}{\sqrt{\alpha^2 + 2}} \begin{Bmatrix} 2 \\ -\alpha \\ \alpha \end{Bmatrix} + \frac{N_A}{S} \frac{1}{\sqrt{\alpha^2 + 2}} \begin{Bmatrix} -\alpha \\ -1 \\ 1 \end{Bmatrix} \right] \quad (5-34)$$

$$\vec{u}_{OC} = \frac{L_\alpha}{E} \left[\frac{\sqrt{2}}{12I_z} (-3M_{Czl0} L_\alpha + M_{Czl1} L_\alpha^2) \begin{Bmatrix} 0 \\ 1 \\ 1 \end{Bmatrix} - \frac{\sqrt{2}}{12I_y} (-3M_{Cyl0} L_\alpha + M_{Cyl1} L_\alpha^2) \frac{1}{\sqrt{\alpha^2 + 2}} \begin{Bmatrix} 2 \\ \alpha \\ -\alpha \end{Bmatrix} + \frac{N_C}{S} \frac{1}{\sqrt{\alpha^2 + 2}} \begin{Bmatrix} -\alpha \\ 1 \\ -1 \end{Bmatrix} \right] \quad (5-35)$$

$$\vec{u}_{OD} = \frac{L_\alpha}{E} \left[\frac{\sqrt{2}}{12I_z} (-3M_{Dzl0} L_\alpha + M_{Dzl1} L_\alpha^2) \begin{Bmatrix} 0 \\ 1 \\ -1 \end{Bmatrix} - \frac{\sqrt{2}}{12I_y} (-3M_{Dyl0} L_\alpha + M_{Dyl1} L_\alpha^2) \frac{1}{\sqrt{\alpha^2 + 2}} \begin{Bmatrix} 2 \\ \alpha \\ \alpha \end{Bmatrix} + \frac{N_D}{S} \frac{1}{\sqrt{\alpha^2 + 2}} \begin{Bmatrix} \alpha \\ -1 \\ -1 \end{Bmatrix} \right] \quad (5-36)$$

By using Eqs. (5-24), (5-29) and (5-32), the rotation vector of point O in beam i is expressed as:

$$\begin{aligned} \vec{\theta}_{Oi}(0) &= y'_{Oi}(0) \vec{t}_{i\alpha 2} - z'_{Oi}(0) \vec{t}_{i\alpha 1} + \alpha_{Oi}(0) \vec{n}_{i\alpha} = \\ &= \frac{L_\alpha}{E} \left[\frac{1}{I_z} \left(-M_{izl0} + \frac{1}{2} M_{izl1} L_\alpha \right) \vec{t}_{i\alpha 2} + \frac{1}{I_y} \left(-M_{iy l0} + \frac{1}{2} M_{iy l1} L_\alpha \right) \vec{t}_{i\alpha 1} - \frac{2(1+\nu) M_{ixl0}}{I_O} \vec{n}_{i\alpha} \right] \end{aligned} \quad (5-37)$$

By using Eq. (4-27), $\vec{\theta}_{Oi}(0)$ are rewritten as follows:

$$\bar{\theta}_{OA}(0) = \frac{L_\alpha}{E} \left[\frac{-2M_{Azl0} + M_{Azl1}L_\alpha}{2I_z\sqrt{2\alpha^2 + 4}} \begin{Bmatrix} 2 \\ -\alpha \\ \alpha \end{Bmatrix} + \frac{-2M_{Ayl0} + M_{Ayl1}L_\alpha}{2\sqrt{2}I_y} \begin{Bmatrix} 0 \\ -1 \\ -1 \end{Bmatrix} - \frac{2(1+\nu)}{\sqrt{\alpha^2 + 2I_o}} M_{Axl0} \begin{Bmatrix} -\alpha \\ -1 \\ 1 \end{Bmatrix} \right] \quad (5-38)$$

$$\bar{\theta}_{OC}(0) = \frac{L_\alpha}{E} \left[\frac{-2M_{Czl0} + M_{Czl1}L_\alpha}{2\sqrt{2\alpha^2 + 4}I_z} \begin{Bmatrix} 2 \\ \alpha \\ -\alpha \end{Bmatrix} + \frac{-2M_{Cyl0} + M_{Cyl1}L_\alpha}{2\sqrt{2}I_y} \begin{Bmatrix} 0 \\ 1 \\ 1 \end{Bmatrix} - \frac{2(1+\nu)}{\sqrt{\alpha^2 + 2I_o}} M_{Cxl0} \begin{Bmatrix} -\alpha \\ 1 \\ -1 \end{Bmatrix} \right] \quad (5-39)$$

$$\bar{\theta}_{OC}(0) = \frac{L_\alpha}{E} \left[\frac{-2M_{Czl0} + M_{Czl1}L_\alpha}{2\sqrt{2\alpha^2 + 4}I_z} \begin{Bmatrix} 2 \\ \alpha \\ -\alpha \end{Bmatrix} + \frac{-2M_{Cyl0} + M_{Cyl1}L_\alpha}{2\sqrt{2}I_y} \begin{Bmatrix} 0 \\ 1 \\ 1 \end{Bmatrix} - \frac{2(1+\nu)}{\sqrt{\alpha^2 + 2I_o}} M_{Cxl0} \begin{Bmatrix} -\alpha \\ 1 \\ -1 \end{Bmatrix} \right] \quad (5-40)$$

For the particular case of point B of beam OB , the equation for the displacement in the y -direction and the moment in the z -direction is given as:

$$EI_z y''_{OB}(s) = M_{Bzl}(s - L_\alpha) \quad (5-41)$$

The boundary condition of beam OB in the y direction is:

$$y_{OB}(0) = 0 \quad (5-42)$$

Two successive integrations of Eq. (5-41) by considering Eq. (5-42) give:

$$EI_z y'_{OB}(s) = \frac{1}{2} M_{Bzl} (s - L_\alpha)^2 + C_{By} \quad (5-43)$$

$$EI_z y_{OB}(s) = \frac{1}{6} M_{Bzl} \left[(s - L_\alpha)^3 + L_\alpha^3 \right] + C_{By} s \quad (5-44)$$

The equations for the displacement in the z -direction and the moment in the y -direction are then expressed as:

$$-EI_y z''_{OB}(s) = M_{Byl}(s - L_\alpha) \quad (5-45)$$

and the boundary condition of beam OB in the z direction is:

$$z_{OB}(0) = 0 \quad (5-46)$$

Two successive integrations of Eq. (5-45) by considering Eq. (5-46) give:

$$-EI_y z'_{OB}(s) = \frac{1}{2} M_{Byl} (s - L_\alpha)^2 + C_{Bz} \quad (5-47)$$

$$-EI_y z_{OB}(s) = \frac{1}{6} M_{Byl} \left[(s - L_\alpha)^3 + L_\alpha^3 \right] + C_{Bz} s \quad (5-48)$$

There is no torsion from point O to B in beam OB as point B is free, and the constant rigid rotation angle about $\vec{n}_{B\alpha}$ is:

$$GI_O \alpha'_{OB}(s) = M_{Bxl0} = 0 \quad (5-49)$$

The integration of the above equation gives:

$$GI_{iO} \alpha_{Oi}(s) = C_{B\alpha} \quad (5-50)$$

The displacement vector of beam OB at point B is given by using Eqs. (4-27), (5-44), and (5-48):

$$\begin{aligned} \vec{u}_{OB} &= y_{OB}(L_\alpha) \vec{t}_{B\alpha 1} + z_{OB}(L_\alpha) \vec{t}_{B\alpha 2} + \frac{N_B L_\alpha}{ES} \vec{n}_{B\alpha} \\ &= \left(\frac{1}{6EI_z} M_{Bzl1} L_\alpha^3 + \frac{C_{By}}{EI_z} L_\alpha \right) \vec{t}_{B\alpha 1} - \left(\frac{1}{6EI_y} M_{Byl1} L_\alpha^3 + \frac{C_{Bz}}{EI_y} L_\alpha \right) \vec{t}_{B\alpha 2} + \frac{N_B}{ES} \vec{n}_{B\alpha} L_\alpha \end{aligned} \quad (5-51)$$

The rotation vector of beam OB at point O is given by using Eqs. (4-27), (5-43), (5-47) and (5-50):

$$\begin{aligned} \vec{\theta}_{OB}(0) &= y'_{OB}(0) \vec{t}_{B\alpha 2} - z'_{OB}(0) \vec{t}_{B\alpha 1} + \alpha_{OB}(0) \vec{n}_{B\alpha} \\ &= \frac{1}{E} \left[\left(\frac{1}{2I_z} M_{Bzl1} L_\alpha^2 + \frac{C_{yt}}{I_z} \right) \frac{1}{\sqrt{2\alpha^2 + 4}} \begin{Bmatrix} 2 \\ -\alpha \\ -\alpha \end{Bmatrix} + \left(\frac{1}{2I_y} M_{Byl1} L_\alpha^2 + \frac{C_{Bz}}{I_y} \right) \frac{1}{\sqrt{2}} \begin{Bmatrix} 0 \\ -1 \\ 1 \end{Bmatrix} + \frac{2(1+\nu)C_{B\alpha}}{I_o} \frac{1}{\sqrt{\alpha^2 + 2}} \begin{Bmatrix} \alpha \\ 1 \\ 1 \end{Bmatrix} \right] \end{aligned} \quad (5-52)$$

The undetermined coefficient $C_{B\alpha}$ in the above equation will not be chosen as a variable of the equation system as point B is free in rotation that doesn't make a constraint to the structure.

The boundary conditions given in Eq. (5-5) and (5-6) are used hereafter to establish the system of equations:

Combining Eqs. (5-5), (5-34) and (5-30) leads to:

$$\begin{aligned} & -\frac{\sqrt{2}}{12I_z} \left[-3M_{Azl0} L_\alpha + (M_{Azl1} + M_{Bzl1}) L_\alpha^2 + 6C_{By} \right] - \frac{\sqrt{2}}{12I_y} \left[-3M_{Ayl0} L_\alpha + (M_{Ayl1} + M_{Byl1}) L_\alpha^2 + 6C_{Bz} \right] \frac{\alpha}{\sqrt{\alpha^2 + 2}} \\ & + \frac{N_A - N_B}{S} \frac{1}{\sqrt{\alpha^2 + 2}} = 0 \end{aligned} \quad (5-53)$$

Combining Eqs. (5-5), (5-35) and (5-36) leads to:

$$\begin{aligned} & \frac{\sqrt{2}}{12I_z} \left[-3(M_{Czl0} + M_{Dzl0}) L_\alpha + (M_{Czl1} + M_{Dzl1}) L_\alpha^2 \right] \\ & + \frac{\sqrt{2}}{12I_y} \left[-3(M_{Cyl0} + M_{Dyl0}) L_\alpha + (M_{Cyl1} + M_{Dyl1}) L_\alpha^2 \right] \frac{\alpha}{\sqrt{\alpha^2 + 2}} - \frac{N_C - N_D}{S\sqrt{\alpha^2 + 2}} = 0 \end{aligned} \quad (5-54)$$

Combining Eqs. (5-5), (5-34) and (5-36) leads to:

$$\begin{aligned}
 & -\frac{\sqrt{2}}{12I_z} \left[-3(M_{Azl0} - M_{Dzl0})L_\alpha + (M_{Azl1} - M_{Dzl1})L_\alpha^2 \right] \\
 & -\frac{\sqrt{2}}{12I_y} \left[-3(M_{Ayl0} - M_{Dyl0})L_\alpha + (M_{Ayl1} - M_{Dyl1})L_\alpha^2 \right] \frac{\alpha}{\sqrt{\alpha^2 + 2}} + \frac{N_A + N_D}{\sqrt{\alpha^2 + 2S}} = \frac{EW}{L_\alpha}
 \end{aligned} \tag{5-55}$$

Combining Eqs. (5-5), (5-34) and (5-35) leads to:

$$\frac{\sqrt{2}}{6I_y} \left[-3(M_{Ayl0} - M_{Cyl0})L_\alpha + (M_{Ayl1} - M_{Cyl1})L_\alpha^2 \right] + \frac{\alpha(N_A - N_C)}{S} = 0 \tag{5-56}$$

Combining Eqs. (5-5), (5-34) and (5-36) leads to:

$$\begin{aligned}
 & \frac{\sqrt{2}}{12I_z} \left[-3(M_{Azl0} + M_{Dzl0})L_\alpha + (M_{Azl1} + M_{Dzl1})L_\alpha^2 \right] \\
 & -\frac{\sqrt{2}}{12I_y} \left[-3(M_{Ayl0} + M_{Dyl0})L_\alpha + (M_{Ayl1} + M_{Dyl1})L_\alpha^2 \right] \frac{\alpha}{\sqrt{\alpha^2 + 2}} + \frac{N_A - N_D}{\sqrt{\alpha^2 + 2S}} = 0
 \end{aligned} \tag{5-57}$$

By using $\theta_{\alpha x}(0) = \theta_{\alpha c x}(0)$ and $\theta_{\alpha y}(0) \pm \theta_{\alpha z}(0) = \theta_{\alpha c y}(0) \pm \theta_{\alpha c z}(0)$ that is equivalent with

Eq. (5-6), with Eqs. (5-38) and (5-39), we have:

$$\frac{\sqrt{2}}{2I_z} \left[-2(M_{Azl0} - M_{Czl0}) + (M_{Azl1} - M_{Czl1})L_\alpha \right] + \alpha \frac{2(1+\nu)}{I_o} (M_{Axl0} - M_{Cxl0}) = 0 \tag{5-58}$$

$$-2(M_{Ayl0} + M_{Cyl0}) + (M_{Ayl1} + M_{Cyl1})L_\alpha = 0 \tag{5-59}$$

$$\frac{\sqrt{2}\alpha}{4I_z} \left[-2(M_{Azl0} + M_{Czl0}) + (M_{Azl1} + M_{Czl1})L_\alpha \right] - \frac{2(1+\nu)}{I_o} (M_{Axl0} + M_{Cxl0}) = 0 \tag{5-60}$$

By using $\theta_{\alpha x}(0) = \theta_{\alpha D x}(0)$, $\theta_{\alpha y}(0) \pm \theta_{\alpha z}(0) = \theta_{\alpha D y}(0) \pm \theta_{\alpha D z}(0)$ that is equivalent with Eq. (5-

6), with Eqs. (5-38) and (5-40), we have:

$$\frac{\sqrt{2}}{2I_z} \left[-2(M_{Azl0} - M_{Dzl0}) + (M_{Azl1} - M_{Dzl1})L_\alpha \right] + \alpha \frac{2(1+\nu)}{I_o} (M_{Axl0} + M_{Dxl0}) = 0 \tag{5-61}$$

$$\frac{\sqrt{2}}{4I_y} (-2M_{Ayl0} + M_{Ayl1}L_\alpha) + \frac{\sqrt{2}\alpha}{4\sqrt{\alpha^2 + 2I_z}} (-2M_{Dzl0} + M_{Dzl1}L_\alpha) + \frac{2(1+\nu)}{\sqrt{\alpha^2 + 2I_o}} M_{Dxl0} = 0 \tag{5-62}$$

$$\frac{\sqrt{2}\alpha}{4\sqrt{\alpha^2 + 2I_z}} (-2M_{Azl0} + M_{Azl1}L_\alpha) + \frac{\sqrt{2}}{4I_y} (-2M_{Dyl0} + M_{Dyl1}L_\alpha) - \frac{2(1+\nu)}{\sqrt{\alpha^2 + 2I_o}} M_{Axl0} = 0 \tag{5-63}$$

By using $\theta_{O_{Ay}}(0) \pm \theta_{O_{Az}}(0) = \theta_{O_{By}}(0) \pm \theta_{O_{Bz}}(0)$ in Eq. (5-6), (5-38) and (5-52), the rotation is not excluded from the equation system, and we have:

$$\frac{-\sqrt{2}\alpha}{2I_z\sqrt{\alpha^2+2}}(-2M_{Azl0}L_\alpha + M_{Azl1}L_\alpha^2) + \frac{\sqrt{2}}{4I_y}(M_{Byl1}L_\alpha^2 + 2C_{Bz}) + \frac{2(1+\nu)}{\sqrt{\alpha^2+2}I_o}M_{Axl0}L_\alpha = 0 \quad (5-64)$$

$$\frac{\sqrt{\alpha^2+2}}{I_z}[-2M_{Azl0}L_\alpha + (M_{Azl1} - M_{Bzl1})L_\alpha^2 - 2C_{By}] + \frac{\alpha}{I_y}[-2M_{Ayl0}L_\alpha + (M_{Ayl1} - M_{Byl1})L_\alpha^2 - 2C_{Bz}] = 0 \quad (5-65)$$

Finally, Eq. (5-10), the 3 equations in Eq. (5-11) and Eqs. (5-53) to (5-65) constitute the system of 17 equations of 17 unknown variables: $P_A, P_B, P_C, P_D, \vec{M}_A, \vec{M}_B, \vec{M}_C, \vec{M}_D, C_{By}, C_{Bz}$

After determining the 17 unknown variables, the relative effective modulus of elasticity can be calculated as follows:

$$\frac{E_{eff}}{E} = -\frac{2(P_A + P_B)}{E\alpha bW} \quad (5-66)$$

The Poisson's ratio can be approximated by the maximum displacement of point B and C or that of point B and D with respect to point A as follows:

$$\nu_{zy} = -\frac{\varepsilon_y}{\varepsilon_z} = -\frac{h}{bW} \max(|u_{By}|, |u_{Cy}|) \quad (5-67)$$

$$\nu_{zx} = -\frac{\varepsilon_x}{\varepsilon_z} = -\frac{h}{bW} \max(|u_{By}|, |u_{Dy}|) \quad (5-68)$$

The displacements used in the above equations are given by Eqs. (5-33) and (5-51).

5.3 Analytical model for upper bound of effective elastic modulus

In open lattice structures, there is a special case where the lattice structure forms an infinite array in both the m and n directions, as shown in Fig. 5.4. Traditionally, this type of structure is classified under the discussion of closed lattice structures. However, in order to accurately analyze the existence of this particular case, it is treated as a separate analysis. In this configuration, each individual cell is arranged in a mirror-symmetrical manner in two directions on the plane, with the number of cells approaching infinity.

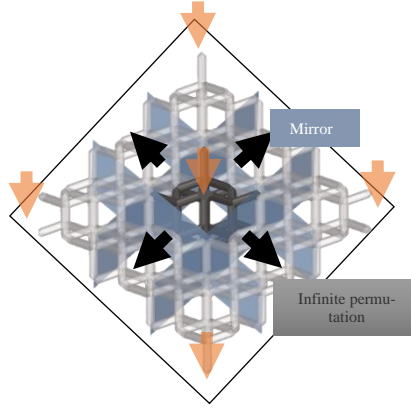


Fig. 5.4 The variables m and n undergo infinite arrays on the plane

The upper bound of effective elastic modulus in the Z -direction is obtained for $m \rightarrow \infty$ and $n \rightarrow \infty$ by imposing the following boundary conditions with constant displacement in the global coordinate system:

$$\begin{cases} \text{Point A: } U_A = V_A = 0; W_A = W; \theta_{Ax} = \theta_{Ay} = \theta_{Az} = 0 \\ \text{Point B: } W_B = W; \theta_{Bx} = \theta_{By} = \theta_{Bz} = 0 \\ \text{Point C: } U_C = W_C = 0; \theta_{Cx} = \theta_{Cy} = \theta_{Cz} = 0 \\ \text{Point D: } V_D = W_D = 0; \theta_{Dx} = \theta_{Dy} = \theta_{Dz} = 0 \end{cases} \quad (5-69)$$

For $X=X_{\max}$ and $Y=Y_{\max}$, two supplementary relative-displacement boundary conditions are imposed as follows:

$$\begin{cases} U_B = U_D \\ V_B = V_C \end{cases} \quad (5-70)$$

By considering the symmetry of the unit cell in the plane XO_gY and the force balance, the forces on the $1/8^{\text{th}}$ unit cell are supposed to be as shown in Fig. 5.3b with:

$$\vec{P}_A = \begin{Bmatrix} H_A \\ Q_A \\ -P_A \end{Bmatrix}, \vec{P}_B = \begin{Bmatrix} H_B \\ Q_B \\ -P_B \end{Bmatrix} \quad (5-71)$$

In a symmetric plane of a border-free problem, the sum of the normal force is zero, by using four symmetric planes ZO_gX , YO_gZ , $X=X_{\max}$ and $Y=Y_{\max}$, \vec{P}_C and \vec{P}_D in the X -direction and the Y -direction are function of \vec{P}_A and \vec{P}_B , and \vec{P}_C and \vec{P}_D as:

$$\vec{P}_C = \begin{Bmatrix} -H_A \\ -Q_B \\ P_C \end{Bmatrix}, \vec{P}_D = \begin{Bmatrix} -H_B \\ -Q_A \\ P_D \end{Bmatrix} \quad (5-72)$$

The moments at the points as shown in Fig.5.3b are as follows:

$$\vec{M}_A = \begin{Bmatrix} M_{Ax} \\ M_{Ay} \\ M_{Az} \end{Bmatrix}, \vec{M}_B = \begin{Bmatrix} M_{Bx} \\ M_{By} \\ M_{Bz} \end{Bmatrix}, \vec{M}_C = \begin{Bmatrix} M_{Cx} \\ M_{Cy} \\ M_{Cz} \end{Bmatrix}, \vec{M}_D = \begin{Bmatrix} M_{Dx} \\ M_{Dy} \\ M_{Dz} \end{Bmatrix} \quad (5-73)$$

The problem of the whole structure with 16 unknown variables is solvable with 4 equilibrium equations and boundary conditions will generate 12 equations.

Equation (5-10) of balance of forces applies also to this case and balance of moments can be written as follows:

$$\begin{Bmatrix} M_{Ax} + M_{Bx} + M_{Cx} + M_{Dx} \\ M_{Ay} + M_{By} + M_{Cy} + M_{Dy} \\ M_{Az} + M_{Bz} + M_{Cz} + M_{Dz} \end{Bmatrix} + \begin{Bmatrix} P_A - P_B + P_C - P_D - 2(Q_B + Q_A) \\ \alpha(-P_A + P_B + P_C - P_D) + 2(H_A + H_B) \\ 2\alpha(-Q_A + Q_B) + 2(H_A - H_B) \end{Bmatrix} \frac{L_\alpha}{\sqrt{\alpha^2 + 2}} = \vec{0} \quad (5-74)$$

The displacements and rotations boundary conditions are given by Eqs. (5-75) and (5-76):

$$\begin{cases} W_A = W_B \\ W_C = W_D \\ W_A - W_D = W \\ U_A = U_C \\ V_A = V_D \\ U_B = U_D \\ V_B = V_C \end{cases} \quad (5-75)$$

$$\begin{cases} \vec{\theta}_{OA}(0) = \vec{\theta}_{OC}(0) \\ \vec{\theta}_{OA}(0) = \vec{\theta}_{OD}(0) \\ \vec{\theta}_{OA}(0) = \vec{\theta}_{OB}(0) \end{cases} \quad (5-76)$$

In order not to repeat the equations, the equations obtained in the last section are reused, if not changed, and only the different equations or new ones will be detailed hereafter.

The normal forces are expressed as follows:

$$N_A = \vec{P}_A \cdot \vec{n}_{A\alpha} = \frac{1}{\sqrt{\alpha^2 + 2}} (-P_A - \alpha H_A - Q_A) \quad (5-77)$$

$$N_B = \vec{P}_B \cdot \vec{n}_{B\alpha} = \frac{1}{\sqrt{\alpha^2 + 2}} (-P_B + \alpha H_B + Q_B) \quad (5-78)$$

$$N_C = \vec{P}_{CA} \cdot \vec{n}_{C\alpha} = \frac{1}{\sqrt{\alpha^2 + 2}} (-P_C + \alpha H_A - Q_B) \quad (5-79)$$

$$N_D = \vec{P}_D \cdot \vec{n}_{D\alpha} = \frac{1}{\sqrt{\alpha^2 + 2}} (-P_D + Q_A - \alpha H_B) \quad (5-80)$$

As for the previous case, the moments in beam sections can be written as:

$$\left\{ \begin{array}{l} M_{Axl0} = \frac{1}{\sqrt{\alpha^2 + 2}} (\alpha M_{Ax} + M_{Ay} - M_{Az}) \\ M_{Ayl0} = -\frac{\sqrt{2}}{2} (M_{Ay} + M_{Az}); M_{Ayl1} = \frac{1}{\sqrt{2\alpha^2 + 4}} (-\alpha P_A + 2H_A - \alpha Q_A) \\ M_{Azl0} = \frac{1}{\sqrt{2\alpha^2 + 4}} (2M_{Ax} - \alpha M_{Ay} + \alpha M_{Az}); M_{Azl1} = \frac{\sqrt{2}}{2} (-P_A + Q_A) \end{array} \right. \quad (5-81)$$

$$\left\{ \begin{array}{l} M_{Bxl0} = \frac{1}{\sqrt{\alpha^2 + 2}} (\alpha M_{Bx} + M_{By} + M_{Bz}) \\ M_{Byl0} = \frac{\sqrt{2}}{2} (-M_{By} + M_{Bz}); M_{Byl1} = \frac{1}{\sqrt{2\alpha^2 + 4}} (\alpha P_B + 2H_B - \alpha Q_B) \\ M_{Bzl0} = \frac{1}{\sqrt{2\alpha^2 + 4}} (2M_{Bx} - \alpha M_{By} - \alpha M_{Bz}); M_{Bzl1} = \frac{1}{\sqrt{2}} (P_B + Q_B) \end{array} \right. \quad (5-82)$$

$$\left\{ \begin{array}{l} M_{Cxl0} = \frac{1}{\sqrt{\alpha^2 + 2}} (-\alpha M_{Cx} + M_{Cy} - M_{Cz}) \\ M_{Cyl0} = \frac{\sqrt{2}}{2} (M_{Cy} + M_{Cz}); M_{Cyl1} = -\frac{1}{\sqrt{2\alpha^2 + 4}} (\alpha P_C + 2H_C + \alpha Q_C) \\ M_{Czl0} = \frac{1}{\sqrt{2\alpha^2 + 4}} (2M_{Cx} + \alpha M_{Cy} - \alpha M_{Cz}); M_{Czl1} = \frac{1}{\sqrt{2}} (-P_C + Q_C) \end{array} \right. \quad (5-83)$$

$$\left\{ \begin{array}{l} M_{Dxl0} = \frac{1}{\sqrt{\alpha^2 + 2}} (\alpha M_{Dx} - M_{Dy} - M_{Dz}) \\ M_{Dyl0} = \frac{\sqrt{2}}{2} (M_{Dy} - M_{Dz}); M_{Dyl1} = \frac{1}{\sqrt{2\alpha^2 + 4}} (\alpha P_D - \alpha Q_A - 2H_D) \\ M_{Dzl0} = \frac{1}{\sqrt{2\alpha^2 + 4}} (2M_{Dx} + \alpha M_{Dy} + \alpha M_{Dz}); M_{Dzl1} = \frac{1}{\sqrt{2}} (P_D + Q_A) \end{array} \right. \quad (5-84)$$

The other mathematical developments remain unchanged except for the following equations, where \vec{u}_{OB} and $\vec{\theta}_{OB}(0)$ are defined as:

$$\vec{u}_{OB} = \frac{\sqrt{2}}{12EI_z} (-3M_{Bz0}L_\alpha^2 + M_{Bz1}L_\alpha^3) \begin{Bmatrix} 0 \\ -1 \\ 1 \end{Bmatrix} - \frac{\sqrt{2}}{12EI_y} (-3M_{By0}L_\alpha^2 + M_{By1}L_\alpha^3) \frac{1}{\sqrt{\alpha^2 + 2}} \begin{Bmatrix} 2 \\ -\alpha \\ -\alpha \end{Bmatrix} + \frac{N_B L_\alpha}{ES} \frac{1}{\sqrt{\alpha^2 + 2}} \begin{Bmatrix} \alpha \\ 1 \\ 1 \end{Bmatrix} \quad (5-85)$$

$$\bar{\theta}_{OB}(0) = \frac{L_\alpha}{E} \left[\frac{-2M_{Bz10} + M_{Bz11}L_\alpha}{2\sqrt{2\alpha^2 + 4I_z}} \begin{Bmatrix} 2 \\ -\alpha \\ -\alpha \end{Bmatrix} + \frac{-2M_{By10} + M_{By11}L_\alpha}{2\sqrt{2I_y}} \begin{Bmatrix} 0 \\ -1 \\ 1 \end{Bmatrix} - \frac{2(1+\nu)M_{Bx10}}{\sqrt{\alpha^2 + 2I_o}} \begin{Bmatrix} \alpha \\ 1 \\ 1 \end{Bmatrix} \right] \quad (5-86)$$

and by considering the new boundary conditions given in Eqs. (5-75) and (5-76):

$$\begin{aligned} & -\frac{\sqrt{2}}{12I_z} \left[-3(M_{Az10} + M_{Bz10})L_\alpha + (M_{Az11} + M_{Bz11})L_\alpha^2 \right] \\ & -\frac{\sqrt{2}}{12I_y} \left(-3(M_{Ay10} + M_{By10})L_\alpha + (M_{Ay11} + M_{By11})L_\alpha^2 \right) \frac{\alpha}{\sqrt{\alpha^2 + 2}} + \frac{N_A - N_B}{S} \frac{1}{\sqrt{\alpha^2 + 2}} = 0 \end{aligned} \quad (5-87)$$

$$\frac{1}{\sqrt{2I_z}} \left[-2(M_{Az10} - M_{Bz10}) + (M_{Az11} - M_{Bz11})L_\alpha \right] + \alpha \frac{2(1+\nu)}{I_o} (M_{Ax10} + M_{Bx10}) = 0 \quad (5-88)$$

$$\frac{1}{2\sqrt{2I_y}} (-2M_{Ay10} + M_{Ay11}L_\alpha) - \frac{\alpha}{2\sqrt{2\alpha^2 + 4I_z}} (-2M_{Bz10} + M_{Bz11}L_\alpha) - \frac{2(1+\nu)}{\sqrt{\alpha^2 + 2I_o}} M_{Bx10} = 0 \quad (5-89)$$

$$\frac{\alpha}{2\sqrt{2\alpha^2 + 4I_z}} (-2M_{Az10} + M_{Az11}L_\alpha) - \frac{1}{2\sqrt{2I_y}} (-2M_{By10} + M_{By11}L_\alpha) - \frac{2(1+\nu)}{\sqrt{\alpha^2 + 2I_o}} M_{Ax10} = 0 \quad (5-90)$$

$$-\frac{\sqrt{2}}{12I_y} \left(-3(M_{By10} - M_{Dy10})L_\alpha + (M_{By11} - M_{Dy11})L_\alpha^2 \right) + \frac{N_B - N_D}{S} \alpha = 0 \quad (5-91)$$

$$\begin{aligned} & -\frac{\sqrt{2}}{12I_z} \left[-3(M_{Bz10} + M_{Cz10})L_\alpha + (M_{Bz11} + M_{Cz11})L_\alpha^2 \right] \\ & + \frac{\sqrt{2}\alpha}{12\sqrt{\alpha^2 + 2I_y}} \left[-3(M_{By10} + M_{Cy10})L_\alpha + (M_{By11} + M_{Cy11})L_\alpha^2 \right] + \frac{N_B - N_C}{\sqrt{\alpha^2 + 2S}} = 0 \end{aligned} \quad (5-92)$$

After determining the 16 unknown variables, the relative effective modulus of elasticity and Poisson's ratios can be calculated by Eqs. (5-66), (5-67) and (5-68), respectively.

5.4 Modeling for structure with border constraint

For the structure with border constraint, the boundary conditions with constant displacement in the global coordinate system are:

$$\begin{cases} \text{Point A: } U_A = V_A = 0; W_A = W; \theta_{Ax} = \theta_{Ay} = \theta_{Az} = 0 \\ \text{Point B: } U_B = V_B = 0; W_B = W; \theta_{Bx} = \theta_{By} = \theta_{Bz} = 0 \\ \text{Point C: } U_C = V_C = W_C = 0; \theta_{Cx} = \theta_{Cy} = \theta_{Cz} = 0 \\ \text{Point D: } U_D = V_D = W_D = 0; \theta_{Dx} = \theta_{Dy} = \theta_{Dz} = 0 \end{cases} \quad (5-93)$$

Boundary conditions of the relative displacements are given by Eqs. (5-75) and (5-76), with two supplementary ones:

$$\begin{cases} U_A = U_D \\ V_A = V_C \end{cases} \quad (5-94)$$

The forces on the 1/8th unit cell are supposed to be as shown in Fig. 5.3c:

$$\vec{P}_A = \begin{Bmatrix} H_A \\ Q_A \\ -P_A \end{Bmatrix}; \vec{P}_B = \begin{Bmatrix} H_B \\ Q_B \\ -P_B \end{Bmatrix}; \vec{P}_C = \begin{Bmatrix} H_C \\ Q_C \\ P_C \end{Bmatrix}; \vec{P}_D = \begin{Bmatrix} H_D \\ Q_D \\ P_D \end{Bmatrix} \quad (5-95)$$

The moments are same as Eq. (5-3 to 5-72).

There are 24 unknown variables in total in the components of forces and moments. The problem can be solved with 6 equilibrium equations and 18 equations generated by the boundary conditions.

The balance of moments can be written as follows:

$$\begin{Bmatrix} M_{Ax} + M_{Bx} + M_{Cx} + M_{Dx} \\ M_{Ay} + M_{By} + M_{Cy} + M_{Dy} \\ M_{Az} + M_{Bz} + M_{Cz} + M_{Dz} \end{Bmatrix} + \begin{Bmatrix} P_A - P_B + P_C - P_D - Q_A - Q_B + Q_C + Q_D \\ \alpha(-P_A + P_B + P_C - P_D) + H_A + H_B - H_C - H_D \\ H_A - H_B - H_C + H_D + \alpha(-Q_A + Q_B - Q_C + Q_D) \end{Bmatrix} \frac{L_\alpha}{\sqrt{\alpha^2 + 2}} = \vec{0} \quad (5-96)$$

The balance of forces can be written as follows:

$$\begin{cases} \sum F_x = 0 \Rightarrow H_A + H_B + H_C + H_D = 0 \\ \sum F_y = 0 \Rightarrow Q_A + Q_B + Q_C + Q_D = 0 \end{cases} \quad (5-97)$$

The normal forces are expressed as follows:

$$N_A = \vec{P}_A \cdot \vec{n}_{A\alpha} = \frac{1}{\sqrt{\alpha^2 + 2}} (-P_A - \alpha H_A - Q_A) \quad (5-98)$$

$$N_A = \vec{P}_B \cdot \vec{n}_{B\alpha} = \frac{1}{\sqrt{\alpha^2 + 2}} (-P_B + \alpha H_B + Q_B) \quad (5-99)$$

$$N_C = \vec{P}_C \cdot \vec{n}_{C\alpha} = \frac{1}{\sqrt{\alpha^2 + 2}} (-\alpha H_C + Q_C - P_C) \quad (5-100)$$

$$N_D = \vec{P}_D \cdot \vec{n}_{D\alpha} = \frac{1}{\sqrt{\alpha^2 + 2}} (\alpha H_D - Q_D - P_D) \quad (5-101)$$

As for the previous case, the moments in beam sections can be written as:

$$\left\{ \begin{array}{l} M_{Axl0} = \frac{1}{\sqrt{\alpha^2 + 2}} (\alpha M_{Ax} + M_{Ay} - M_{Az}) \\ M_{Ayl0} = -\frac{\sqrt{2}}{2} (M_{Ay} + M_{Az}); M_{Ayl1} = \frac{1}{\sqrt{2\alpha^2 + 4}} (-\alpha P_A + 2H_A - \alpha Q_A) \\ M_{Azl0} = \frac{1}{\sqrt{2\alpha^2 + 4}} (2M_{Ax} - \alpha M_{Ay} + \alpha M_{Az}); M_{Azl1} = \frac{\sqrt{2}}{2} (-P_A + Q_A) \end{array} \right. \quad (5-102)$$

$$\left\{ \begin{array}{l} M_{Bxl0} = \frac{1}{\sqrt{\alpha^2 + 2}} (\alpha M_{Bx} + M_{By} + M_{Bz}) \\ M_{Byl0} = \frac{\sqrt{2}}{2} (-M_{By} + M_{Bz}); M_{Byl1} = \frac{1}{\sqrt{2\alpha^2 + 4}} (\alpha P_B + 2H_B - \alpha Q_B) \\ M_{Bzl0} = \frac{1}{\sqrt{2\alpha^2 + 4}} (2M_{Bx} - \alpha M_{By} - \alpha M_{Bz}); M_{Bzl1} = \frac{1}{\sqrt{2}} (P_B + Q_B) \end{array} \right. \quad (5-103)$$

$$\left\{ \begin{array}{l} M_{Cxl0} = \frac{1}{\sqrt{\alpha^2 + 2}} (-\alpha M_{Cx} + M_{Cy} - M_{Cz}) \\ M_{Cyl0} = \frac{\sqrt{2}}{2} (M_{Cy} + M_{Cz}); M_{Cyl1} = \frac{1}{\sqrt{2\alpha^2 + 4}} (-\alpha P_C + 2H_C + \alpha Q_C) \\ M_{Czl0} = \frac{1}{\sqrt{2\alpha^2 + 4}} (2M_{Cx} + \alpha M_{Cy} - \alpha M_{Cz}); M_{Czl1} = -\frac{1}{\sqrt{2}} (P_C + Q_C) \end{array} \right. \quad (5-104)$$

$$\left\{ \begin{array}{l} M_{Dxl0} = \frac{1}{\sqrt{\alpha^2 + 2}} (\alpha M_{Dx} - M_{Dy} - M_{Dz}) \\ M_{Dyl0} = \frac{\sqrt{2}}{2} (M_{Dy} - M_{Dz}); M_{Dyl1} = \frac{1}{\sqrt{2\alpha^2 + 4}} (\alpha P_D + \alpha Q_D + 2H_D) \\ M_{Dzl0} = \frac{1}{\sqrt{2\alpha^2 + 4}} (2M_{Dx} + \alpha M_{Dy} + \alpha M_{Dz}); M_{Dzl1} = \frac{1}{\sqrt{2}} (P_D - Q_D) \end{array} \right. \quad (5-105)$$

The other mathematical developments remain unchanged except for the following two equations:

$$-\frac{\sqrt{2}}{6I_y} \left[-3(M_{Ayl0} - M_{Dyl0})L_\alpha + (M_{Ayl1} - M_{Dyl1})L_\alpha^2 \right] - \frac{N_A + N_D}{S} \frac{\alpha}{\sqrt{\alpha^2 + 2}} = 0 \quad (5-106)$$

$$\begin{aligned} & -\frac{\sqrt{2}}{12I_z} \left[-3(M_{Azl0} + M_{Czl0})L_\alpha + (M_{Azl1} + M_{Czl1})L_\alpha^2 \right] \\ & + \frac{\sqrt{2}}{12I_y} \left[-3(M_{Ayl0} + M_{Cyl0})L_\alpha + (M_{Ayl1} + M_{Cyl1})L_\alpha^2 \right] \frac{\alpha}{\sqrt{\alpha^2 + 2}} - \frac{N_A + N_C}{S} \frac{1}{\sqrt{\alpha^2 + 2}} = 0 \end{aligned}$$

(5-107)

5.5 Finite element modeling by using beam theory

The finite element method taking into consideration the tension/compression, bending and torsion without shearing effect has been used. Therefore, the stiffness matrix contains three kinds of stiffness: tension/compression, bending and torsion. A beam consisting of point i and j has 12 general displacement variables $u_i, v_i, w_i, \theta_{ix}, \theta_{iy}, \theta_{iz}, u_j, v_j, w_j, \theta_{jx}, \theta_{jy}, \theta_{jz}$ accordingly in the beam (local) coordinate system.

5.5.1 Stiffness matrix of a beam in the local coordinate system

For the uniaxial tension or compression of a beam, by using $f = Ku$, the unidimensional stiffness is:

$$K = \frac{ES}{L} \quad (5-108)$$

For the bending with an ellipse section, the bending is dissociated into $\vec{t}_{\alpha 1}$ and $\vec{t}_{\alpha 2}$ direction, the stiffness matrix for bending about the Z-direction ($\vec{t}_{\alpha 2}$ -direction) is:

$$[Z] = \begin{bmatrix} Z_{11} & Z_{12} & Z_{13} & Z_{14} \\ Z_{21} & Z_{22} & Z_{23} & Z_{24} \\ Z_{31} & Z_{32} & Z_{33} & Z_{34} \\ Z_{41} & Z_{42} & Z_{43} & Z_{44} \end{bmatrix} = \frac{EI_Z}{L^3} \begin{bmatrix} 12 & 6L & -12 & 6L \\ & 4L^2 & -6L & 2L^2 \\ & & 12 & -6L \\ \text{sym} & & & 4L^2 \end{bmatrix} \quad (5-109)$$

The bending deformation about the Y-direction is from x to z, the rotation is clockwise. Similar as the stiffness matrix $[Z]$, the stiffness matrix for bending about the Y-direction can be expressed as:

$$[Y] = \begin{bmatrix} Y_{11} & Y_{12} & Y_{13} & Y_{14} \\ Y_{21} & Y_{22} & Y_{23} & Y_{24} \\ Y_{31} & Y_{32} & Y_{33} & Y_{34} \\ Y_{41} & Y_{42} & Y_{43} & Y_{44} \end{bmatrix} = \frac{EI_Y}{L^3} \begin{bmatrix} 12 & -6L & -12 & -6L \\ & 4L^2 & 6L & 2L^2 \\ & & 12 & 6L \\ \text{sym} & & & 4L^2 \end{bmatrix} \quad (5-110)$$

For the torsion with $M = T\theta$, the unidimensional stiffness is:

$$T = GI_o / L \quad (5-111)$$

The global elemental element displacement-force matrix Eq. is therefore obtained from Eqs. (5-108-5-111) and has the expression as follows:

the global stiffness matrix is found as follows:

$$[K]_g = [R_c][K]_l[R_c]^T \quad (5-115)$$

1) Upper bounds of the effective elastic modulus E_{eff} of an $m \times n$ structure

In order to study the upper bounds of the effective elastic modulus that is a function of m and n for the $m \times n$ structure, without loss of generality, it is supposed that the number of rows m is constant, and the number of columns n varies from 1 to infinite. And each couple (m, n) gives an effective elastic modulus. The upper bound of the effective elastic modulus can be given by using the infinite number of cells ($n \rightarrow \infty$). And for the whole structure without fixing m , the upper bound can be found by using the infinite number of cells in rows and columns ($m \rightarrow \infty; n \rightarrow \infty$).

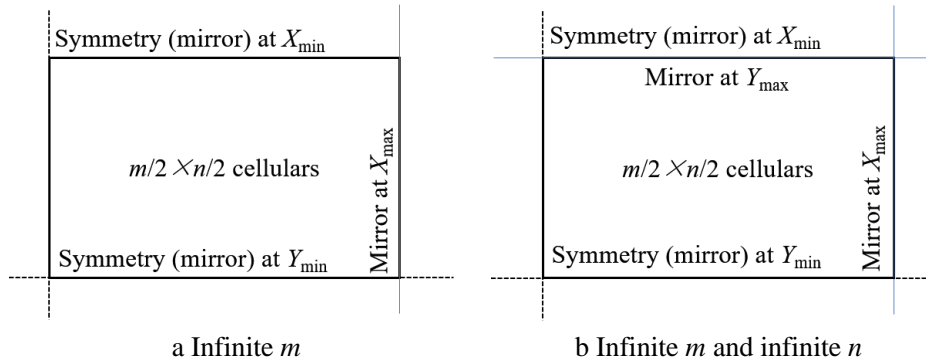


Fig. 5.5 Mirror settings for infinite numbers of cells

In the $m \times n$ structure, any two vertical parallel mirrors placed in the X - or the Y -direction will give an infinite number of cells in the direction that is perpendicular to the parallel mirrors. For example, as shown in Fig. 5.5a the symmetric plane (mirror) at X_{\min} and the mirror at X_{\max} will give an infinite number of cells in the X -direction and it doesn't depend on the values of n . That is, any value of n will give the same value of the effective elastic modulus. As shown in Fig. 5.5b, two pairs of vertical mirrors in the X - and the Y -directions will give an infinite number of cells in both directions.

2) Boundary conditions for infinite n structure

In general, the choice of m or n is fixed is the same methodology. It is supposed that m is constant. For any constant m of $m \times n$ structure, $n \rightarrow \infty$ gives the upper bound of effective elastic stiffness. In finite element method, $n \rightarrow \infty$ is ensured by the boundary conditions by using a

mirror at X_{max} . As any value of n with the mirror at X_{max} . gives the infinite assumption, $n=1$ is chosen.

For any point on the symmetrical plane (mirror) at X_{min} , the displacement boundary conditions are:

$$U_i = 0; \theta_{iy} = \theta_{iz} = 0 \quad (5-116)$$

As all the points on the mirror at X_{max} move conjointly in the X -direction, point i is chosen as the reference point, and the displacement boundary conditions for the points on this mirror are:

$$U_j = U_i (i \neq j); \theta_{jy} = \theta_{jz} = 0 \quad (5-117)$$

where the displacement u_i or the reference point is unknown. As the mirror at X_{max} is not a free border of the structure, a supplementary force equilibrium boundary condition will be used:

$$\sum F_{ix} = 0 \quad (5-118)$$

where i denotes all the nodes on the mirror at X_{max} .

For the boundary conditions for infinite m and infinite n structure, in addition to the boundary conditions in the X -direction, the boundary conditions in the Y -direction will be adopted by using the same method.

3) Stiffness matrix, displacement vector and force vector modification

The global stiffness matrix $[K]_g$ is singular. It becomes nonsingular by modifying it according to the boundary conditions. The global stiffness matrix and the displacement vector in the matrix Eq. $[K]_g \{U\} = \{F\}$ will be modified at the same time. This matrix Eq. is regarded as N_{equ} normal Eqs. where $N_{equ} \times N_{equ}$ is the dimension of the stiffness matrix. Initially, the force vector $\{F\}$ is set as $\vec{0}$ and the modification is executed in the following order:

- a) For a constant displacement boundary condition $U_q = C$

This boundary condition concerns the points on the symmetric plane and the points on at X_{max} . The coefficients in the q^{th} Eq. are rewritten:

$$K_{qr} = \begin{cases} 1(q = r) \\ 0(q \neq r) \end{cases} \quad (5-119A)$$

For the case $C \neq 0$, the following coefficients in the q^{th} Eq. are modified:

$$F_q = C \quad (5-119B)$$

In order to use the sparse matrix resolution method, more coefficients may be modified. Other directions denoted as r of the concerned points in which $K_{rq} \neq 0$ is used and F_q is modified as:

$$F_q \rightarrow F_q - \sum K_{rq} U_q \quad (5-119C)$$

and then K_{rq} is reset as zero.

$$K_{rq} = 0 \quad (5-119D)$$

b) For a conjoint movement boundary condition $U_j = U_i$

This boundary condition concerns the points on the mirror at xmax. In this case $U_j - U_i$ is used as the new unknown variable at the place of U_j .

In the kth equation ($k \neq j$), originally it is:

$$\sum_{A \neq i; A \neq j} K_{kA} U_A + K_{ki} U_i + K_{kj} U_j = F_k \quad (5-120)$$

In order to use $U_j - U_i$ as the new unknown variable the above equation is rewritten as follows:

$$\sum_{A \neq i; A \neq j} K_{kA} U_A + (K_{ki} + K_{kj}) U_i + K_{kj} (U_j - U_i) = F_k \quad (5-121)$$

For those Eqs. in which $K_{kj} \neq 0$, K_{ki} is rewritten as:

$$K_{ki} \rightarrow K_{ki} + K_{kj} \quad (5-122)$$

and in the j^{th} equation,

$$K_{jl} = \begin{cases} 1(j=l) \\ 0(j \neq l) \end{cases} \quad (5-123)$$

c) For the supplementary force equilibrium boundary condition

This boundary condition concerns the X-direction of all the points on the mirror at Xmax. In the ith equation, the force equilibrium boundary condition in Eq. (5-118) is used. The X-direction of a concerned point is denoted as k, and the Y-direction of the concerned points is denoted as l, the coefficients K_{il} are modified as follows:

$$K_{il} \rightarrow \sum K_{kl} \quad (5-124)$$

After the resolution of the modified matrix equation, U_j is reset as U_i at the place of $U_j - U_i$.

4) Effective elastic modulus under compression with border constraint

The problem of compression with border constraint has only constant displacement boundary condition. A normal solution of FE will give the effective elastic modulus under compression. The stiffness matrix is modified by using Eqs. (5-119A) to (5-119D) with the imposed constant displacement boundary conditions in order to dispose of its singularity.

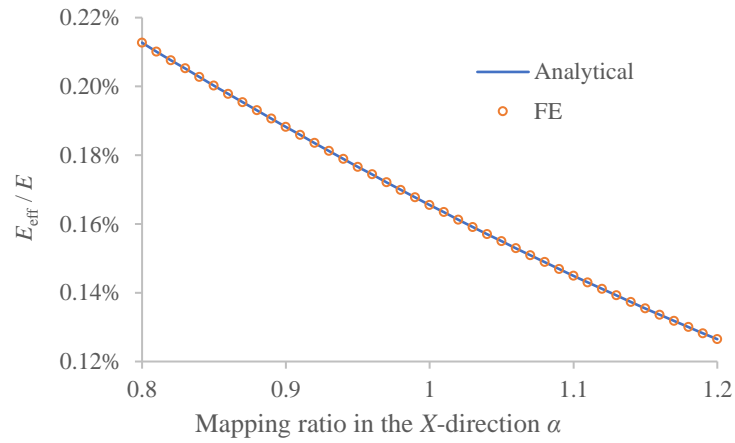
5.6 Results and discussion

The relative effective compressive elastic modulus and Poisson's ratio related to the mapping ratio in the X -direction α will mainly be presented and analyzed, as well as those related to the number of cells m and n for variable values of α . The analytical results are firstly compared to results obtained with the finite element (FE) method developed in our previous work¹⁸⁴, then some experimental results are used for comparison.

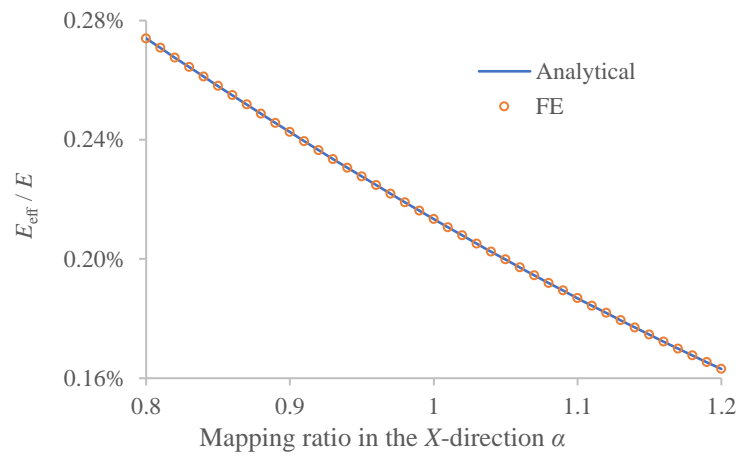
We consider a rhombic dodecahedron structure under compression in the Z -direction with the following geometrical parameters: $b = 5$ mm; $d = 0.5$ mm. The strut material is supposed as elastic and isotropic with $E = 110$ GPa and $\nu = 0.3$. The range of mapping ratio in the X -direction α is supposed between 0.8 and 1.2. For the given geometrical parameters, the porosity of the structure remains the same and is $\phi = 0.89$.

Fig. 5.6 shows the results of the lower and upper bounds of the relative compressive effective elastic modulus related to the mapping ratio in the X -direction α for the structure without border constraint.

The lower bound is given by the structure of the 1×1 cell while the upper bound is given by $\infty \times \infty$, without border constraint in both cases. As shown in Fig. 5.6, the upper and lower bounds given by the analytical method are identical to those given by the FE method as both methods are based on the same beam theory. It is found that both the lower and upper bounds decrease when the mapping ratio in the X -direction α increase.



a



b

Fig. 5.6 Relative compressive effective elastic modulus without border constraint: (a) Upper bound, (b) Lower bound.

Fig. 5.7 shows the results of the lower and upper bounds of the relative compressive effective elastic modulus related to the mapping ratio in the X-direction α for the structure with border constraint. It is observed that this curve decreases when the mapping ratio increases as those curves of the lower and upper bounds obtained in Fig 5.6. However, the values of the relative effective compressive elastic modulus with border constraint is higher than the upper bound without border constraint.

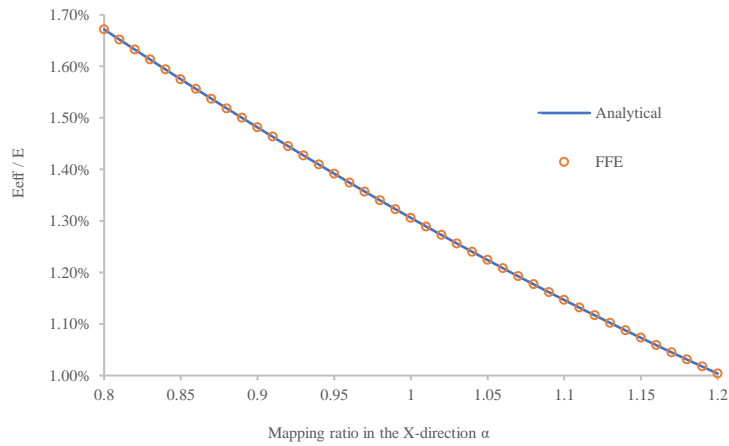


Fig. 5.7 Relative compressive effective elastic modulus with border constraint.

In Fig. 5.8, the Poisson's ratio ν_{zx} and ν_{zy} related to the mapping ratio in the X -direction α for the structures of 1×1 and $\infty \times \infty$ cells without border constraint are presented.

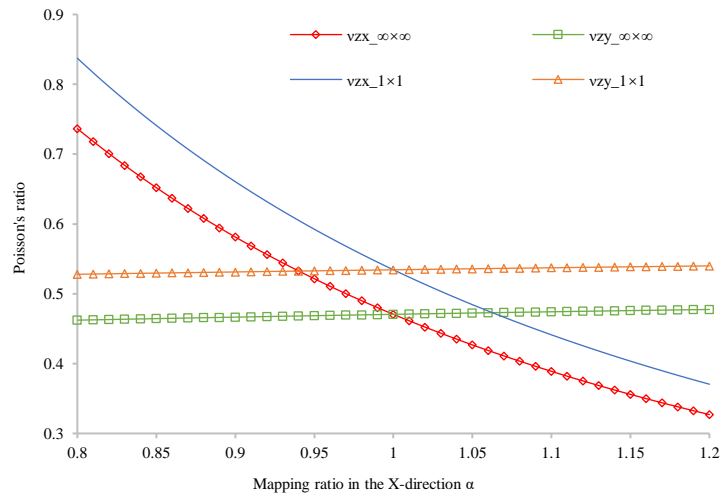


Fig. 5.8. Poisson's ratio without border constraint.

For both cases, the Poisson's ratio ν_{zx} decreases significantly when the mapping ratio α increases while ν_{zy} increases lightly. Poisson's ratio ν_{zy} remains stable because there is no mapping in the Y -direction. It is also observed that with any value of α , the value of ν_{zx} of 1×1 is higher than that of $\infty \times \infty$, because the horizontal displacement in the X -direction in the case $\infty \times \infty$ is less than that in the case of 1×1 , due to the uniform and averaged deformation in the infinite case. The same observation is found for ν_{zy} .

The Poisson's ratio ν_{zx} and ν_{zy} related to the mapping ratio in the X -direction α with border constraint remains 0 as there is no horizontal displacement and will not be presented graphically here.

The elastic properties can be presented for a structure having $m \times n$ cells with a certain value

of α too, such as $\alpha=1$ to study the influence of the cells as discussed in our previous study.

The effective elastic modulus for $\alpha=1$ without border constraint is presented in Fig. 5.9. It is observed that with a certain number of cells m , the relative effective compressive elastic modulus increases and tends to an upper bound when $n \rightarrow \infty$. The results are based on the FE method due to its powerful calculation capacity. When the cells of m or n increase, the effective elastic modulus tends to a limit value. Therefore, the homogenization of such a structure needs several cells in both the X and Y directions. The homogenization based on small number of cells is not reliable.

When handling the mapped structures without boundary constraints in the same way, the calculation and statistical analysis of the effective elastic modulus with respect to the number of cells were performed for $\alpha=0.7$ and $\alpha=0.5$. These results were shown in Fig. 5.10 and Fig. 5.11. The variation trend was found to be the same as when $\alpha=1$.

For the diamond-like dodecahedron in practical applications, the assumption is usually made that the volumes of the homogenous blocks are equal. This means that the outer framework dimensions of the same lattice structure are the same, while the number of unit cells increases with a decrease in the mapping ratio. The number of unit cells for $\alpha=0.5$ is twice that of $\alpha=1$. For the same number of cells, the effective elastic modulus increases with a decrease in the mapping ratio. Additionally, the effective elastic modulus increases with an increase in the number of cells. In other words, for samples with the same volume, the one with a smaller mapping ratio has a higher elastic modulus.

When n is held constant at 40, the variation of the equivalent elastic modulus with the mapping ratio is explored as m increases from 1 to 40. The results are presented in Fig. 5.12. Previous discussions have already established that the equivalent elastic modulus increases monotonically with the number of cells. For structures with the same number of cells, the equivalent elastic modulus decreases monotonically with the mapping ratio in a nonlinearly increasing manner. A smaller value of α corresponds to a slower rate of increase in elastic modulus.

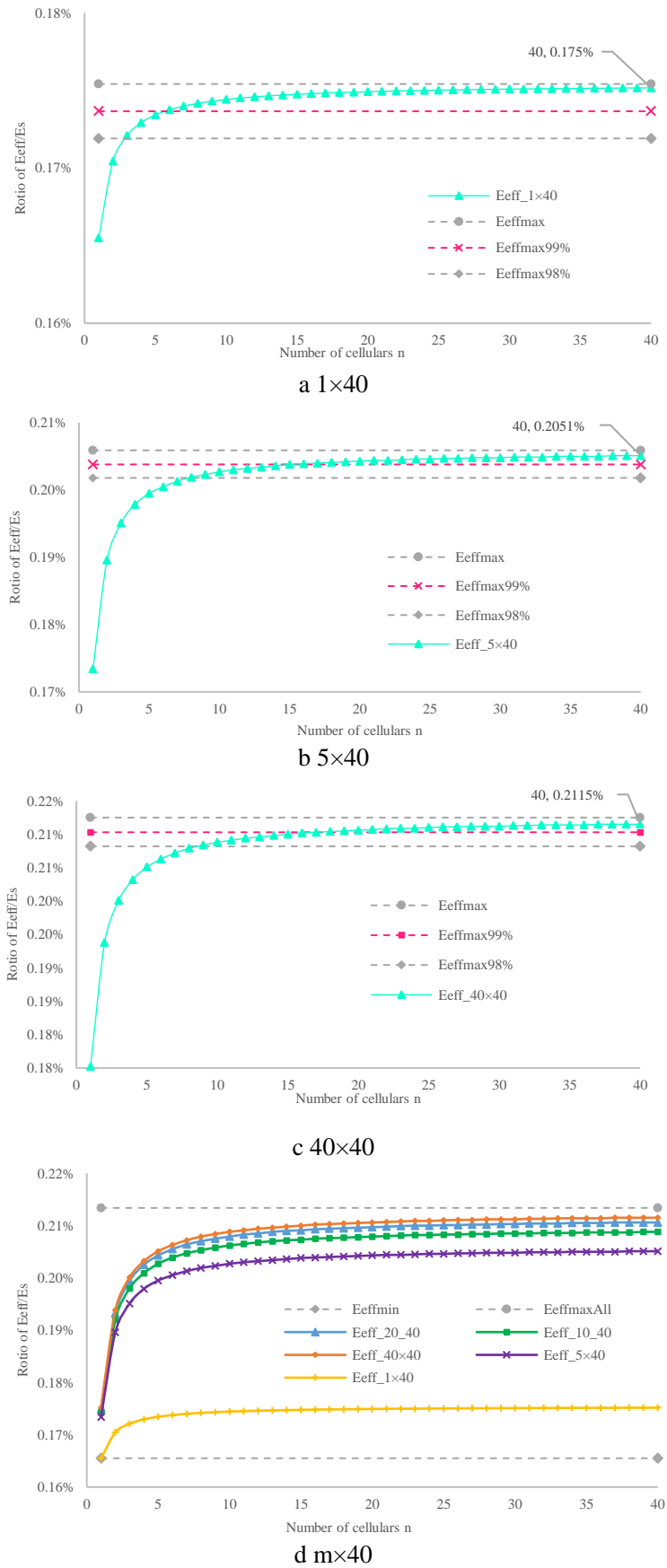


Fig. 5.9. Effective elastic modulus for $\alpha=1$ of different structures without border constraints

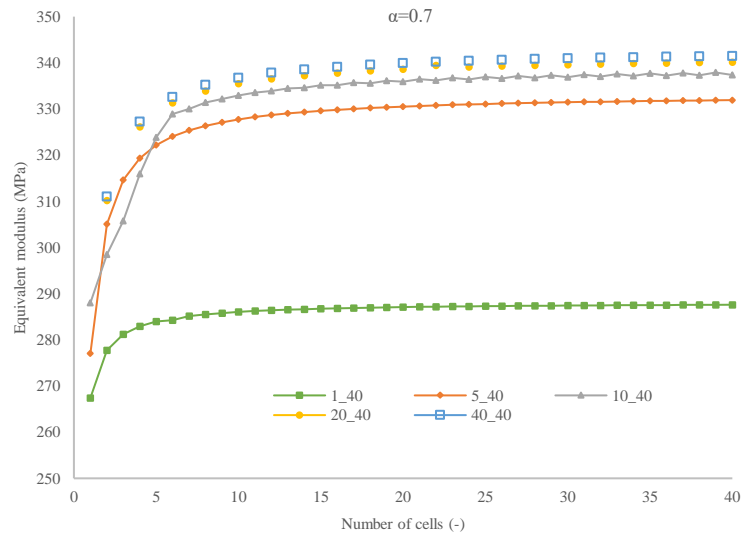


Fig. 5.10. Effective elastic modulus for $\alpha=0.7$ of different structures without border constraints

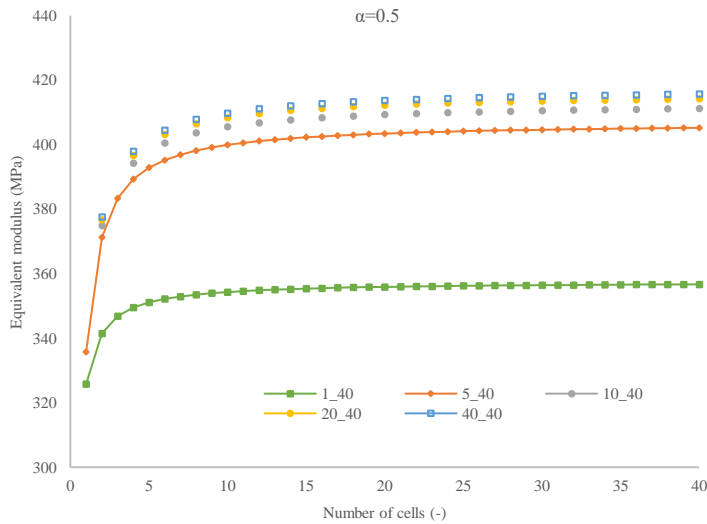


Fig. 5.11 Effective elastic modulus for $\alpha=0.5$ of different structures without border constraints

Other models often express the equivalent elastic modulus as a function of porosity. Similarly, our analytical model also presents the influence of strut size on porosity and equivalent elastic modulus in Fig. 5.13. Firstly, the elastic modulus exhibits a nonlinear increasing trend with strut diameter, and the thicker the strut, the faster the rate of modulus growth. Intuitively, the effect of mapping ratio on elastic modulus, as observed in Fig. 5.12, remains consistent. During the monotonically decreasing mapping ratio, the growth rate of modulus decreases. Furthermore, the porosity continues to decrease with increasing strut diameter, and the rate of change of porosity also increases.

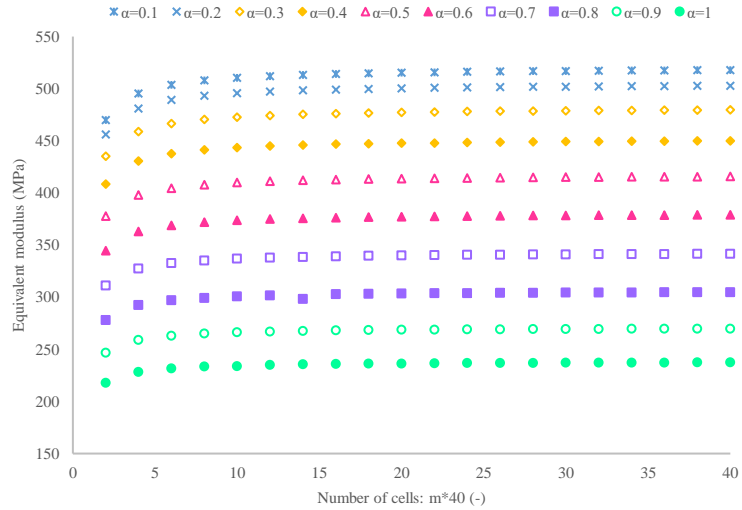


Fig. 5.12 The influence of the number of unit cells and the mapped ratio on the effective elastic modulus of a homogeneous block.

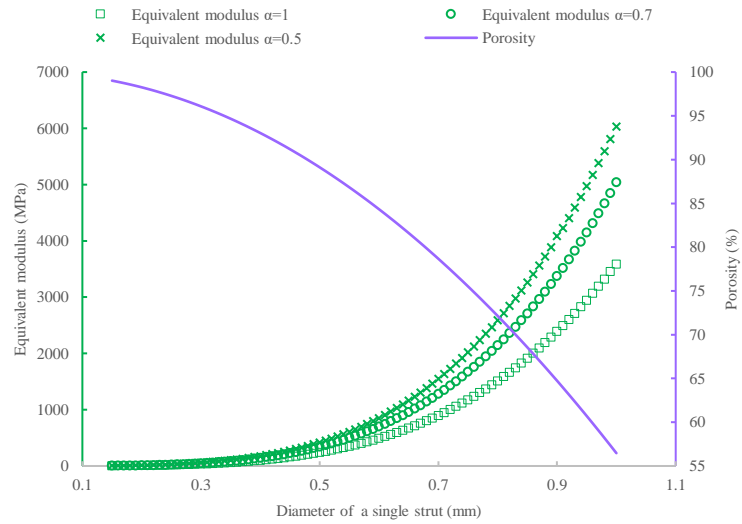


Fig. 5.13 Effect of strut diameter on equivalent elastic modulus and porosity.

In Fig. 5.14, the curves of the Poisson's ratio ν_{zx} and ν_{zy} are presented for $\alpha=1$ without border constraint. Theoretically, all the curves tend to a constant value when $n \rightarrow \infty$ that coincides with the upper bound of the effective Poisson's ratio. It is observed that when the number of cells n is small (<5), the curve's tendency is not stabilized due to the border effects of the structure. This shows again that the homogenization of the structure cannot be based on a small value of m or n .

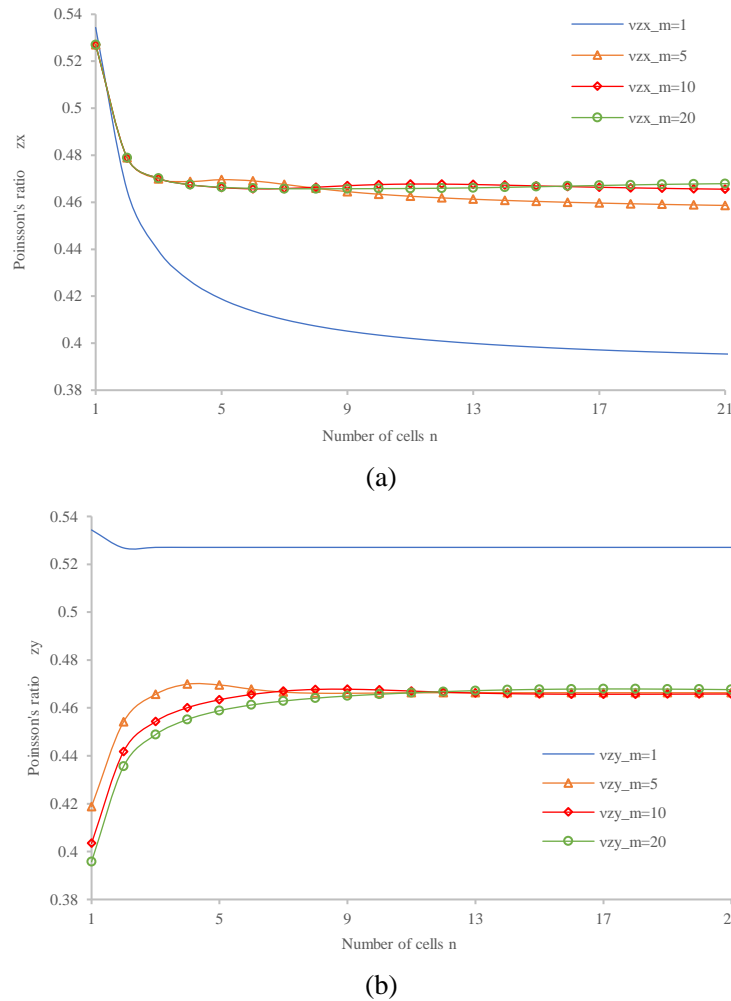


Fig. 5.14 Poisson's ratio for $\alpha=1$ without border constraint: (a) Poisson's ratio v_{zx} ,
(b) Poisson's ratio v_{zy} .

To validate the prediction model, tests corresponding to the appropriate conditions were conducted and the results of the relative compressive effective elastic modulus, with different mapping ratios in the X-direction α , are shown in Fig. 5.15. When $\alpha=1$, the highest actual printed diameter of the strut exceeds the design value by 26%. The numerical results underestimate the experimental ones. According to the statistical analysis, the maximum errors between the actual testing and calculated values for three different mapping ratios are 3.9%, 6.5%, and 6.2%, respectively. It has been determined that for Electron Beam Melting (EBM), the minimum required part diameter should be greater than 0.15 mm. When $\alpha=0.5$ and the design diameter is calculated as $d=0.5$, the length of the minor axis of the elliptical cross-section of the strut is close to the lower limit of the required accuracy. However, due to the sagging effect during material melting, the actual dimensions of the struts are often significantly larger than the design values. This discrepancy leads to prediction errors in the equivalent elastic modulus.

At smaller scales, it is not advisable to choose a very small mapping ratio for the components. At larger scales, the influence of surface quality is greatly reduced, and the effects of geometric deformation are much smaller compared to the effects of fabrication precision. Theoretically, reducing the mapping ratio to a certain extent can significantly improve the stiffness and strength of lattice structures.

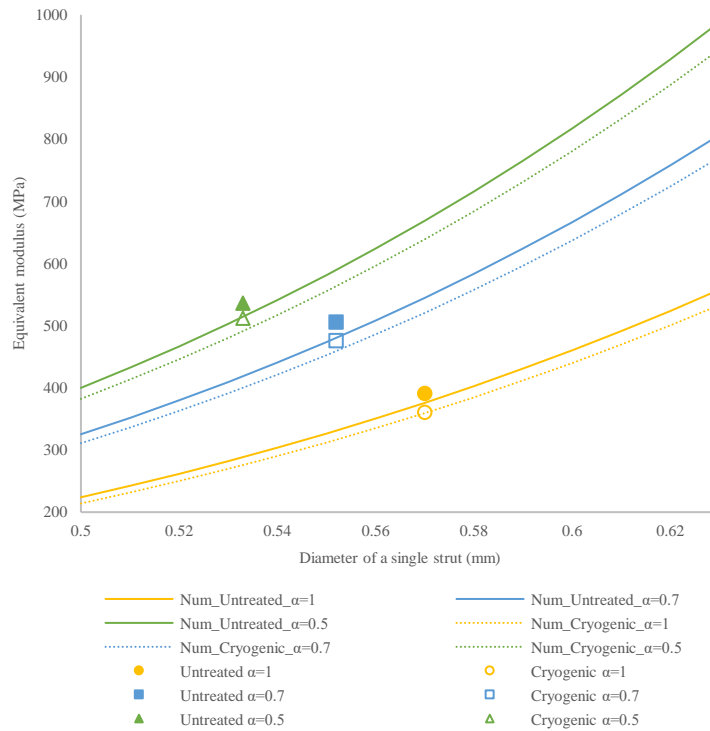


Fig. 5.15. Comparison of experimental and analytical results.

To validate the applicability of the analytical model, a comparison is made with the elastic modulus of Ti6Al4V diamond-shaped dodecahedron structures reported in other studies. The standard rhombic dodecahedron equivalent modulus of elasticity has also been summarized in some literature^{185,186}, and the tested relative density on the relative modulus are compared with the analytical prediction model under the corresponding conditions shown in Fig. 5.16. Although process parameters and dimensional errors at small scales can affect the modulus, the trend in the equivalent elastic modulus predicted by the model, using the relative density as a reference, can still be observed in the graph to be consistent with the test results provided in the literature. However, no suitable test results have been reported for the effective modulus of elasticity of uniaxial mapped models with equal porosity. Certainly, although the analytical model is

specifically designed for components composed of diamond-shaped dodecahedron, it can be applied to various metal materials as well. This is because the primary inputs to the model are the unit cell dimensions, as well as the elastic modulus and Poisson's ratio of the base material. Therefore, in theory, the trend prediction of the elastic modulus can be conducted for different alloy types based on their material properties.

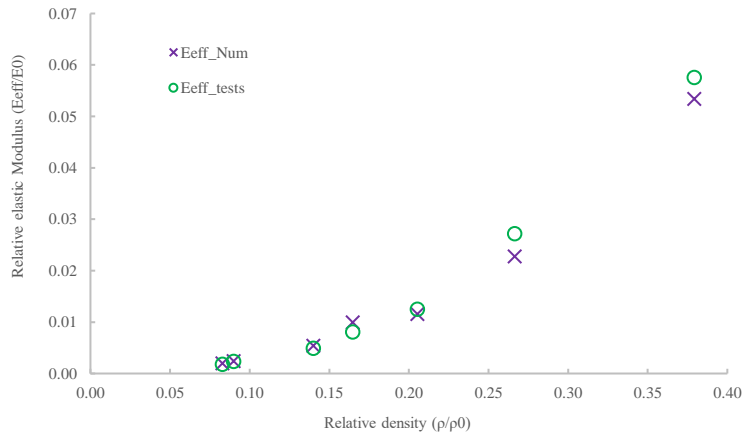


Fig. 5.16 Analytical results compared with data of elastic modulus provided in literatures.

5.7 Summary

In this chapter, an analytical and a finite element model for the estimation of the effective compressive elastic modulus and Poisson's ratios of mapped cellular rhombic dodecahedron structures fabricated in Ti6Al4V using the electron beam melting (EBM) process, with and without border constraints. Mathematically, the coordinates of a point in the strut are mapped with the mapping function $x \rightarrow \alpha x$. In this mapping operation, the porosity of the structure remains unchanged but the section and position of the struts change. The compressive effective elastic modulus and Poisson's ratios has been investigated in different cases. It was found that both the lower and upper bounds of compressive effective elastic modulus decrease when the mapping ratio in the X-direction α increase, and the diameter of the struts decrease. The Poisson's ratio ν_{zx} decreases significantly when the mapping ratio α increases while ν_{zy} increases lightly. By comparing the equivalent elastic moduli of diamond-shaped dodecahedron from different studies, it has been observed that the analytical model can to some extent effectively predict the elastic modulus. Furthermore, by considering the equivalent stresses based on the cell for diamond-shaped dodecahedron specimens with different cross-sectional shapes, the model can accurately reflect the effective elastic modulus of a homogeneous body and its variation

trend within a certain range of precision.

The method will help to have a better understanding of the mechanical properties of mapped cellular rhombic dodecahedron structures. Besides, the method of introducing the mapping parameter into the original lattice structure provides a new possibility for the design of three-dimensional lattice configuration with variable mechanical properties.

Chapter 6 Prediction of high-cycle fatigue

In the previous experimental section, compression tests under high-cycle fatigue were conducted on rhombic dodecahedron specimens of $5 \times 5 \times 5$ with different mapping ratios ($\alpha = 1, 0.7, \text{ and } 0.5$). The cyclic S-N curve of the specimens was plotted as the cyclic equivalent-stress monotonically increased. Taking the specimens as the equivalent homogeneous body for the rhombic dodecahedron, other specimens of different sizes or shapes will be normalized based on the equivalent stress for comparison purposes.

The numerical simulation of lattice structures is based on the compression process simulation of rhombic dodecahedron. Within the range of elastic deformation, as the compression load monotonically increases, the load in the compression direction (Z-axis) and the deformation exhibits a linear trend. The cyclic process of high-cycle fatigue can be approximated as a loading-unloading process within the elastic range, especially in the early stages of fatigue. In this fatigue study, the stress amplitude is determined based on the cyclic compression load, which determines the equivalent stress on the uniform cross-section of the square block specimen. Depending on the different compression loads, the upper and lower limits of cyclic loads can be determined at a stress ratio (R) of 0.1, thus determining the cyclic stress amplitude. After determining the stress amplitude, the Z-axis compression deformation at this equivalent stress is determined using the analytical method mentioned earlier. This method allows for the combination of different cyclic conditions under $R=0.1$ at various equivalent stresses.

Subsequently, in the fatigue simulation, the Basquin's law (equation 2-9) and the Soderberg average stress correction formula (equation 2-10), along with the consideration of surface roughness coefficients, are used to approximate the material's fatigue life. In the numerical simulation, both solid elements and Euler-Bernoulli beam elements are employed for comparison. The simulation results are then validated against actual block fatigue test data. It should be noted that controlling the precise cyclic stress amplitude in the simulation is challenging due to the difficulty in accurately adjusting the step size. Therefore, there may be a maximum error of up to 4% for each load group. The main objective is to use the visualization capability of the numerical simulation to identify the location of fatigue failure.

6.1 Simulation of first fatigue fracture on the single strut in multi-cells

In the numerical simulations with solid elements and beam elements shown in Fig. 6.1a and Fig. 6.1b, the maximum local stress occurs at the joint near the central region of the outermost edge of the porous structure. For the mapped structure, under the same cyclic load, the bending deformation of the support decreases with the increase of the mapping ratio, and the local stress of the joint at the unmapped direction and the lower surface boundary is greater than that at the mapped one. In the subsequent fatigue numerical simulation, as shown in Fig. 6.1c, it is verified that the joints at the same position have the shortest life, and the strut with the maximum stress is the first to experience fatigue fracture. Considering the excessively high computational cost of solid elements, and after confirming the consistency of the stress distribution trend, all subsequent simulations are conducted using beam elements.

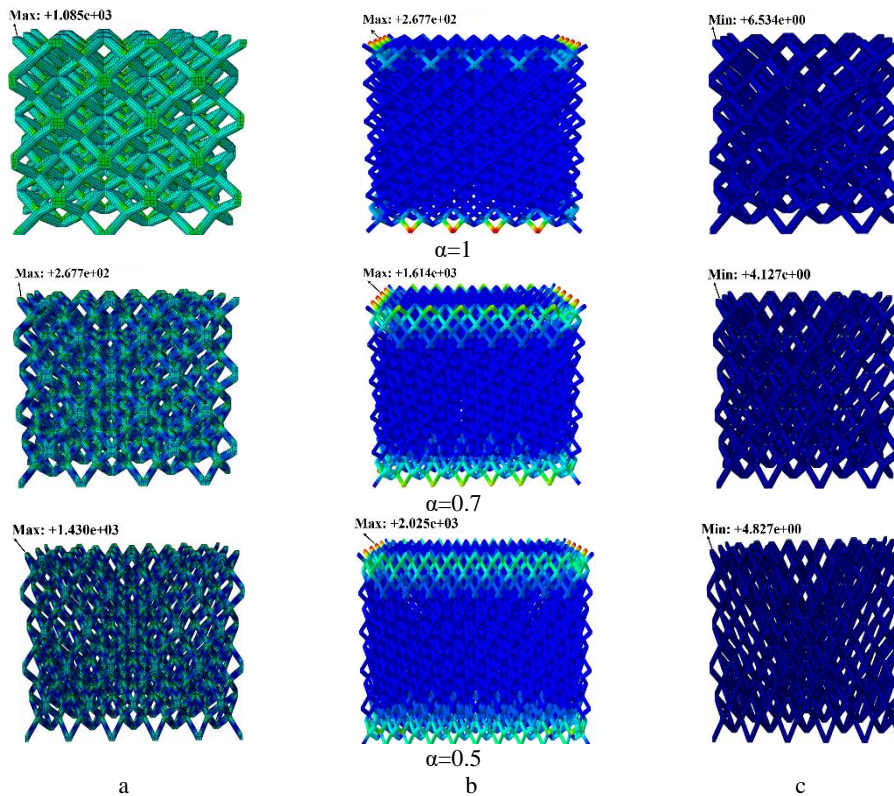


Fig. 6.1 The local maximum stress of each mapping ratio strut in fatigue simulation with solid elements a and beam elements b; The corresponding high cycle fatigue life on the same strut c

Fatigue failure of samples with different mapping ratios are shown in Fig. 6.2. In the outermost center of the upper surface or lower surface in the non-mapped direction, a small aggregate composed of a few support struts first falls off the structure due to stress concentration.

The predicted phenomena are consistent with the results of the numerical simulation. There is no support between the struts after the lateral propagation of the joint failure crack leads to the overall failure of the outermost boundary. The severe extrusion effect of the inward bending of the upper and lower surfaces during the continuous compression process caused the stress concentration in the stress center, and the main crack propagated obliquely along the cell at about 45° . The study has found that the 45° extrusion band generated by material failure usually appears after the fatigue strain curve reaches a certain threshold, before which the strain rate is almost constant¹⁸¹.

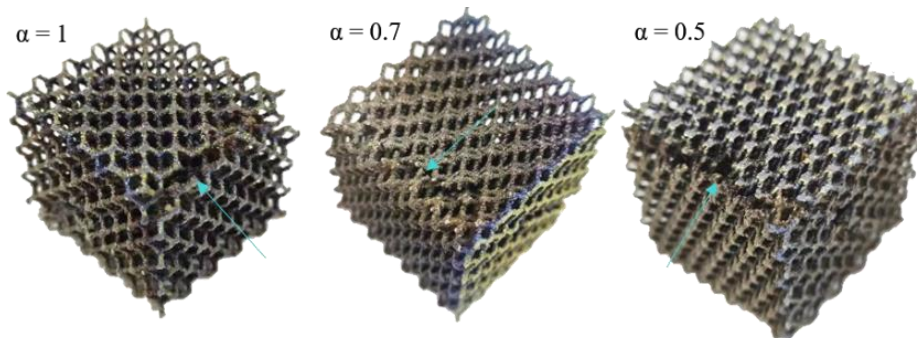


Fig. 6.2 The outer edge of a fracture in a fatigue test

The compressive performance of lattice materials is influenced by their equivalent elastic modulus, which exhibits a non-linear increasing trend with a monotonically increasing number of unit cells. To investigate the sensitivity of the fatigue performance of rhombic dodecahedron structures to changes in the number of unit cells, beam elements were used for numerical simulation as shown in Fig. 6.3, and cell numbers were 5×5 , 10×10 , 20×20 , 40×40 and 100×100 , respectively. By analyzing the stress distribution, it can be found that the maximum local stress is also in the center of the outer boundary without any change in post-treatment means or mapping ratio. It is important to note that free boundaries have a significant impact on the mechanical properties of open lattice structures. As demonstrated in Chapter 3, when the boundary conditions fully constrain the unit cells on all sides, creating a closed lattice structure, the elastic modulus reaches its relative maximum. In this case, the forces experienced at all nodes have symmetric counterparts with the same force patterns, making it possible to ignore the influence of the number of unit cells and boundary effects on the mechanical properties of the lattice material.

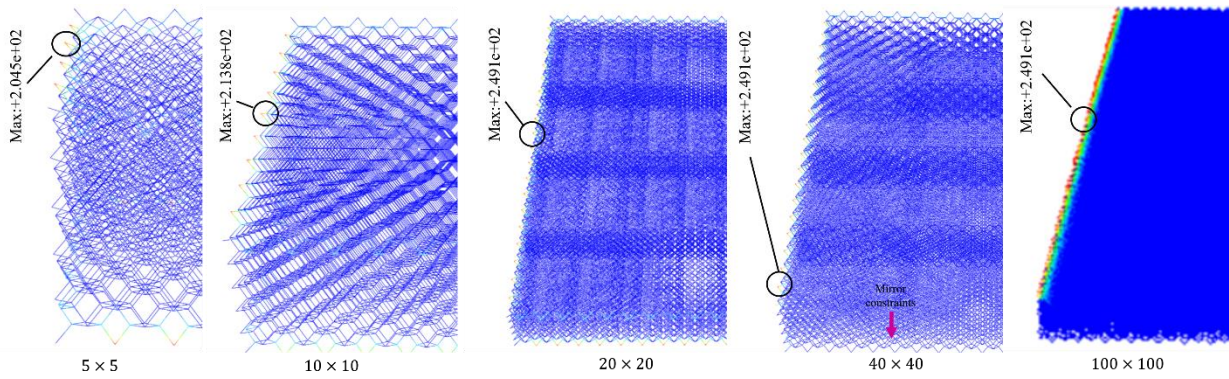


Fig. 6.3 Numerical simulation of the maximum stress of struts in the compression of beam elements with cell number growth

As shown in Fig. 6.4, the relation between the number of arrayed unit-cell and fatigue life is consistent with the change of equivalent elastic modulus¹⁵⁸. The equivalent uniform mechanical performance of the homogeneous block was related to a tendency of first steepening and then slowing in the monotonically increasing process of the number of cells in the two-dimensional array. Same to the equivalent elastic modulus, the growth rate is negligible when the cells exceed 100×100 . High-cycle compression-compression fatigue was numerically simulated for cells with varying numbers. The number of cells has minimal impact on the fatigue life of the first fracture strut. The maximum fatigue limit of 100×100 cells is less than 3% higher than that of 5×5 cells. Indeed, selecting an equivalent model with a homogeneous body of size 5×5 can help save the cost of preparing repetitive fatigue test samples. However, in an ideal scenario, it would be preferable to choose a larger size such as 100×100 or, as demonstrated in Chapter 3, a sample size of 40×40 with minimal variation in the elastic modulus.

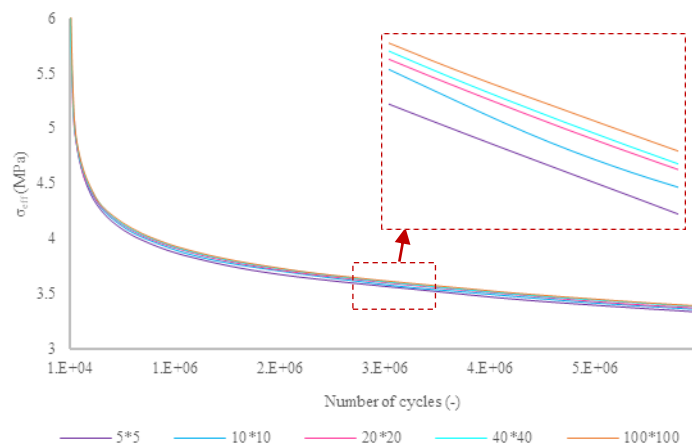


Fig. 6.4 High cycle fatigue S-N curve of simulated beam element with cell number increasing

It should be noted that the calculated fatigue life up to now is the life of the strut corresponding to the fracture at the maximum local stress on the strut. But the real life of a homogeneous structure is much longer than that. The first time a strut breaks in a fatigue test, it cannot be detected by the equipment, much less seen by the human eye. Consequently, under the direction of the ratchet model, homogeneous block fatigue continues to be anticipated.

6.2 Analytical calculation of local maximum stress

As mentioned in Chapter 1, studying the fatigue life of unit cells using the approach of local maximum stress is reasonable and feasible. Moreover, the feasibility of numerical simulations is based on the relationship between local maximum stress and the number of cycles. However, performing finite element numerical analysis with varying stress amplitudes can be cumbersome and inefficient. Even if the beam element is used for numerical simulation, it is still not convenient for the diversified design requirements, and it can only meet the calculation of the life of the strut. There is much monitoring work for the simulation and prediction of the overall cell collapse. The main problem is to calculate the maximum local stress of the strut by the analytical method instead of a complex numerical simulation. Combining the calculation of local maximum stress with the variation of strut cross-sectional properties based on the bending deformation theory of beam elements in solid mechanics is an approach to consider. This allows for the calculation of stress distribution and deformation in the lattice structure by taking into account the changes in strut cross-sectional properties with respect to the mapping ratio. By utilizing the principles of beam element theory, the local maximum stress can be evaluated, providing insights into the mechanical behavior of the lattice structure.

The geometrical relations of the strut OA are demonstrated in Eq. (4-8). And the length of a mapped strut (beam) is a function of the mapping ratio α and the length L of a normal unit shown in Eq. (4-9).

After the mapping in the X -direction, the beam's direction is a function of the mapping ratio α . The section is perpendicular to $\vec{n}_{A\alpha}$ and its shape is an ellipse. The projection of this ellipse on the plane YOZ is also an ellipse. These two ellipses share the same long axis (when $\alpha \leq 1$) or the same short axis (when $\alpha \geq 1$): an axis with the same direction and length. Hereafter $\alpha \leq 1$ is assumed without losing the generality.

Combining equations (4-10) to (4-13), for the convenience of the calculation required be-

fore and after the mapping, a local coordinate system of the mapped beam will be established. The long axis direction is used as the first coordinate direction of the mapped beam. A local coordinates system for the mapped beam $O\alpha$ is established in Eq. (4-15) and (4-16). And a point on the border of the section is given in Eq. (4-21).

Therefore, the forces on a node in the local coordinate system are calculated as:

$$\begin{Bmatrix} M_t \\ M_{f_1} \\ M_{f_2} \end{Bmatrix} = [R]^T \begin{Bmatrix} M_x \\ M_y \\ M_z \end{Bmatrix} \quad (6-1)$$

Then the normal stress on the beam section is as follows:

$$\sigma = \frac{N}{S} + \frac{M_{f_1}}{I_{G1}} z - \frac{M_{f_2}}{I_{G2}} y = \frac{N}{S} + \frac{M_{f_1}}{I_{G1}} q \sin \theta - \frac{M_{f_2}}{I_{G2}} p \cos \theta \quad (6-2)$$

$$\text{where } y = r \cos \theta = p \cos \theta; \quad z = r \frac{\sqrt{3}\alpha}{\sqrt{\alpha^2 + 2}} \sin \theta = q \sin \theta$$

$$\frac{d\sigma}{d\theta} = \frac{M_{f_1}}{I_{G1}} q \cos \theta + \frac{M_{f_2}}{I_{G2}} p \sin \theta = 0 \Rightarrow \begin{cases} \cos \theta = \pm \frac{M_{f_2} I_{G1} p}{\sqrt{M_{f_1}^2 I_{G2}^2 q^2 + M_{f_2}^2 I_{G1}^2 p^2}} \\ \sin \theta = \mp \frac{M_{f_1} I_{G2} q}{\sqrt{M_{f_1}^2 I_{G2}^2 q^2 + M_{f_2}^2 I_{G1}^2 p^2}} \end{cases} \quad (6-3)$$

Finally, the local maximum stress is as follows:

$$\sigma_{\max} = \frac{N}{S} \pm \frac{I_{G2}}{I_{G1}} \left(\frac{M_{f_1}^2 q^2}{\sqrt{M_{f_1}^2 I_{G2}^2 q^2 + M_{f_2}^2 I_{G1}^2 p^2}} + \frac{I_{G1}}{I_{G2}} \frac{M_{f_2}^2 p^2}{\sqrt{M_{f_1}^2 I_{G1}^2 p^2 + M_{f_2}^2 I_{G1}^2 p^2}} \right) \quad (6-4)$$

The commercial finite element solver Abaqus was used to simulate the compression process of the cells, and Fe-safe software was used for the subsequent fatigue calculation with the Basquin's law and the mean stress correction model.

By combining Eqs. (2-9) and (2-10), a single strut's life (N_{fs}) is expressed in Eq. (6-5):

$$N_{fs} = \left(\frac{\sigma_f}{a} \right)^{\frac{1}{b}} = \left[\frac{(\sigma_{\max} - \sigma_{\min}) \cdot K_t}{2a \cdot \left(1 - \frac{\sigma_m}{\sigma_{ut}} \right)} \right]^{\frac{1}{b}} \quad (6-5)$$

Based on Eq. (6-5), the first failure lifetime of the strut and the maximum equivalent cyclic load holds:

$$N_{fS} = \left(\frac{\sigma_f}{a} \right)^{\frac{1}{b}} = \left[\frac{(\sigma_{\max}^* - \sigma_{\min}^*) \cdot K_t}{2a \cdot \left(1 - \frac{\sigma_m^*}{\sigma_{ut}^*} \right)} \right]^{\frac{1}{b}} = \left[\frac{\sigma_{\max}^* (1-R) \cdot K_t}{2a \cdot \left(1 - \frac{\sigma_{\max}^* (1+R)}{2\sigma_{ut}^*} \right)} \right]^{\frac{1}{b}} = \left[\frac{(1-R) \cdot K_t}{2a \frac{1}{\sigma_{\max}^*} - \frac{(1+R)}{2\sigma_{ut}^*}} \right]^{\frac{1}{b}} \quad (6-6)$$

The maximum principal stress computed by the FEM Abaqus software under compressive-compressive load conditions was compared to the life derived from the fatigue life Eq. (6-6). The results are given in Fig. 6.5. The variation of local maximum stress with equivalent stress is linear, while the fatigue life of struts exhibits a non-linear decreasing trend with monotonically increasing equivalent stress. The analytical solutions closely approximate the results obtained from numerical simulations.

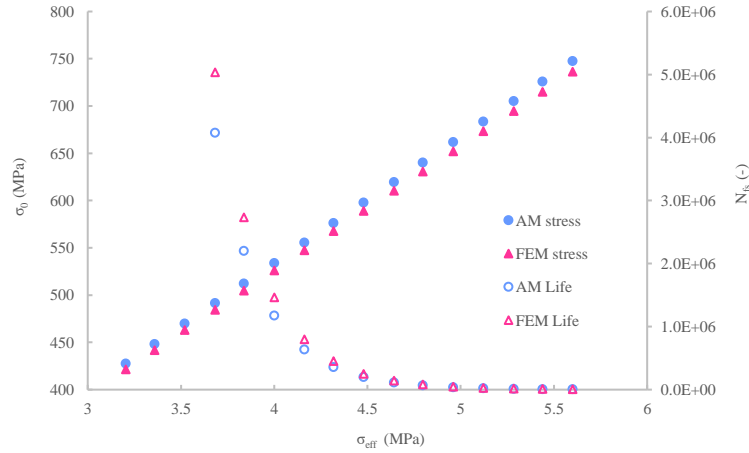


Fig. 6.5 The equivalent stress of the homogeneous block and the maximum stress of the strut and the corresponding fatigue life

By maintaining the same porosity and varying the mapping ratio α , it was observed that reducing α resulted in the elliptical cross-section of the struts becoming too small to meet the minimum accuracy requirements of EBM manufacturing. To address this, the scale was increased, setting the length b of the homogenous cell body to 10 mm, and the diameter of the struts was adjusted to 2 mm, resulting in a calculated porosity of 56.47%. With α set to 0.1, the short axis of the elliptical cross-section of the struts approached 0.2 mm, precisely meeting the minimum size requirement of 0.15 mm for EBM technology.

Under a cyclic load of 1000N, the curve of local maximum stress varying monotonically with the mapping ratio was obtained using analytical solutions and plotted in Fig. 6.6. It was observed that as the mapping ratio α decreased below 0.2, the local stress rapidly increased,

making it difficult to meet the actual requirements of the component. Additionally, when α approached 0.1, the local stress exceeded the material's yield limit, resulting in the complete failure and fracture of the strut experiencing the maximum stress within one cycle.

Based on these findings, a mapping ratio of $\alpha=0.5$ was considered appropriate in the design, as it not only significantly improved the mechanical performance but also reduced the likelihood of fatigue failure. After the failure of the first strut, the remaining struts, which were more numerous in structures with smaller mapping ratios due to the same block size, continued to provide support, reducing the cyclic load impact caused by the ratchet effect.

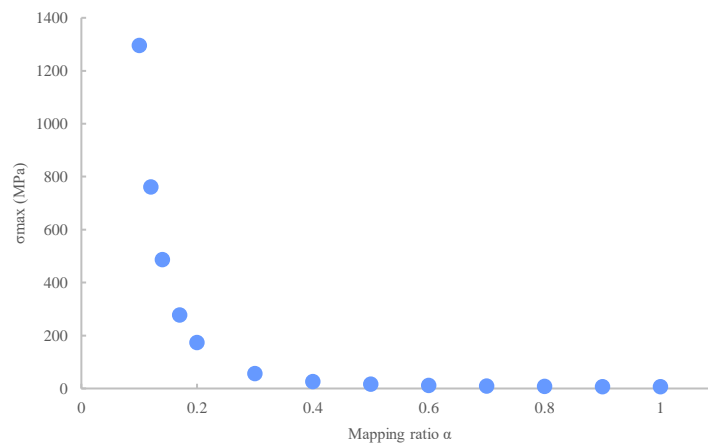


Fig. 6.6 The variation of local maximum stress with mapping ratio

6.3 Fatigue life of multi-cells under preset load limit

Previous research data did not allow for accurate predictions of the relationship between cyclical damage and fatigue life. However, periodic ratcheting and fatigue cracks were found, and the dominant failure mode was the ratcheting effect¹⁴⁶. Indeed, the failure of the first strut occurs in the region where strain accumulates slowly along the strain curve. Under the action of cyclic loading, the fractured strut experiences inward compression, leading to an accelerated growth of strain accumulation. Once the turning point is reached, rapid failure occurs. This phenomenon can be attributed to the primary influence of the ratchet effect.

Eqs. (2-13) has been used extensively to calculate the ratcheting effect of porous materials, including rhombic dodecahedron^{128,130}. However, this homogenization of the model based on the structure of the regular plate cannot precisely re-establish the deformation state of the rhombic dodecahedron in terms of geometric precision. Determination of the stress concentration generated during strut deformation is difficult. Therefore, in combination with the earlier

work and the above equations, the ratcheting model belonging to the rhombic dodecahedron is proposed. It can not only represent the maximum local strain on the strut but also clarify the relationship between the fracture of the strut and the failure of the homogeneous block.

Fig. 6.7 integrates the relation between the maximum cyclic load and the accumulation of deformation in the compression direction when the cycle reaches the preset limit in the high-cycle fatigue test. The compression deformation and cyclic load of cells fatigue failure and ratchet effect accumulation may follow a linear relationship, as expressed in Eqs. (6-7A). The deformation of untreated samples and cryogenically treated samples exhibits a similar linear slope, thus allowing for normalization. With cryogenic treatment, the material undergoes grain refinement, resulting in an increased number of grain boundaries and a decrease in creep resistance. Under the same cyclic loading, the accumulated deformation increases, but greater damping is also generated. The accumulation of plastic strain varies with different post-treatment methods. Taking the plastic properties of the untreated material as a reference, the accumulated deformation is expected to decrease or increase during the transition from ductile to brittle behavior in the material. The accumulated deformation of the bulk sample in the fatigue test shows a certain degree of linear trend. When the mapping ratio decreases, the angle between the strut and the compression direction becomes smaller, and the deformation mode of the strut gradually shifts from bending-dominated to buckling-dominated. Therefore, under the same load, the compression deformation is reduced. When the number of bulk cells changes, the system can withstand multiple times the load under the same deformation. Therefore, it is necessary to use the equivalent stress as a reference and convert the system's compression load with changed cell count to the equivalent load in this test, as described in Eqs. (6-7B).

Eqs. (6-8) represents the relationship between the total accumulated plastic strain and the maximum cyclic load of the fatigue test system. The microstructure of the materials modified by cryogenic treatment differs in macroscopic mechanical properties. The deformation intensity before and after post-treatment is the slope K_d of the linear relation, and K_d is the same for the samples under the same treatment conditions. After cryogenic treatment, the plastic properties of the samples were significantly improved, showing that they were more sensitive to the ratchet effect, and more deformation accumulated under the same load, so K_d increased slightly. The coefficients are given in Table 6.1.

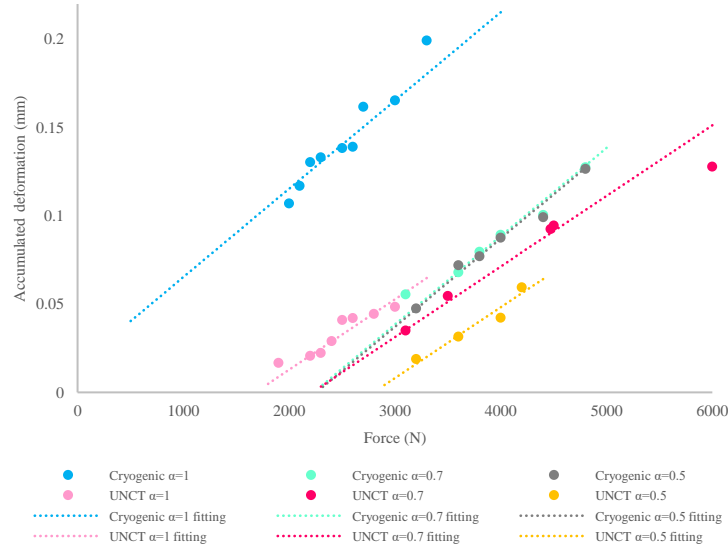


Fig. 6.7. Maximum cyclic load and accumulation of deformation in the compression direction

$$d_{pl} = K_d \cdot P_{\max} + C_{pl} \quad (6-7A)$$

$$d_{pl} = K_d \cdot P_{\max}^{Multi} \cdot \frac{S_{area}^{as-built}}{S_{area}^{Multi}} + C_{pl} \quad (6-7B)$$

Where d_{pl} is the accumulated total deformation in the fatigue test, P_{\max} is the maximum cyclic load, $S_{area}^{as-built}$ is the surface area of the square upper surface of the rhombic dodecahedron framework, S_{area}^{Multi} is the surface area of the framework with multiple cells after the change in cell count, and K_d and C_{pl} are constants.

$$\varepsilon_y = \frac{d_{pl}}{b_{asbuilt}} = \frac{K_d \cdot P_{\max} + C_{pl}}{b_{asbuilt}} \quad (6-8)$$

Based on Eqs. (2-13), (6-4), (6-7) and (6-8), the fatigue life at the load limit of the homogeneous block and the life of the strut that fails first holds:

$$N_{fH} = \frac{2^m \cdot (K_d \cdot P_{\max} + C_{pl})}{Kb_{asbuilt} \cdot [P_{\max} (1-R)]^m \left[\frac{(1-R) \cdot K_t}{2a \cdot N_{fS}^b} + \frac{(1+R)}{2\sigma_{ut}} \right]^n} \quad (6-9)$$

The selected strut range was from the design value of 0.5 mm to the SEM image calibration average value of 0.68 mm. Fig. 6.8. shows the changes in the equivalent density and predicted equivalent elastic modulus of the unprocessed samples with different mapping ratios α . The equivalent density of a homogeneous body with a diameter calibrated by SEM is almost twice the design value, which causes significant errors in the mechanical property analysis of the structure. The difference in the strut diameter causes a change in cell porosity, which is not only

reflected in the equivalent elastic modulus but also has a significant influence on the local stress of the strut under compression-compression cycles, which directly affects the fatigue life. Owing to the constant porosity of all samples, the diameter of the strut had only one unique value. Based on the displacement of the system that reaches the upper and lower limits of the cyclic load during the initial stage of the fatigue test, the deformation obtained by the analytical method under the same load condition is determined to be in the best agreement with the analytical and test results when $R=0.63$ mm, as presented in Fig. 6.9.

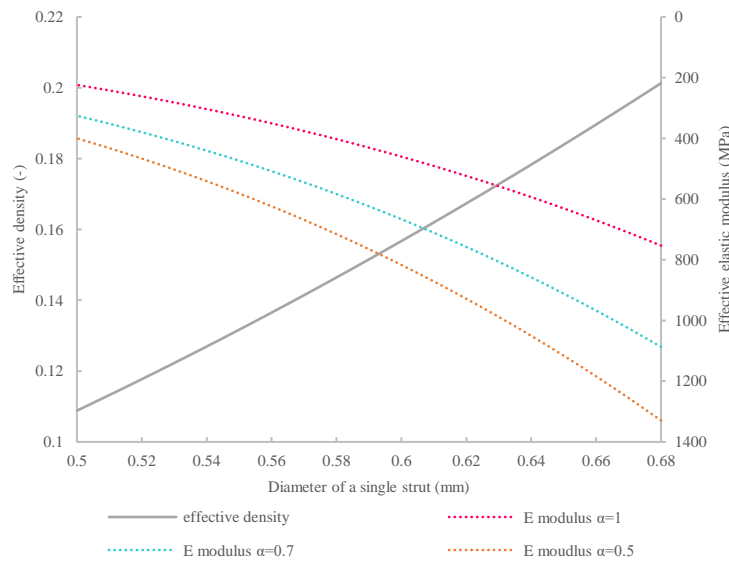


Fig. 6.8. Equivalent density and predicted equivalent elastic modulus of unprocessed samples with different mapping ratios α .

Table 6.1 Constants of the relationship between the maximum pressure and accumulated deformation

	Untreated			Cryogenic			
	α	1	0.7	0.5	1	0.7	0.5
K_d			4E-5			5E-5	
C_{pl}		-0.06723	-0.08871	-0.11186	0.0153	-0.11151	-0.11282

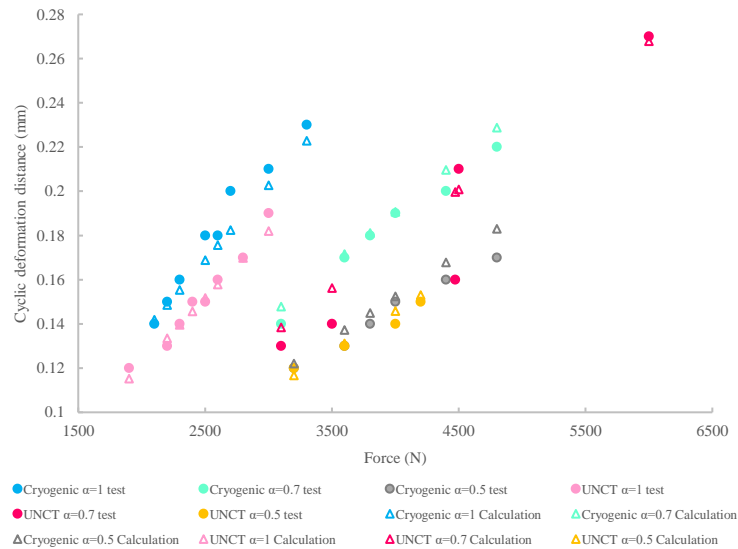


Fig. 6.9. Cyclic deformation calculated by the analytical method and measured by the fatigue testing machine

When $d=0.63$ mm, the cross-sectional properties of the elliptical cylindrical strut are listed in Table 6.2. The fatigue life of the strut and homogeneous block of the three mapping ratios before and after cryogenic treatment were predicted, and the calculated S-N curves are shown in Fig. 6.10. The range of strut diameters from 0.5 mm to 0.68 mm is plotted in the figure as a translucent area, with peak pressure errors of 10% to 15% for the same number of cycles. The fatigue life of the same-volume sample increased with a decreasing in mapping ratio. When $\alpha=1$, the angle between adjacent struts was too large to provide excellent bending performance. When $\alpha=0.5$ and $\alpha=0.7$, the fatigue behavior of the homogeneous block was similar, which is consistent with the variation trend of the equivalent elastic modulus with the mapping ratio in previous studies. As the mapping ratio of the porous structure decreased, the corresponding increase in cycles was nonlinear, but instead exhibited initial rapid growth and gradual convergence. The variation in the material constants was almost exclusively related to the local maximum stress of the strut. Compared with the mapping ratio $\alpha=1$, 0.7, and 0.5, the corresponding ratio of the constant n in this experiment was close to 1, 0.5, and 0.4. The material constants related to the high cycle fatigue life of the homogeneous block under a preset load limit are listed in Table 6.3. The fatigue lives of other mapping ratios can be obtained by interpolation or other statistical methods. Owing to the improvement in plastic properties, the sensitivity of strain accumulation in the cryogenic samples was greater, and the value of n was slightly higher than those of untreated samples. The smaller the mapping ratio, the closer the value is to the constant n . The values of the material constants may be slightly varied based on the number of

unit cells. When the number of cells increases, σ_{eff}^* is determined according to the change in S_{area} of the homogeneous structure. However, in this study, the influence of the cell height in the z-direction is more idealized. Due to geometric inhomogeneity, the compressive fatigue response to the number of layers could be more pronounced, necessitating further studies to elucidate.

Table 6.2 The cross-section properties of the elliptical cylindrical strut

α	r	$I_y A_\alpha$	$I_z A_\alpha$	$I_o A_\alpha$	I_{yz}	S_{area}	J	G_U	G_C
1		0.0077	0.0077	0.0155		0.3117	0.0155		
0.7	0.315	0.0007	0.0020	0.0026	0	0.2395	0.0094	41241.54	39414.15
0.5		0.0010	0.0030	0.0040		0.1800	0.0060		

Table 6.3 Constants of the N_{FH} model

	Untreated	Cryogenic	Untreated	Cryogenic	Untreated	Cryogenic
α		1		0.7		0.5
K				4E-15		
n	1.54	1.76	0.735	0.78	0.58	0.69
m				12.5		

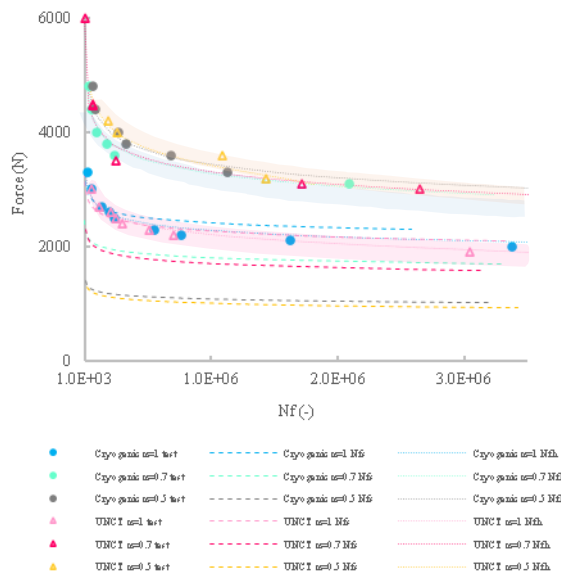


Fig. 6.10 $S-N$ curves of struts and homogeneous blocks with different mapping ratios

The prediction of the fatigue life of the rhombic dodecahedron's homogenous block varies depending on the criteria used to determine the life. Further validation is needed to determine if the predictive model can provide guidance for fatigue failure of this type of component. Fig. 6.11 shows the curves of the number of cycles and accumulated strain obtained by Wang et al.¹⁸⁷ for the multi-cellular Ti6Al4V rhombic dodecahedron under equivalent stress amplitudes of 2 MPa and 3.8 MPa. The same material parameters and processing methods were used for

validation under the same equivalent stress amplitude. Although the definition of life in the experiments differs from our model, the predicted model suggests that the point of rapid strain accumulation is approximately reached when the life is attained. According to the studies of other researchers, the cellular structure will collapse rapidly after reaching the inflection point of the strain curve. The error between the predicted life and the life at the inflection point is approximately 10.3% for a cyclic stress of 2 MPa, and roughly 16.67% for a cyclic stress of 3.8 MPa. This indicates that even in the absence of complete material properties, the predictive model still provides valuable guidance for assessing the trends of stress, strain, and number of cycles under cyclic loading.

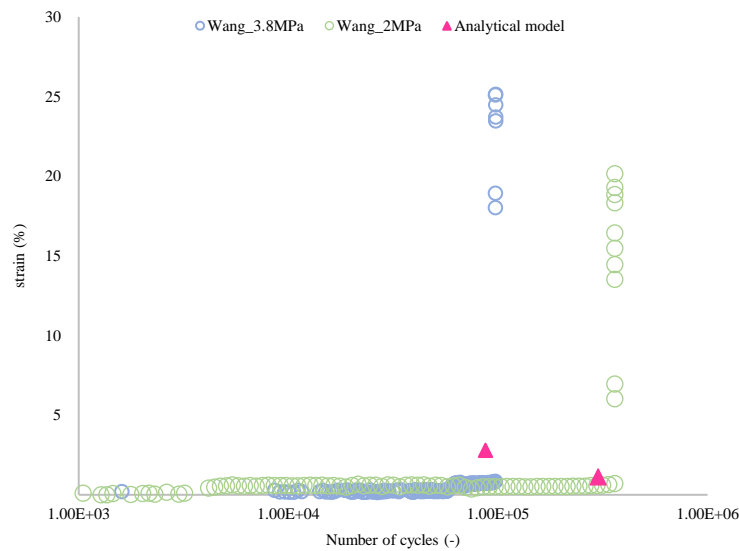


Fig. 6.11 Analytical model validation of the Strain-N curve for Ti6Al4V rhombic dodecahedron

Even when the material parameters are not identical, it is advisable to select the same additive manufacturing alloy type, such as Ti6Al4V, for comparing the compression fatigue performance of diamond-shaped dodecahedron structures. The results are presented in Fig. 6.12. Liu conducted high-cycle compression fatigue tests using diamond-shaped dodecahedron with a porosity of 91.2%⁸⁷. By using the same porosity, the design diameter of the struts can be calculated. Although there is a measurement error of approximately $\pm 11\%$ in the actual diameter, the surface roughness and material properties were chosen based on the properties used in this study, resulting in an acceptable error in the S-N curve. Additionally, Ahmadi conducted compression fatigue tests on cylindrical specimens composed of diamond-shaped dodecahedron unit cells¹⁴². The approach for selecting material parameters was consistent with the previous study.

While there are slight differences in the macroscopic compression deformation between cylindrical and square specimens, the cylindrical cross-sections were equivalent to square specimens with the same cross-sectional area for calculation during validation, resulting in some errors. However, this approach can still provide insights for fatigue prediction of diamond-shaped dodecahedron lattice structures with various common cross-sectional shapes.

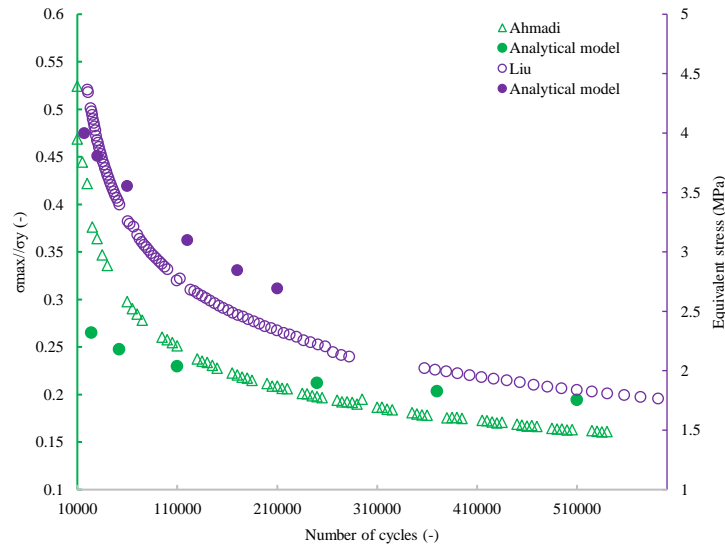


Fig. 6.12 Analytical model validation of the Stress-N curve for Ti6Al4V rhombic dodecahedron

6.4 Summary:

In this chapter, the high cycle compression-compression fatigue response of cells was studied. The maximum local stress of the strut in the compression process was solved analytically. The mean stress correction is used to predict the cycle times of the strut that first fails under high-cycle compression-compression load. Based on the cumulative plastic deformation and cycle times under ratchet effect and the effect of strut diameter on load under small scale, the relationship between the defined fatigue life and the maximum cycle load of homogeneous blocks is established, and the appropriate material constants are given under these conditions.

Under the condition of the same volume and constant porosity, the relation between the high-cycle fatigue life of the equivalent homogeneous body composed of rhomboidal dodecahedron and mapping ratio α is nonlinear. The number of cycles increased with the decrease of mapping ratio α and the increase of cell number, but the growth rate continued to decline until the upper limit. Among the three structures, the smallest mapping ratio, $\alpha=0.5$, shows the best

compressive strength and fatigue performance. Although the increase in the number of cells plays a certain role in improving the mechanical properties of homogeneous bodies, considering the cost, when the number of cells reaches 100×100 , the expression of homogenization with an infinite number of cells can be satisfied in most cases.

Comparison with high-cycle fatigue test results of Ti6Al4V diamond-shaped dodecahedron in other studies reveals that the predictive model can provide reasonably accurate predictions even when material parameters, model assumptions, or system conditions are not identical. Although there may be some discrepancies in certain regions of the S-N curve comparison, the results are significantly closer to the provided data compared to traditional formulas that are only applicable to rod failure. Instead of directly providing precise and usable predictive data, the model offers a valuable alternative by predicting the allowable fatigue life of the corresponding multicellular structures based on a certain degree of fatigue testing results. This not only saves a significant amount of experimental costs but also demonstrates the value of the model.

Chapter 7 Conclusion

This study focuses on the analysis of the lattice structure of a rhombic dodecahedron fabricated through electron beam melting for medical bone implants. Analytical and finite element models were developed to estimate the effective compressive elastic modulus and Poisson's ratios of mapped cellular rhombic dodecahedron structures, with and without border constraints. The mapping function $x \rightarrow \alpha x$ was used to map the coordinates of points in the struts, resulting in changes to the section and position of the struts while maintaining the structure's porosity. The study investigated the compressive effective elastic modulus and Poisson's ratios in various scenarios. Additionally, the study examined the high-cycle compression-compression fatigue response of the cells and established a fatigue life prediction model for equivalent homogeneous blocks. The influence of cryogenic treatment on the fatigue properties of Ti6Al4V samples was also investigated. Based on the research, the following findings and conclusions can be drawn:

1) Mechanical Properties of Ti6Al4V rhombic dodecahedron lattice structure:

The equivalent elastic modulus and high-cycle compression-compression fatigue performance of the rhombic dodecahedron lattice structure fabricated from Ti6Al4V exhibited a significant improvement as the mapping ratio α decreased monotonically. The fatigue failure mode of the unit cell involved 45° shear bands, accompanied by the detachment of strut aggregates from the surface of the specimen. The presence of unmelted metal particles on the printed surface and the overlapping of texture lines were attributed to solidification direction variations caused by printing strategies and the characteristics of the EBM technology. Fatigue failure primarily occurred at the joints where the struts were connected, with a smaller amount occurring in the center of the struts. After deep cryogenic treatment, the equivalent elastic modulus, compressive strength, and fatigue performance of specimens with the same mapping ratio showed improvement. However, an increase in accumulated strain along the compression direction was observed after fatigue failure.

2) Microstructural modification by deep cryogenic treatment:

In the microstructure of Ti6Al4V material, the presence of α -Ti clusters can be observed. These clusters are formed by the aggregation of α -Ti phase in specific directions, resulting in a

strong texture. The strength and orientation of the texture significantly influence the mechanical properties of the material. A strong texture can increase the material's strength but may reduce its ductility. After the deep cryogenic treatment process, the volume contraction of the material causes the absorption of stable V element precipitates in the β -Ti phase by the α -Ti phase, resulting in lattice distortion. Lattice distortion promotes dislocation multiplication within grains and tends to align them in the same direction. These substructures form numerous unstable subgrains, leading to the decomposition of α -Ti grain clusters, grain deflection, and weakening of the original texture. The grain refinement increases the number of grain boundaries. The refined grains and additional grain boundaries provide more slip systems, offering more options for dislocation motion, thus improving the material's plasticity and fatigue performance but simultaneously reducing its creep resistance.

3) Analytical model of Mapped Cellular Rhombic Dodecahedron Structures:

The mapping ratio α was introduced to describe the parametric equations and deformation accuracy of the mapped structure. The accuracy of the parameter equations was validated through numerical simulations. Analytical and finite element models were developed to estimate the effective compressive elastic modulus and Poisson's ratios of the mapped structures with and without border constraints. The models considered the changes in the section and position of the struts after mapping. It was found that the compressive effective elastic modulus and Poisson's ratios varied with the mapping ratio α and the diameter of the struts. The analytical model showed promising predictions of the elastic modulus. By considering the equivalent stresses based on the cell, the model accurately reflected the effective elastic modulus of a homogeneous body. The method provides insights into the mechanical properties of mapped cellular rhombic dodecahedron structures and offers possibilities for designing three-dimensional lattice configurations with variable mechanical properties.

4) Fatigue Life Prediction and Homogenization Analysis:

Analytical solutions determined the maximum local stress of struts under compression and used mean stress correction to predict cycle times under high-cycle compression-compression loads. The relationship between fatigue life and maximum cycle load of homogeneous blocks was established, considering plastic deformation, ratchet effect, and strut diameter's impact on small-scale load. Nonlinear relationship observed between high-cycle fatigue life and mapping

ratio α of equivalent homogeneous bodies composed of rhomboidal dodecahedron, with cycles increasing as α decreases and cell number increases. Smallest mapping ratio, $\alpha=0.5$, showed best compressive strength and fatigue performance among three structures. Model provided reasonably accurate predictions compared to other studies on Ti6Al4V rhombic dodecahedron, accounting for varying material parameters, assumptions, and system conditions. Alternative approach predicted fatigue life of multicellular structures based on fatigue testing results, saving costs and demonstrating value.

Overall, the research presented in this study successfully employed analytical and computational models to analyze the mechanical properties, microstructure, and performance of Ti6Al4V base material and mapped cellular rhombic dodecahedron structures. These models offer valuable insights for understanding and predicting the behavior of these materials and structures.

Chapitre 7 Conclusion

Cette étude se concentre sur l'analyse de la structure en treillis d'un dodécaèdre rhombique fabriqué par fusion de faisceau d'électrons pour des implants osseux médicaux. Des modèles analytiques et par éléments finis ont été développés pour estimer le module d'élasticité compressive effectif et les coefficients de Poisson des structures en dodécaèdre rhombique cellulaire, avec ou sans contraintes aux frontières. La fonction de mappage $x \rightarrow \alpha x$ a été utilisée pour mapper les coordonnées des points dans les entretoises, entraînant des changements de section et de position des entretoises tout en maintenant la porosité de la structure. L'étude a examiné le module d'élasticité compressive effectif et les coefficients de Poisson dans différents scénarios. De plus, l'étude a examiné la réponse à la fatigue compression-compression à cycles élevés des cellules et a établi un modèle de prédiction de durée de vie en fatigue pour des blocs homogènes équivalents. L'influence du traitement cryogénique sur les propriétés de fatigue des échantillons de Ti6Al4V a également été étudiée. Sur la base des recherches effectuées, les conclusions et résultats suivants peuvent être tirés :

1) Propriétés mécaniques de la structure en treillis du dodécaèdre rhombique en Ti6Al4V :

Le module d'élasticité équivalent et les performances en compression-compression à cycles élevés de la structure en treillis du dodécaèdre rhombique fabriquée à partir de Ti6Al4V ont montré une amélioration significative lorsque le rapport de mappage α diminuait de manière monotone. Le mode de défaillance en fatigue de la cellule unitaire impliquait des bandes de cisaillement à 45° , accompagnées du détachement des agrégats d'entretoises de la surface de l'échantillon. La présence de particules métalliques non fondues à la surface imprimée et le chevauchement des lignes de texture étaient attribués aux variations de la direction de solidification causées par les stratégies d'impression et les caractéristiques de la technologie EBM. La défaillance en fatigue se produisait principalement au niveau des joints où les entretoises étaient connectées, avec une quantité moindre au centre des entretoises. Après un traitement cryogénique profond, le module d'élasticité équivalent, la résistance à la compression et les performances en fatigue des échantillons avec le même rapport de mappage ont montré une amélioration. Cependant, une augmentation de la déformation accumulée le long de la direction de compression a été observée après la défaillance en fatigue.

2) Modification microstructurale par traitement cryogénique profond:

Dans la microstructure du matériau Ti6Al4V, on peut observer la présence de grappes d' α -Ti. Ces grappes sont formées par l'agrégation de grains de phase α -Ti dans des directions spécifiques, ce qui entraîne une texture forte. La résistance et l'orientation de la texture influencent significativement les propriétés mécaniques du matériau. Une texture forte peut augmenter la résistance du matériau mais peut réduire sa ductilité. Après le processus de traitement cryogénique profond, la contraction volumique du matériau provoque l'absorption de précipités d'éléments V stables dans la phase β -Ti par la phase α -Ti, ce qui entraîne une distorsion de la structure cristalline. La distorsion de la structure cristalline favorise la multiplication des dislocations à l'intérieur des grains et tend à les aligner dans la même direction. Ces sous-structures forment de nombreux sous-grains instables, conduisant à la décomposition des grappes de grains d' α -Ti, à la déviation des grains et à l'affaiblissement de la texture d'origine. L'affinement des grains augmente le nombre de joints de grains. Les grains raffinés et les joints de grains supplémentaires fournissent plus de systèmes de glissement, offrant ainsi davantage d'options de déplacement des dislocations, ce qui améliore la plasticité et les performances en fatigue du matériau, mais réduit simultanément sa résistance au fluage.

3) Analyse des structures cellulaires rhombiques dodécaèdres mappées:

Le rapport de mappage α a été introduit pour décrire les équations paramétriques et la précision de déformation de la structure mappée. La précision des équations paramétriques a été validée par des simulations numériques. Des modèles analytiques et par éléments finis ont été développés pour estimer le module d'élasticité en compression effectif et les coefficients de Poisson des structures mappées avec et sans contraintes aux frontières. Les modèles ont pris en compte les changements de section et de position des entretoises après le mappage. Il a été constaté que le module d'élasticité en compression effectif et les coefficients de Poisson variaient avec le rapport de mappage α et le diamètre des entretoises. Le modèle analytique a montré des prédictions prometteuses du module d'élasticité. En considérant les contraintes équivalentes basées sur la cellule, le modèle a reflété avec précision le module d'élasticité effectif d'un corps homogène. Cette méthode fournit des informations sur les propriétés mécaniques des structures cellulaires rhombiques dodécaèdres mappées et offre des possibilités pour la conception de configurations de treillis tridimensionnels avec des propriétés mécaniques variables.

4) Prédiction de la durée de vie en fatigue et analyse d'homogénéisation:

Des solutions analytiques ont permis de déterminer la contrainte maximale locale des entretoises sous compression et d'utiliser une correction de la contrainte moyenne pour prédire les cycles sous des charges de compression-compression à haute fréquence. La relation entre la durée de vie en fatigue et la charge maximale de cycle des blocs homogènes a été établie en tenant compte de la déformation plastique, de l'effet de cliquet et de l'impact du diamètre des entretoises sur la charge à petite échelle. Une relation non linéaire a été observée entre la durée de vie en fatigue à haute fréquence et le rapport de mappage α des corps homogènes équivalents composés de rhombes dodécaédriques, les cycles augmentant à mesure que α diminue et que le nombre de cellules augmente. Le plus petit rapport de mappage, $\alpha = 0,5$, a montré la meilleure résistance à la compression et les meilleures performances en fatigue parmi les trois structures. Le modèle a fourni des prédictions raisonnablement précises par rapport à d'autres études sur les rhombes dodécaédriques de Ti6Al4V, en tenant compte des paramètres matériaux variables, des hypothèses et des conditions du système. Une approche alternative a prédit la durée de vie en fatigue des structures multicellulaires sur la base des résultats des essais de fatigue, ce qui permet d'économiser des coûts et démontre sa valeur. Dans l'ensemble, la recherche présentée dans cette étude a utilisé avec succès des modèles analytiques et computationnels pour analyser les propriétés mécaniques, la microstructure et les performances du matériau de base Ti6Al4V et des structures cellulaires cartographiées en dodécaèdre rhombique. Ces modèles offrent des informations précieuses pour comprendre et prédire le comportement de ces matériaux et structures.

References

- [1] Zhao N., Parthasarathy M., Patil S., et al. Direct additive manufacturing of metal parts for automotive applications. *Journal of Manufacturing Systems* **2023**, *68*, 368-375. DOI: <https://doi.org/10.1016/j.jmsy.2023.04.008>
- [2] Anaz Khan M. Latheef A. Metal additive manufacturing of alloy structures in architecture: A review on achievements and challenges. *Materials Today: Proceedings* **2017**. DOI: <https://doi.org/10.1016/j.matpr.2023.05.192>
- [3] Rodriguez-Montano, O. L. Cortes-Rodriguez, C. J. Uva A. E. F., et al. Comparison of the mechanobiological performance of bone tissue scaffolds based on different unit cell geometries. *J Mech Behav Biomed Mater* **2018**, *83*, 28-45. DOI: <https://doi.org/10.1016/j.jmbbm.2018.04.008>
- [4] Wang S., Zhou X., Liu L., et al. On the design and properties of porous femoral stems with adjustable stiffness gradient. *Med Eng Phys* **2020**, *81*, 30-38. DOI: <https://doi.org/10.1016/j.medengphy.2020.05.003>
- [5] Yavari S. A., Wauthle R., van der Stok J., et al. Fatigue behavior of porous biomaterials manufactured using selective laser melting. *Mater Sci Eng C Mater Biol Appl* **2013**, *33* (8), 4849-4858. DOI: <https://doi.org/10.1016/j.msec.2013.08.006>
- [6] Zhao S., Li S. J., Wang S. G., et al. Compressive and fatigue behavior of functionally graded Ti-6Al-4V meshes fabricated by electron beam melting. *Acta Materialia* **2018**, *150*, 1-15. DOI: <https://doi.org/10.1016/j.actamat.2018.02.060>
- [7] Klippstein H., Hassanin H., Diaz De Cerio Sanchez A., et al. Additive Manufacturing of Porous Structures for Unmanned Aerial Vehicles Applications. *Advanced Engineering Materials* **2018**, *20* (9), 1800290. DOI: <https://doi.org/10.1002/adem.201800290>
- [8] Bici M., Brischetto S., Campana F., et al. Development of a multifunctional panel for aerospace use through SLM additive manufacturing. *Procedia CIRP* **2018**, *67*, 215-220. DOI: <https://doi.org/10.1016/j.procir.2017.12.202>
- [9] Gong X., Anderson T. Chou K. Review on powder-based electron beam additive manufacturing technology. *Manufacturing Review* **2014**, *1* (2), 1-11. DOI: <https://doi.org/10.1115/ISFA2012-7256>
- [10] Gibson LJ MF A. *Cellular Solids: Structure and Properties*; 1999.
- [11] Harrysson O. L. A., Cansizoglu O., Marcellin-Little D. J., et al. Direct metal fabrication of titanium implants with tailored materials and mechanical properties using electron beam melting technology. *Materials Science and Engineering: C* **2008**, *28* (3), 366-373. DOI: <https://doi.org/10.1016/j.msec.2007.04.022>
- [12] Takezawa A., Koizumi Y. Kobashi M. High-stiffness and strength porous maraging steel via topology optimization and selective laser melting. *Additive Manufacturing* **2017**, *18*, 194-202. DOI: <https://doi.org/10.1016/j.addma.2017.10.004>
- [13] Lan X. Wang Z. Efficient high-temperature electromagnetic wave absorption enabled by structuring binary porous SiC with multiple interfaces. *Carbon* **2020**, *170*, 517-526. DOI: <https://doi.org/10.1016/j.carbon.2020.08.052>
- [14] Li Z., Wang K. F., Wang B. L., et al. The thermal shock resistance prediction of porous ceramic sandwich structures with temperature-dependent material properties. *Ceramics International* **2019**, *45* (3), 4043-4052. DOI: [10.1016/j.ceramint.2018.11.083](https://doi.org/10.1016/j.ceramint.2018.11.083)
- [15] Speirs M., Van Hooreweder B., Van Humbeeck J., et al. Fatigue behaviour of NiTi shape memory alloy scaffolds produced by SLM, a unit cell design comparison. *J Mech Behav Biomed Mater* **2017**, *70*, 53-59. DOI: <https://doi.org/10.1016/j.jmbbm.2017.01.016>
- [16] Yan C., Hao L., Hussein A., et al. Evaluations of cellular lattice structures manufactured using selective laser melting. *International Journal of Machine Tools and Manufacture* **2012**, *62*, 32-38. DOI: <https://doi.org/10.1016/j.ijmachtools.2012.06.002>
- [17] Keaveny TM WC H. Mechanical properties of cortical and trabecular bone. *In: Bone* **1993**, *7*, 285-344.
- [18] Philippe K. Zysset, X. Edward Guo, C. Edward Hofer, et al. Elastic modulus and hardness of cortical and trabecular bone lamellae measured by nanoindentation in the human femur. *Journal of Biomechanics* **1999**, *32* (10), 1005-1012. DOI: [https://doi.org/10.1016/S0021-9290\(99\)00111-6](https://doi.org/10.1016/S0021-9290(99)00111-6)

-
- [19] Monteiro E. d. S., Moura de Souza Soares F., Nunes L. F., et al. Comparison of the wettability and corrosion resistance of two biomedical Ti alloys free of toxic elements with those of the commercial ASTM F136 (Ti–6Al–4V) alloy. *Journal of Materials Research and Technology* **2020**, 9 (6), 16329-16338. DOI: <https://doi.org/10.1016/j.jmrt.2020.11.068>
- [20] Hedayati R., Sadighi M., Mohammadi-Aghdam M., et al. Effect of mass multiple counting on the elastic properties of open-cell regular porous biomaterials. *Materials & Design* **2016**, 89, 9-20. DOI: <https://doi.org/10.1016/j.matdes.2015.09.052>
- [21] Murr L. E., Gaytan S. M., Ramirez D. A., et al. Metal Fabrication by Additive Manufacturing Using Laser and Electron Beam Melting Technologies. *Journal of Materials Science & Technology* **2012**, 28 (1), 1-14. DOI: [https://doi.org/10.1016/s1005-0302\(12\)60016-4](https://doi.org/10.1016/s1005-0302(12)60016-4)
- [22] Bandyopadhyay A., Espana F., Balla V. K., et al. Influence of porosity on mechanical properties and in vivo response of Ti6Al4V implants. *Acta Biomater* **2010**, 6 (4), 1640-1648. DOI: <https://doi.org/10.1016/j.actbio.2009.11.011>
- [23] Murr L. E., Esquivel E. V., Quinones S. A., et al. Microstructures and mechanical properties of electron beam-rapid manufactured Ti–6Al–4V biomedical prototypes compared to wrought Ti–6Al–4V. *Materials Characterization* **2009**, 60 (2), 96-105. DOI: <https://doi.org/10.1016/j.matchar.2008.07.006>
- [24] Yan X., Li Q., Yin S., et al. Mechanical and in vitro study of an isotropic Ti6Al4V lattice structure fabricated using selective laser melting. *Journal of Alloys and Compounds* **2019**, 782, 209-223. DOI: <https://doi.org/10.1016/j.jallcom.2018.12.220>
- [25] Beretta S. Romano S. A comparison of fatigue strength sensitivity to defects for materials manufactured by AM or traditional processes. *International Journal of Fatigue* **2017**, 94, 178-191. DOI: <https://doi.org/10.1016/j.ijfatigue.2016.06.020>
- [26] Romano S., Brückner-Foit A., Brandão A., et al. Fatigue properties of AlSi10Mg obtained by additive manufacturing: Defect-based modelling and prediction of fatigue strength. *Engineering Fracture Mechanics* **2018**, 187, 165-189. DOI: <https://doi.org/10.1016/j.engfracmech.2017.11.002>
- [27] Wu X., Liang J., Mei J., et al. Microstructures of laser-deposited Ti–6Al–4V. *Materials & Design* **2004**, 25 (2), 137-144. DOI: <https://doi.org/10.1016/j.matdes.2003.09.009>
- [28] Zhang Y., Fang X., Wang H., et al. Microstructure and low-cycle fatigue performance of selective electron beam melted Ti6Al4V alloy. *International Journal of Fatigue* **2022**, 163, 107017. DOI: <https://doi.org/10.1016/j.ijfatigue.2022.107017>
- [29] Zhang Y., Zhang H., Xue J., et al. Microstructure transformed by heat treatment to improve fatigue property of laser solid formed Ti6Al4V titanium alloy. *Materials Science and Engineering: A* **2023**, 865, 144363. DOI: <https://doi.org/10.1016/j.msea.2022.144363>
- [30] Agius D., Kourousis K. I., Wallbrink C., et al. Cyclic plasticity and microstructure of as-built SLM Ti-6Al-4V: The effect of build orientation. *Materials Science and Engineering: A* **2017**, 701, 85-100. DOI: <https://doi.org/10.1016/j.msea.2017.06.069>
- [31] Kirka M. M., Greeley D. A., Hawkins C., et al. Effect of anisotropy and texture on the low cycle fatigue behavior of Inconel 718 processed via electron beam melting. *International Journal of Fatigue* **2017**, 105, 235-243. DOI: <https://doi.org/10.1016/j.ijfatigue.2017.08.021>
- [32] Bergmann G., Graichen F., Rohlmann A., et al. Realistic loads for testing hip implants. *Biomed Mater Eng* **2010**, 20 (2), 65-75. DOI: <https://doi.org/10.3233/BME-2010-0616>
- [33] Tofail S. A. M., Koumoulos E. P., Bandyopadhyay A., et al. Additive manufacturing: scientific and technological challenges, market uptake and opportunities. *Materials Today* **2018**, 21 (1), 22-37. DOI: <https://doi.org/10.1016/j.mattod.2017.07.001>
- [34] Laureijs RE, Roca JB, Narra SP, et al. Metal Additive Manufacturing: Cost Competitive Beyond Low Volumes. *Journal of Manufacturing Science and Engineering* **2017**, 139(8), 081010. DOI: <https://doi.org/10.1115/1.4035420>
- [35] Tan C., Weng F., Sui S., et al. Progress and perspectives in laser additive manufacturing of key aeroengine materials. *International Journal of Machine Tools and Manufacture* **2021**, 170, 103804. DOI: <https://doi.org/10.1016/j.ijmachtools.2021.103804>
- [36] Najmon J. C., Raesi S. Tovar A. Review of additive manufacturing technologies and applications in the aerospace industry. In *Additive Manufacturing for the Aerospace Industry*, 2019; pp 7-31.
- [37] Busachi A., Erkoyuncu J., Colegrove P., et al. A review of Additive Manufacturing technology and Cost Estimation techniques for the defence sector. *CIRP Journal of Manufacturing Science and Technology* **2017**, 19, 117-128. DOI:

<https://doi.org/10.1016/j.cirpj.2017.07.001>

[38] Cacace S., Furlan V., Sorci R., et al. Using recycled material to produce gas-atomized metal powders for additive manufacturing processes. *Journal of Cleaner Production* **2020**, 268, 122218. DOI: <https://doi.org/10.1016/j.jclepro.2020.122218>

[39] Tan C., Zou J., Li S., et al. Additive manufacturing of bio-inspired multi-scale hierarchically strengthened lattice structures. *International Journal of Machine Tools and Manufacture* **2021**, 167, 103764. DOI: <https://doi.org/10.1016/j.ijmachtools.2021.103764>

[40] Pham M. S., Liu C., Todd I., et al. Damage-tolerant architected materials inspired by crystal microstructure. *Nature* **2019**, 565 (7739), 305-311. DOI: <https://doi.org/10.1038/s41586-018-0850-3>

[41] Liu L., Ding Q., Zhong Y., et al. Dislocation network in additive manufactured steel breaks strength–ductility trade-off. *Materials Today* **2018**, 21 (4), 354-361. DOI: <https://doi.org/10.1016/j.mattod.2017.11.004>

[42] Kok Y., Tan X. P., Wang P., et al. Anisotropy and heterogeneity of microstructure and mechanical properties in metal additive manufacturing: A critical review. *Materials & Design* **2018**, 139, 565-586. DOI: <https://doi.org/10.1016/j.matdes.2017.11.021>

[43] Ford S., Mortara L., Minshall T. The Emergence of Additive Manufacturing: Introduction to the Special Issue. *Technological Forecasting and Social Change* **2016**, 102, 156-159. DOI: <https://doi.org/10.1016/j.techfore.2015.09.023>

[44] Yakout M., Elbestawi M. A., Veldhuis S. C. A Review of Metal Additive Manufacturing Technologies. *Solid State Phenomena* **2018**, 278, 1-14. DOI: <https://doi.org/10.4028/www.scientific.net/SSP.278.1>

[45] ASTM International. Standard Terminology for Additive Manufacturing Technologies. In *Rapid Manufacturing Association*, 2013; pp 10–12. DOI: <https://doi.org/10.1520/f2792-12a>.

[46] Tan C., Wang D., Ma W., et al. Ultra-strong bond interface in additively manufactured iron-based multi-materials. *Materials Science and Engineering: A* **2021**, 802, 140642. DOI: <https://doi.org/10.1016/j.msea.2020.140642>

[47] DebRoy T., Wei H. L., Zuback J. S., et al. Additive manufacturing of metallic components – Process, structure and properties. *Progress in Materials Science* **2018**, 92, 112-224. DOI: <https://doi.org/10.1016/j.pmatsci.2017.10.001>

[48] Yadroitsev I., Yadroitsava I., Bertrand P., et al. Factor analysis of selective laser melting process parameters and geometrical characteristics of synthesized single tracks. *Rapid Prototyping Journal* **2012**, 18 (3), 201-208. DOI: <https://doi.org/10.1108/13552541211218117>

[49] Sun J., Yang Y., Wang D. Parametric optimization of selective laser melting for forming Ti6Al4V samples by Taguchi method. *Optics & Laser Technology* **2013**, 49, 118-124. DOI: <https://doi.org/10.1016/j.optlastec.2012.12.002>

[50] Liu F., Gan D., Zhang K., et al. A selective strategy for determining suitable structure and fatigue behavior study of minimal surface scaffolds fabricated by EBM. *International Journal of Fatigue* **2023**, 167, 107380. DOI: <https://doi.org/10.1016/j.ijfatigue.2022.107380>

[51] Yadroitsev I., Smurov I. Surface Morphology in Selective Laser Melting of Metal Powders. *Physics Procedia* **2011**, 12, 264-270. DOI: <https://doi.org/10.1016/j.phpro.2011.03.034>

[52] Tan C., Li R., Su J., et al. Review on field assisted metal additive manufacturing. *International Journal of Machine Tools and Manufacture* **2023**, 189, 104032. DOI: <https://doi.org/10.1016/j.ijmachtools.2023.104032>

[53] Calignano F., Mercurio V., Rizza G., et al. Investigation of surface shot blasting of AlSi10Mg and Ti6Al4V components produced by powder bed fusion technologies. *Precision Engineering* **2022**, 78, 79-89. DOI: <https://doi.org/10.1016/j.precisioneng.2022.07.008>

[54] Navarro M., Michiardi A., Castano O., et al. Biomaterials in orthopaedics. *J R Soc Interface* **2008**, 5 (27), 1137-1158. DOI: <https://doi.org/10.1098/rsif.2008.0151>

[55] Marc Long Rack H. J. Review Titanium alloys in total joint replacement—a materials science perspective. *Biomaterials* **1998**, 19 (18), 1621—1639. DOI: [https://doi.org/10.1016/S0142-9612\(97\)00146-4](https://doi.org/10.1016/S0142-9612(97)00146-4)

[56] Zhang L. C., Chen L. Y. A Review on Biomedical Titanium Alloys: Recent Progress and Prospect. *Advanced Engineering Materials* **2019**, 21 (4), 1801215. DOI: <https://doi.org/10.1002/adem.201801215>

[57] Sezer N., Evis Z., Kayhan S. M., et al. Review of magnesium-based biomaterials and their applications. *Journal of Magnesium and Alloys* **2018**, 6 (1), 23-43. DOI:

<https://doi.org/10.1016/j.jma.2018.02.003>

- [58] Kaur M. Singh K. Review on titanium and titanium based alloys as biomaterials for orthopaedic applications. *Mater Sci Eng C Mater Biol Appl* **2019**, *102*, 844-862. DOI: <https://doi.org/10.1016/j.msec.2019.04.064>
- [59] Mughal M. P., Farooq M. U., Mumtaz J., et al. Surface modification for osseointegration of Ti6Al4V ELI using powder mixed sinking EDM. *J Mech Behav Biomed Mater* **2021**, *113*, 104145. DOI: <https://doi.org/10.1016/j.jmbbm.2020.104145>
- [60] Nan-Jue Cao Y.-H. Z., Fei Gao , Chen Liang , Zhen-Bo Wang , Yue Zhang , Chun-Ping Hao , Wei Wang Gradient nanostructured titanium stimulates cell responses in vitro and enhances osseointegration in vivo. *Annals of Translational Medicine* **2021**, *9* (07), 531. DOI: <https://doi.org/10.21037/atm-20-7588>
- [61] Nagels J S. M., Rozing PM. Stress shielding and bone resorption in shoulder arthroplasty. *Shoulder Elbow Surg* **2003**, *12* (01), 35-39. DOI: <https://doi.org/10.1067/mse.2003.22>
- [62] Oshida Y., Tuna E. B., Aktoren O., et al. Dental implant systems. *Int J Mol Sci* **2010**, *11* (4), 1580-1678. DOI: <https://doi.org/10.3390/ijms11041580>
- [63] WA L. Some Remarks on the Treatment of Fractures. *Br Med J* **1895**, *1*, 861. DOI: <https://doi.org/10.1136/bmj.1.1790.861>
- [64] W S. Vanadium steel bone plates and screws. *Surg Gynecol Obstet* **1912**, *14*, 629-634.
- [65] Bommala V. K., Krishna M. G. Rao C. T. Magnesium matrix composites for biomedical applications: A review. *Journal of Magnesium and Alloys* **2019**, *7* (1), 72-79. DOI: <https://doi.org/10.1016/j.jma.2018.11.001>
- [66] Yu W., Sun R., Guo Z., et al. Novel fluoridated hydroxyapatite/MAO composite coating on AZ31B magnesium alloy for biomedical application. *Applied Surface Science* **2019**, *464*, 708-715. DOI: <https://doi.org/10.1016/j.apsusc.2018.09.148>
- [67] Moghadasi K., Mohd Isa M. S., Ariffin M. A., et al. A review on biomedical implant materials and the effect of friction stir based techniques on their mechanical and tribological properties. *Journal of Materials Research and Technology* **2022**, *17*, 1054-1121. DOI: <https://doi.org/10.1016/j.jmrt.2022.01.050>
- [68] I.P. van Rossen D.D.S., L.H. Braak Ph.D., C. de Putter D.D.S., et al. Stress-absorbing elements in dental implants. *J Prosthet Dent* **1990**, *64* (2), 198-205. DOI: [https://doi.org/10.1016/0022-3913\(90\)90179-G](https://doi.org/10.1016/0022-3913(90)90179-G)
- [69] Marsumi Y. Pramono A. W. Influence of Niobium or Molybdenum in Titanium Alloy for Permanent Implant Application. *Advanced Materials Research* **2014**, *900*, 53-63. DOI: <https://doi.org/10.4028/www.scientific.net/AMR.900.53>
- [70] Zhao S., Hou W. T., Xu Q. S., et al. Ti-6Al-4V lattice structures fabricated by electron beam melting for biomedical applications. In *Titanium in Medical and Dental Applications*, 2018; pp 277-301.
- [71] Kapfer S. C., Hyde S. T., Mecke K., et al. Minimal surface scaffold designs for tissue engineering. *Biomaterials* **2011**, *32* (29), 6875-6882. DOI: <https://doi.org/10.1016/j.biomaterials.2011.06.012>
- [72] Billiet T., Gevaert E., De Schryver T., et al. The 3D printing of gelatin methacrylamide cell-laden tissue-engineered constructs with high cell viability. *Biomaterials* **2014**, *35* (1), 49-62. DOI: <https://doi.org/10.1016/j.biomaterials.2013.09.078>
- [73] Chang P. B., Williams B. J., Bhalla K. S., et al. Design and analysis of robust total joint replacements: finite element model experiments with environmental variables. *J Biomech Eng* **2001**, *123* (3), 239-246. DOI: <https://doi.org/10.1115/1.1372701>
- [74] D.R. Sumner, T.M. Turner, R. Igloria, et al. Functional adaptation and ingrowth of bone vary as a function of hip implant stiffness. *Journal of Biomechanics* **1998**, *31* (10), 909-917. DOI: [https://doi.org/10.1016/S0021-9290\(98\)00096-7](https://doi.org/10.1016/S0021-9290(98)00096-7)
- [75] Takemoto M., Fujibayashi S., Neo M., et al. Mechanical properties and osteoconductivity of porous bioactive titanium. *Biomaterials* **2005**, *26* (30), 6014-6023. DOI: <https://doi.org/10.1016/j.biomaterials.2005.03.019>
- [76] Babić M., Verić O., Božić Ž., et al. Fracture analysis of a total hip prosthesis based on reverse engineering. *Engineering Fracture Mechanics* **2019**, *215*, 261-271. DOI: <https://doi.org/10.1016/j.engfracmech.2019.05.003>
- [77] Elias C. N., Fernandes D. J., Souza F. M. d., et al. Mechanical and clinical properties of titanium and titanium-based alloys (Ti G2, Ti G4 cold worked nanostructured and Ti G5) for biomedical applications. *Journal of Materials Research and Technology* **2019**, *8* (1), 1060-1069.

- DOI: <https://doi.org/10.1016/j.jmrt.2018.07.016>
- [78] DF W. Titanium in medicine. *Springer* **2001**, 13-24.
- [79] Zadpoor A. A. Open forward and inverse problems in theoretical modeling of bone tissue adaptation. *J Mech Behav Biomed Mater* **2013**, 27, 249-261. DOI: <https://doi.org/10.1016/j.jmbbm.2013.05.017>
- [80] Yang L., Wu S., Yan C., et al. Fatigue properties of Ti-6Al-4V Gyroid graded lattice structures fabricated by laser powder bed fusion with lateral loading. *Additive Manufacturing* **2021**, 46, 102214. DOI: <https://doi.org/10.1016/j.addma.2021.102214>
- [81] Chen W., Yang J., Kong H., et al. Fatigue behaviour and biocompatibility of additively manufactured bioactive tantalum graded lattice structures for load-bearing orthopaedic applications. *Mater Sci Eng C Mater Biol Appl* **2021**, 130, 112461. DOI: <https://doi.org/10.1016/j.msec.2021.112461>
- [82] Wang N., Meenashisundaram G. K., Chang S., et al. A comparative investigation on the mechanical properties and cytotoxicity of Cubic, Octet, and TPMS gyroid structures fabricated by selective laser melting of stainless steel 316L. *J Mech Behav Biomed Mater* **2022**, 129, 105151. DOI: <https://doi.org/10.1016/j.jmbbm.2022.105151>
- [83] Herrera P., Hernandez-Nava E., Thornton R., et al. Abrasive wear resistance of Ti-6Al-4V obtained by the conventional manufacturing process and by electron beam melting (EBM). *Wear* **2023**, 524-525, 204879. DOI: <https://doi.org/10.1016/j.wear.2023.204879>
- [84] Zhu C., Lv Y., Qian C., et al. Microstructures, mechanical, and biological properties of a novel Ti-6V-4V/zinc surface nanocomposite prepared by friction stir processing. *Int J Nanomedicine* **2018**, 13, 1881-1898. DOI: <https://doi.org/10.2147/IJN.S154260>
- [85] Al-Bermani S. S., Blackmore M. L., Zhang W., et al. The Origin of Microstructural Diversity, Texture, and Mechanical Properties in Electron Beam Melted Ti-6Al-4V. *Metallurgical and Materials Transactions A* **2010**, 41 (13), 3422-3434. DOI: <https://doi.org/10.1007/s11661-010-0397-x>
- [86] Sun Z., Xiong K., Jin C., et al. An experimental and computational design low-modulus (HfNbTa)_{1-x}Ti_x multiprinciple elemental alloys with super formability for biomedical applications. *Materials Science and Engineering: A* **2023**, 876, 145137. DOI: <https://doi.org/10.1016/j.msea.2023.145137>
- [87] Liu Y. J., Wang H. L., Li S. J., et al. Compressive and fatigue behavior of beta-type titanium porous structures fabricated by electron beam melting. *Acta Materialia* **2017**, 126, 58-66. DOI: <https://doi.org/10.1016/j.actamat.2016.12.052>
- [88] Sallica-Leva E., Jardini A. L., Fogagnolo J. B. Microstructure and mechanical behavior of porous Ti-6Al-4V parts obtained by selective laser melting. *J Mech Behav Biomed Mater* **2013**, 26, 98-108. DOI: <https://doi.org/10.1016/j.jmbbm.2013.05.011>
- [89] Jin Y., Zou S., Pan B., et al. Biomechanical properties of cylindrical and twisted triply periodic minimal surface scaffolds fabricated by laser powder bed fusion. *Additive Manufacturing* **2022**, 56, 102899. DOI: <https://doi.org/10.1016/j.addma.2022.102899>
- [90] Zhang J., Liu Y., Babamiri B. B., et al. Enhancing specific energy absorption of additively manufactured titanium lattice structures through simultaneous manipulation of architecture and constituent material. *Additive Manufacturing* **2022**, 55, 102887. DOI: <https://doi.org/10.1016/j.addma.2022.102887>
- [91] Attarzadeh R. A.-N. S. H., Duwig C. Multi-objective optimization of TPMS-based heat exchangers for lowtemperature waste heat recovery. *Appl Therm Eng* **2022**, 212, 118448.
- [92] Zadpoor A. A. Mechanical performance of additively manufactured meta-biomaterials. *Acta Biomater* **2019**, 85, 41-59. DOI: <https://doi.org/10.1016/j.actbio.2018.12.038>
- [93] Van Hooreweder B., Kruth J.-P. Advanced fatigue analysis of metal lattice structures produced by Selective Laser Melting. *CIRP Annals* **2017**, 66 (1), 221-224. DOI: <https://doi.org/10.1016/j.cirp.2017.04.130>
- [94] Peng K., Cai G., Hu B., et al. Investigation on effect of pillar size on the comprehensive properties of Ti6Al4V lattice fabricated by selective laser melting. *Materials Science and Engineering: A* **2022**, 860, 144281. DOI: <https://doi.org/10.1016/j.msea.2022.144281>
- [95] Wang W., Yang X., Han B., et al. Analytical design of effective thermal conductivity for fluid-saturated prismatic cellular metal honeycombs. *Theoretical and Applied Mechanics Letters* **2016**, 6 (2), 69-75. DOI: <https://doi.org/10.1016/j.taml.2016.01.003>
- [96] Vasiliev V. V., Razin A. F. Anisogrid composite lattice structures for spacecraft and aircraft

-
- applications. *Composite Structures* **2006**, 76 (1-2), 182-189. DOI: <https://doi.org/10.1016/j.compstruct.2006.06.025>
- [97] He J., Ren M., Sun S., et al. Failure prediction on advanced grid stiffened composite cylinder under axial compression. *Composite Structures* **2011**, 93 (7), 1939-1946. DOI: <https://doi.org/10.1016/j.compstruct.2011.02.003>
- [98] Zok F. W., Waltner S. A., Wei Z., et al. A protocol for characterizing the structural performance of metallic sandwich panels: application to pyramidal truss cores. *International Journal of Solids and Structures* **2004**, 41 (22-23), 6249-6271. DOI: <https://doi.org/10.1016/j.ijsolstr.2004.05.045>
- [99] Kooistra G. W., Queheillalt D. T., Wadley H. N. G. Shear behavior of aluminum lattice truss sandwich panel structures. *Materials Science and Engineering: A* **2008**, 472 (1-2), 242-250. DOI: <https://doi.org/10.1016/j.msea.2007.03.034>
- [100] Chen H., Zheng Q., Zhao L., et al. Mechanical property of lattice truss material in sandwich panel including strut flexural deformation. *Composite Structures* **2012**, 94 (12), 3448-3456. DOI: <https://doi.org/10.1016/j.compstruct.2012.06.004>
- [101] Gu H., Pavier M., Shterenlikht A. Experimental study of modulus, strength and toughness of 2D triangular lattices. *International Journal of Solids and Structures* **2018**, 152-153, 207-216. DOI: <https://doi.org/10.1016/j.ijsolstr.2018.06.028>
- [102] Luo J. P., Huang Y. J., Xu J. Y., et al. Additively manufactured biomedical Ti-Nb-Ta-Zr lattices with tunable Young's modulus: Mechanical property, biocompatibility, and proteomics analysis. *Mater Sci Eng C Mater Biol Appl* **2020**, 114, 110903. DOI: <https://doi.org/10.1016/j.msec.2020.110903>
- [103] Almesmari A., Sheikh-Ahmad J., Jarrar F., et al. Optimizing the specific mechanical properties of lattice structures fabricated by material extrusion additive manufacturing. *Journal of Materials Research and Technology* **2023**, 22, 1821-1838. DOI: <https://doi.org/10.1016/j.jmrt.2022.12.024>
- [104] Babae S., Jahromi B. H., Ajdari A., et al. Mechanical properties of open-cell rhombic dodecahedron cellular structures. *Acta Materialia* **2012**, 60 (6-7), 2873-2885. DOI: <https://doi.org/10.1016/j.actamat.2012.01.052>
- [105] Yang Y., Shan M., Zhao L., et al. Multiple strut-deformation patterns based analytical elastic modulus of sandwich BCC lattices. *Materials & Design* **2019**, 181, 107916. DOI: <https://doi.org/10.1016/j.matdes.2019.107916>
- [106] Khaleghi S., Dehnavi F. N., Baghani M., et al. On the directional elastic modulus of the TPMS structures and a novel hybridization method to control anisotropy. *Materials & Design* **2021**, 210, 110074. DOI: <https://doi.org/10.1016/j.matdes.2021.110074>
- [107] Li S. J., Xu Q. S., Wang Z., et al. Influence of cell shape on mechanical properties of Ti-6Al-4V meshes fabricated by electron beam melting method. *Acta Biomater* **2014**, 10 (10), 4537-4547. DOI: <https://doi.org/10.1016/j.actbio.2014.06.010>
- [108] Long Bai , Cheng Gong , Xiaohong Chen , et al. Quasi-Static compressive responses and fatigue behaviour of Ti-6Al-4 V graded lattice structures fabricated by laser powder bed fusion. *Materials & Design* **2021**, 210 (15), 110110. DOI: <https://doi.org/10.1016/j.matdes.2021.110110>
- [109] Krishnan K., Lee D.-W., Al Teneji M., et al. Effective stiffness, strength, buckling and anisotropy of foams based on nine unique triple periodic minimal surfaces. *International Journal of Solids and Structures* **2022**, 238, 111418. DOI: <https://doi.org/10.1016/j.ijsolstr.2021.111418>
- [110] Ma Q., Zhang L., Ding J., et al. Elastically-isotropic open-cell minimal surface shell lattices with superior stiffness via variable thickness design. *Additive Manufacturing* **2021**, 47, 102293. DOI: <https://doi.org/10.1016/j.addma.2021.102293>
- [111] Yang N., Qian Z., Wei H., et al. Anisotropy and deformation of triply periodic minimal surface based lattices with skew transformation. *Materials & Design* **2023**, 225, 111595. DOI: <https://doi.org/10.1016/j.matdes.2023.111595>
- [112] Prajwal P., Ghuku S., Mukhopadhyay T. Large-deformation mechanics of anti-curvature lattice materials for mode-dependent enhancement of non-linear shear modulus. *Mechanics of Materials* **2022**, 171, 104337. DOI: <https://doi.org/10.1016/j.mechmat.2022.104337>
- [113] Liu F., Mao Z., Zhang P., et al. Functionally graded porous scaffolds in multiple patterns: New design method, physical and mechanical properties. *Materials & Design* **2018**, 160, 849-860. DOI: <https://doi.org/10.1016/j.matdes.2018.09.053>

- [114] Raghavendra S M. A., Fontanari V, et al. Evaluation of Static and Fatigue Properties of Regular Lattice and Trabecular Cellular Structures. *Procedia Structural Integrity* **2020**, 517–524. DOI: <https://doi.org/10.1016/j.prostr.2020.10.061>
- [115] Burr A., Persenot T., Dautre P.-T., et al. A numerical framework to predict the fatigue life of lattice structures built by additive manufacturing. *International Journal of Fatigue* **2020**, 139, 105769. DOI: <https://doi.org/10.1016/j.ijfatigue.2020.105769>
- [116] Stachurski Z. H. *Mechanical behavior of materials*; 2009.
- [117] Chen C., Ye D., Zhang L., et al. Effects of tensile/compressive overloads on fatigue crack growth behavior of an extra-low-interstitial titanium alloy. *International Journal of Mechanical Sciences* **2016**, 118, 55-66. DOI: <https://doi.org/10.1016/j.ijmecsci.2016.09.014>
- [118] Boniotti L., Beretta S., Patriarca L., et al. Experimental and numerical investigation on compressive fatigue strength of lattice structures of AlSi7Mg manufactured by SLM. *International Journal of Fatigue* **2019**, 128, 105181. DOI: <https://doi.org/10.1016/j.ijfatigue.2019.06.041>
- [119] Sterling A. J., Torries B., Shamsaei N., et al. Fatigue behavior and failure mechanisms of direct laser deposited Ti–6Al–4V. *Materials Science and Engineering: A* **2016**, 655, 100-112. DOI: <https://doi.org/10.1016/j.msea.2015.12.026>
- [120] Benedetti M., du Plessis A., Ritchie R. O., et al. Architected cellular materials: A review on their mechanical properties towards fatigue-tolerant design and fabrication. *Materials Science and Engineering: R: Reports* **2021**, 144, 100606. DOI: <https://doi.org/10.1016/j.mser.2021.100606>
- [121] Peng C., Tran P., Nguyen-Xuan H., et al. Mechanical performance and fatigue life prediction of lattice structures: Parametric computational approach. *Composite Structures* **2020**, 235, 111821. DOI: <https://doi.org/10.1016/j.compstruct.2019.111821>
- [122] Cutolo A. Van Hooreweder B. Fatigue behaviour of diamond based Ti-6Al-4V lattice structures produced by laser powder bed fusion: On the effect of load direction. *Materials Today Communications* **2022**, 33, 104661. DOI: <https://doi.org/10.1016/j.matcomm.2022.104661>
- [123] Dallago M W. B., Zanini F, et al. On the effect of geometrical imperfections and defects on the fatigue strength of cellular lattice structures additively manufactured via Selective Laser Melting. *International Journal of Fatigue* **2019**, 124, 348-360.
- [124] Pérez-Sánchez A., Yáñez A., Cuadrado A., et al. Fatigue behaviour and equivalent diameter of single Ti-6Al-4V struts fabricated by Electron Beam Melting orientated to porous lattice structures. *Materials & Design* **2018**, 155, 106-115. DOI: <https://doi.org/10.1016/j.matdes.2018.05.066>
- [125] Guo Y C. C., Tan L, et al. The role of pore structures on the fatigue properties of additively manufactured porous tantalum scaffolds produced by electron beam powder bed fusion. *Journal of Materials Research and Technology* **2022**, 19, 3461-3473. DOI: <https://doi.org/10.1016/j.jmrt.2022.06.096>
- [126] Yang L L. Y., Chen Y, et al. Topologically optimized lattice structures with superior fatigue performance. *International Journal of Fatigue* **2022**, 165, 107188. DOI: <https://doi.org/10.1016/j.ijfatigue.2022.107188>
- [127] Dallago M., Raghavendra S., Luchin V., et al. The role of node fillet, unit-cell size and strut orientation on the fatigue strength of Ti-6Al-4V lattice materials additively manufactured via laser powder bed fusion. *International Journal of Fatigue* **2021**, 142, 105946. DOI: <https://doi.org/10.1016/j.ijfatigue.2020.105946>
- [128] Ghouse S., Babu S., Nai K., et al. The influence of laser parameters, scanning strategies and material on the fatigue strength of a stochastic porous structure. *Additive Manufacturing* **2018**, 22, 290-301. DOI: <https://doi.org/10.1016/j.addma.2018.05.024>
- [129] Liang H., Yang Y., Xie D., et al. Trabecular-like Ti-6Al-4V scaffolds for orthopedic: fabrication by selective laser melting and in vitro biocompatibility. *Journal of Materials Science & Technology* **2019**, 35 (7), 1284-1297. DOI: <https://doi.org/10.1016/j.jmst.2019.01.012>
- [130] Yang L., Yan C., Cao W., et al. Compression–compression fatigue behaviour of gyroid-type triply periodic minimal surface porous structures fabricated by selective laser melting. *Acta Materialia* **2019**, 181, 49-66. DOI: <https://doi.org/10.1016/j.actamat.2019.09.042>
- [131] Serrano-Munoz I., Buffiere J. Y., Mokso R., et al. Location, location & size: defects close to surfaces dominate fatigue crack initiation. *Sci Rep* **2017**, 7, 45239. DOI:

<https://doi.org/10.1038/srep45239>

- [132] Yáñez A., Fiorucci M. P., Cuadrado A., et al. Surface roughness effects on the fatigue behaviour of gyroid cellular structures obtained by additive manufacturing. *International Journal of Fatigue* **2020**, *138*, 105702. DOI: <https://doi.org/10.1016/j.ijfatigue.2020.105702>
- [133] Romano S., Patriarca L., Foletti S., et al. LCF behaviour and a comprehensive life prediction model for AlSi10Mg obtained by SLM. *International Journal of Fatigue* **2018**, *117*, 47-62. DOI: <https://doi.org/10.1016/j.ijfatigue.2018.07.030>
- [134] Mian M. J., Razmi J., Ladani L. Defect analysis and fatigue strength prediction of as-built Ti6Al4V parts, produced using electron beam melting (EBM) AM technology. *Materialia* **2021**, *16*, 101041. DOI: <https://doi.org/10.1016/j.mtla.2021.101041>
- [135] Ataee A., Li Y., Fraser D., et al. Anisotropic Ti-6Al-4V gyroid scaffolds manufactured by electron beam melting (EBM) for bone implant applications. *Materials & Design* **2018**, *137*, 345-354. DOI: <https://doi.org/10.1016/j.matdes.2017.10.040>
- [136] Karami K., Blok A., Weber L., et al. Continuous and pulsed selective laser melting of Ti6Al4V lattice structures: Effect of post-processing on microstructural anisotropy and fatigue behaviour. *Additive Manufacturing* **2020**, *36*, 106800. DOI: <https://doi.org/10.1016/j.addma.2020.101433>
- [137] Goswami R., Qadri S. B., Feng C. R., et al. Residual stress and localized lattice rotation under fatigue loading. *Materials Science and Engineering: A* **2019**, *763*, 138113. DOI: <https://doi.org/10.1016/j.msea.2019.138113>
- [138] Sanaei N., Fatemi A. Defects in additive manufactured metals and their effect on fatigue performance: A state-of-the-art review. *Progress in Materials Science* **2021**, *117*, 100724. DOI: <https://doi.org/10.1016/j.pmatsci.2020.100724>
- [139] Molavitabrizi D., Ekberg A., Mousavi S. M. Computational model for low cycle fatigue analysis of lattice materials: Incorporating theory of critical distance with elastoplastic homogenization. *European Journal of Mechanics - A/Solids* **2022**, *92*, 104480. DOI: <https://doi.org/10.1016/j.euromechsol.2021.104480>
- [140] Li Z., Tian X.-j., Tang H.-b., et al. Low cycle fatigue behavior of laser melting deposited TC18 titanium alloy. *Transactions of Nonferrous Metals Society of China* **2013**, *23* (9), 2591-2597. DOI: [https://doi.org/10.1016/s1003-6326\(13\)62772-7](https://doi.org/10.1016/s1003-6326(13)62772-7)
- [141] Bentachfine S. P. G., Gilgert J., et al. Notch effect in low cycle fatigue. *International Journal of Fatigue* **1999**, *21* (05), 421-430. DOI: [https://doi.org/10.1016/S0142-1123\(99\)00004-3](https://doi.org/10.1016/S0142-1123(99)00004-3)
- [142] Ahmadi S. M., Hedayati R., Li Y., et al. Fatigue performance of additively manufactured meta-biomaterials: The effects of topology and material type. *Acta Biomater* **2018**, *65*, 292-304. DOI: <https://doi.org/10.1016/j.actbio.2017.11.014>
- [143] Bowman SM G. X., Cheng DW, et al. Creep Contributes to the Fatigue Behavior of Bovine Trabecular Bone. *Journal of Biomechanical Engineering* **1998**, *120* (05), 647-654. DOI: <https://doi.org/10.1115/1.2834757>
- [144] Li Y., Jahr H., Zhang X. Y., et al. Biodegradation-affected fatigue behavior of additively manufactured porous magnesium. *Additive Manufacturing* **2019**, *28*, 299-311. DOI: <https://doi.org/10.1016/j.addma.2019.05.013>
- [145] Wu M.-W., Chen J.-K., Lin B.-H., et al. Compressive fatigue properties of additive-manufactured Ti-6Al-4V cellular material with different porosities. *Materials Science and Engineering: A* **2020**, *790*, 139695. DOI: <https://doi.org/10.1016/j.msea.2020.139695>
- [146] Li S. J., Murr L. E., Cheng X. Y., et al. Compression fatigue behavior of Ti-6Al-4V mesh arrays fabricated by electron beam melting. *Acta Materialia* **2012**, *60* (3), 793-802. DOI: <https://doi.org/10.1016/j.actamat.2011.10.051>
- [147] Hedayati R., Hosseini-Toudeshky H., Sadighi M., et al. Computational prediction of the fatigue behavior of additively manufactured porous metallic biomaterials. *International Journal of Fatigue* **2016**, *84*, 67-79. DOI: <https://doi.org/10.1016/j.ijfatigue.2015.11.017>
- [148] Zhang P., Zhang D., Zhong B. Constitutive and damage modelling of selective laser melted Ti-6Al-4V lattice structure subjected to low cycle fatigue. *International Journal of Fatigue* **2022**, *159*, 106800. DOI: <https://doi.org/10.1016/j.ijfatigue.2022.106800>
- [149] Li Y., Zhan M., Jiang X., et al. Low-cycle fatigue behavior and life prediction of TA15 titanium alloy by crystal plasticity-based modelling. *Journal of Materials Research and Technology* **2023**, *23*, 954-966. DOI: <https://doi.org/10.1016/j.jmrt.2023.01.063>
- [150] Benedetti M., Fontanari V., Bandini M., et al. Low- and high-cycle fatigue resistance of

- Ti-6Al-4V ELI additively manufactured via selective laser melting: Mean stress and defect sensitivity. *International Journal of Fatigue* **2018**, *107*, 96-109. DOI: <https://doi.org/10.1016/j.ijfatigue.2017.10.021>
- [151] Fatemi A., Molaei R., Sharifimehr S., et al. Multiaxial fatigue behavior of wrought and additive manufactured Ti-6Al-4V including surface finish effect. *International Journal of Fatigue* **2017**, *100*, 347-366. DOI: <https://doi.org/10.1016/j.ijfatigue.2017.03.044>
- [152] Xiaochen, L., Shiyang, W. Zhidong C. Effect of Cryogenic Treatment Duration on Microstructure and Mechanical Properties of TC4 Dual-Phase Titanium Alloy. *Journal of Changzhou University* **2022**, *34* (04), 7-13. DOI: <https://doi.org/10.3969/j.isn>.
- [153] M.M. Megahed, A.R.S. Ponter Morrison C. J. Experimental investigations into the influence of cyclic phenomena of metals on structural ratchetting behaviour. *Int J Mech Sci* **1984**, *26*, 625-638. DOI: [https://doi.org/10.1016/0020-7403\(84\)90016-X](https://doi.org/10.1016/0020-7403(84)90016-X)
- [154] OH B. The exponential law of endurance tests. *Proc Am Soc Test Mater* **1910**, *10* (24), 625-630.
- [155] Niesłony A. Böhm M. Mean Stress Effect Correction in Frequency-domain Methods for Fatigue Life Assessment. *Procedia Engineering* **2015**, *101*, 347-354. DOI: <https://doi.org/10.1016/j.proeng.2015.02.042>
- [156] O.B. Olurin, K.Y.G. McCullough, N.A. Fleck, et al. Fatigue crack propagation in aluminium alloy foams *International Journal of Fatigue* **2001**, *23* (05), 375-382. DOI: [https://doi.org/10.1016/S0142-1123\(01\)00010-X](https://doi.org/10.1016/S0142-1123(01)00010-X)
- [157] FE-SAFE:FATIGUE THEORY REFERENCE MANUAL. (accessed).
- [158] Yu B., Li Y., Abbas B., et al. An analytical method to calculate effective elastic properties of mapped rhombic dodecahedron structures fabricated with electron beam melting. *Materials Today Communications* **2022**, *32*, 103993. DOI: <https://doi.org/10.1016/j.mtcomm.2022.103993>
- [159] Strano G., Hao L., Everson R. M., et al. Surface roughness analysis, modelling and prediction in selective laser melting. *Journal of Materials Processing Technology* **2013**, *213* (4), 589-597. DOI: <https://doi.org/10.1016/j.jmatprotec.2012.11.011>
- [160] Kotousov A., Bortolan Neto L. Rahman S. S. Theoretical model for roughness induced opening of cracks subjected to compression and shear loading. *International Journal of Fracture* **2011**, *172* (1), 9-18. DOI: <https://doi.org/10.1007/s10704-011-9642-6>
- [161] Xiao L., Li S., Song W., et al. Process-induced geometric defect sensitivity of Ti-6Al-4V lattice structures with different mesoscopic topologies fabricated by electron beam melting. *Materials Science and Engineering: A* **2020**, *778*, 139092. DOI: <https://doi.org/10.1016/j.msea.2020.139092>
- [162] Pyka G., Kerckhofs G., Papantoniou I., et al. Surface Roughness and Morphology Customization of Additive Manufactured Open Porous Ti6Al4V Structures. *Materials (Basel)* **2013**, *6* (10), 4737-4757. DOI: <https://doi.org/10.3390/ma6104737>
- [163] Li S., Yan P., Fan L., et al. Effect of cryogenic machining-strengthening process on enhanced surface integrity and fatigue properties of ZK61M magnesium alloy. *Journal of Manufacturing Processes* **2023**, *92*, 297-310. DOI: <https://doi.org/10.1016/j.jmapro.2023.02.065>
- [164] Wu B., Pan Z., Ding D., et al. Effects of heat accumulation on microstructure and mechanical properties of Ti6Al4V alloy deposited by wire arc additive manufacturing. *Additive Manufacturing* **2018**, *23*, 151-160. DOI: <https://doi.org/10.1016/j.addma.2018.08.004>
- [165] Rahman M. A., Rahman M. Kumar A. S. Modelling of flow stress by correlating the material grain size and chip thickness in ultra-precision machining. *International Journal of Machine Tools and Manufacture* **2017**, *123*, 57-75. DOI: <https://doi.org/10.1016/j.ijmachtools.2017.08.001>
- [166] Wu B., Qiu Z., Dong B., et al. Effects of synchronized magnetic arc oscillation on microstructure, texture, grain boundary and mechanical properties of wire arc additively manufactured Ti6Al4V alloy. *Additive Manufacturing* **2022**, *54*, 102723. DOI: <https://doi.org/10.1016/j.addma.2022.102723>
- [167] Banerjee D. Williams J. C. Perspectives on Titanium Science and Technology. *Acta Materialia* **2013**, *61* (3), 844-879. DOI: <https://doi.org/10.1016/j.actamat.2012.10.043>
- [168] Zaefferer S. A study of active deformation systems in titanium alloys: dependence on alloy composition and correlation with deformation texture. *Materials Science and Engineering* **2003**, *344* (1-3), 20-30. DOI: [https://doi.org/10.1016/S0921-5093\(02\)00421-5](https://doi.org/10.1016/S0921-5093(02)00421-5)

-
- [169] Xiao G. B., To S. Jelenković E. V. Effects of non-amorphizing hydrogen ion implantation on anisotropy in micro cutting of silicon. *Journal of Materials Processing Technology* **2015**, 225, 439-450. DOI: <https://doi.org/10.1016/j.jmatprotec.2015.06.017>
- [170] Agnew S. R. Duygulu Ö. Plastic anisotropy and the role of non-basal slip in magnesium alloy AZ31B. *International Journal of Plasticity* **2005**, 21 (6), 1161-1193. DOI: <https://doi.org/10.1016/j.ijplas.2004.05.018>
- [171] Anne B. R., Okuyama Y., Morikawa T., et al. Activated slip systems in bimodal Ti-6Al-4V plastically deformed at low and moderately high temperatures. *Materials Science and Engineering: A* **2020**, 798, 140211. DOI: <https://doi.org/10.1016/j.msea.2020.140211>
- [172] Bridier F., Villechaise P. Mendez J. Analysis of the different slip systems activated by tension in a α/β titanium alloy in relation with local crystallographic orientation. *Acta Materialia* **2005**, 53 (3), 555-567. DOI: <https://doi.org/10.1016/j.actamat.2004.09.040>
- [173] Zhao Z. To S. An investigation of resolved shear stress on activation of slip systems during ultraprecision rotary cutting of local anisotropic Ti-6Al-4V alloy: Models and experiments. *International Journal of Machine Tools and Manufacture* **2018**, 134, 69-78. DOI: <https://doi.org/10.1016/j.ijmachtools.2018.07.001>
- [174] Li H., Mason D. E., Bieler T. R., et al. Methodology for estimating the critical resolved shear stress ratios of α -phase Ti using EBSD-based trace analysis. *Acta Materialia* **2013**, 61 (20), 7555-7567. DOI: <https://doi.org/10.1016/j.actamat.2013.08.042>
- [175] H. Li, C.J. Boehlert, T.R. Bieler, et al. Examination of the distribution of the tensile deformation systems in tension and tension-creep of Ti-6Al-4V (wt.%) at 296K and 728K. *Philos Mag* **2015**, 95, 691-729. DOI: <https://doi.org/10.1080/14786435.2014.1001459>
- [176] Vidyarthi M. K., Ghose A. K. Chakrabarty I. Effect of deep cryogenic treatment on the microstructure and wear performance of Cr-Mn-Cu white cast iron grinding media. *Cryogenics* **2013**, 58, 85-92. DOI: <https://doi.org/10.1016/j.cryogenics.2013.10.005>
- [177] R Filip, K Kubiak Ziaja W. The effect of microstructure on the mechanical properties of two-phase titanium alloys. *Materials Processing Technology* **1997**, 18, 361-363. DOI: [https://doi.org/10.1016/S0924-0136\(02\)00248-0](https://doi.org/10.1016/S0924-0136(02)00248-0)
- [178] Li G. R., Li Y. M., Wang F. F., et al. Microstructure and performance of solid TC4 titanium alloy subjected to the high pulsed magnetic field treatment. *Journal of Alloys and Compounds* **2015**, 644, 750-756. DOI: <https://doi.org/10.1016/j.jallcom.2015.04.191>
- [179] Zhao F., Ding X., Cui R., et al. Research on microstructure and texture of as-extruded AZ31 magnesium alloy during thermal compression. *Journal of Materials Research* **2019**, 34 (12), 2114-2125. DOI: <https://doi.org/10.1557/jmr.2019.90>
- [180] Yang S J W N. S. Investigation of α_2/γ phase transformation mechanism under the interaction of dislocation with lamellar interface in primary creep of lamellar TiAl alloys. *MSEA* **2002**, 329, 898-905. DOI: [https://doi.org/10.1016/S0921-5093\(01\)01572-6](https://doi.org/10.1016/S0921-5093(01)01572-6)
- [181] Guo Y., Chen C., Tan L., et al. The role of pore structures on the fatigue properties of additively manufactured porous tantalum scaffolds produced by electron beam powder bed fusion. *Journal of Materials Research and Technology* **2022**, 19, 3461-3473. DOI: <https://doi.org/10.1016/j.jmrt.2022.06.096>
- [182] WA Glaeser Lawless B. Behavior of alloy Ti-6Al-4V under pre-fretting and subsequent fatigue conditions. *Wear* **2001**, 250, 621-630. DOI: [https://doi.org/10.1016/S0043-1648\(01\)00669-X](https://doi.org/10.1016/S0043-1648(01)00669-X)
- [183] Gong HJ R. K., Starr T, et al. Effect of Defects on Fatigue Tests of As-Build Ti-6Al-4V Parts Fabricated by Selective Laser Melting. *International Solid Freeform Fabrication Symposium* **2012**, 499-506. DOI: <http://dx.doi.org/10.26153/tsw/15369>
- [184] Yu B., Li Y., Abbes B., et al. Effective compressive elastic behavior of rhombic dodecahedron structure with and without border constraints. *Composite Structures* **2021**, 259, 113500. DOI: <https://doi.org/10.1016/j.compstruct.2020.113500>
- [185] Cheng X. Y., Li S. J., Murr L. E., et al. Compression deformation behavior of Ti-6Al-4V alloy with cellular structures fabricated by electron beam melting. *J Mech Behav Biomed Mater* **2012**, 16, 153-162. DOI: <https://doi.org/10.1016/j.jmbbm.2012.10.005>
- [186] Horn T. J., Harrysson O. L. A., Marcellin-Little D. J., et al. Flexural properties of Ti6Al4V rhombic dodecahedron open cellular structures fabricated with electron beam melting. *Additive Manufacturing* **2014**, 1-4, 2-11. DOI: <https://doi.org/10.1016/j.addma.2014.05.001>
- [187] Wang Q. S., Li S. J., Hou W. T., et al. Mechanistic understanding of compression-compression fatigue behavior of functionally graded Ti-6Al-4V mesh structure fabricated by

electron beam melting. *J Mech Behav Biomed Mater* **2020**, *103*, 103590. DOI: <https://doi.org/10.1016/j.jmbbm.2019.103590>



Publications

Yu BN, Li YM, Abbas B, et al. Effective compressive elastic behavior of rhombic dodecahedron structure with and without border constraints. *Composite Structures* 2021; 257: 113300. <https://doi.org/10.1016/j.compstruct.2020.113500>

(Q1, Impact factor: 6.3)

Yu BN, Li YM, Abbas B, et al. An analytical method to calculate effective elastic properties of mapped rhombic dodecahedron structures fabricated with electron beam melting. *MATER TODAY COMMUN* 2022; 32: 103993. <https://doi.org/10.1016/j.mtcomm.2022.103993>

(Q2, Impact factor: 3.8)

Yu BN, Li YM, Abbas B, et al. Experimental and numerical study of the compressive fatigue behavior of a Ti6Al4V mapped rhomboidal dodecahedral structure fabricated by electron beam melting. *IJF* 2023; 177: 107912. <https://doi.org/10.1016/j.ijfatigue.2023.107912>

(Q1, Impact factor: 6.0)

Acknowledgments

Minimizing preamble, offering heartfelt gratitude.

I express my gratitude to Dr. Yuming LI, my mentor. His significant contribution to this thesis has had a profound impact on my life. Throughout my entire doctoral journey, the COVID-19 pandemic, which spanned France and China, immersed me in three years of seclusion, causing profound emotional fluctuations. Yuming's academic guidance and psychological support will forever be etched in my memory.

I extend my gratitude to my collaborative mentors, Prof. Boussad ABBES and Prof. Baoyi YU, for providing me with research insights, academic guidance, experimental resources, and financial support. You have been the unwavering pillars that aided me in conquering my doctoral pursuits.

I am deeply thankful to my mother, Mrs. Guiqing SU, whose steadfast dedication and companionship over the course of several decades have been the driving force behind the completion of my doctoral thesis. This thesis stands as a gift to my mother.

To my cherished wife, Mrs. Shuhao YU, I appreciate your daily presence in a foreign land, which epitomizes our love. It is my greatest remorse that I couldn't be by your side consistently throughout our five years of affection.

I express gratitude to our adorable feline companion, Pumbaa YU, for standing in my stead beside my wife, for which more cans of cat food shall serve as recompense.

I am grateful to my fellow colleagues, Tahar, Shuning LYU, and Huiwen ZHU. During my doctoral studies, you provided invaluable support, and your influence is evident throughout this thesis.

Finally, I express gratitude to myself for persevering during the most arduous years. Amidst numerous instances of helplessness and heartache, poignant sentiments and separations, I hope these experiences will become our most cherished treasures upon closure.

Life is short; enjoy it in a timely fashion. Approach all matters with equanimity, and let everything follow the heart.

The conclusion of this thesis marks the end of the summer of 2023.

